



THE HONG KONG
POLYTECHNIC UNIVERSITY

香港理工大學

Pao Yue-kong Library

包玉剛圖書館

Copyright Undertaking

This thesis is protected by copyright, with all rights reserved.

By reading and using the thesis, the reader understands and agrees to the following terms:

1. The reader will abide by the rules and legal ordinances governing copyright regarding the use of the thesis.
2. The reader will use the thesis for the purpose of research or private study only and not for distribution or further reproduction or any other purpose.
3. The reader agrees to indemnify and hold the University harmless from and against any loss, damage, cost, liability or expenses arising from copyright infringement or unauthorized usage.

IMPORTANT

If you have reasons to believe that any materials in this thesis are deemed not suitable to be distributed in this form, or a copyright owner having difficulty with the material being included in our database, please contact lbsys@polyu.edu.hk providing details. The Library will look into your claim and consider taking remedial action upon receipt of the written requests.

The Hong Kong Polytechnic University
Department of Applied Physics

**Study of Organic-inorganic Hybrid Solar
Cells**

Lo Shing Chung

A thesis submitted in partial fulfilment of the requirements for
the degree of Master of Philosophy

JUNE 2012



Certificate of Originality

I hereby declare that this thesis is my own work and that, to the best of my knowledge and belief, it reproduces no material previously published or written nor material which has been accepted for the award of any other degree or diploma, except where due acknowledgement has been made in the text.

_____ (Signature)

Lo Shing Chung (Name of candidate)



Abstract

Conventional solar cells based on bulk silicon have been considered as a promising candidate to deal with the world energy crisis. However, the fabrication of such kind of solar cells needs high temperature, high vacuum and high purity materials. These conditions inevitably result in expensive manufacturing cost and limited production area. Therefore, it is desirable to develop novel photovoltaic devices with easy fabrication, low cost and availability for large area production to replace the commercial silicon-based solar cells. Following the invention of organic semiconductors and the fast development of thin film technology, organic solar cells have been considered to be the third-generation photovoltaic devices. Organic materials have several important advantages, including low cost, solution processability and flexibility, making organic solar cells a very attractive area to be investigated.

In this project, organic solar cells composed of poly(3-hexylthiophene) (P3HT) and titanium oxide (TiO_2) have been studied. P3HT is a p-type semiconducting polymer that has high light absorption coefficient in the visible region and is soluble in common organic solvents. Therefore P3HT can be used for producing thin film devices by simple printing or coating techniques and a few hundred nanometer thick P3HT film is enough to absorb sufficient light to generate electricity. TiO_2 is a n-type semiconductor which exhibits higher electron mobility than that of organic semiconductors. More importantly, TiO_2 can form a staggered heterojunction with P3HT and show



photovoltaic effect. In our experiments, a TiO₂ thin film has been coated on an indium tin oxide (ITO) electrode by spin-coating and subsequently annealed for crystallization. In order to enhance the performance of the solar cell, aligned TiO₂ nanofibers have been fabricated on the TiO₂ thin film by electrospinning to increase the interfacial area between TiO₂ and P3HT. Afterward, P3HT film of ~200nm thick has been spin-coated on the TiO₂ nanofibrous film and annealed in a nitrogen-filled glovebox. Gold electrode is then evaporated on top of the P3HT. Consequently, J-V curve of the device has been measured under a solar simulator with AM1.5 filter to characterize the photovoltaic parameters of such hybrid solar cell.

Considering the absorption range of TiO₂ and P3HT, the cell only utilizes a narrow part of the solar spectrum. Hence, we aim to improve the absorption by adding an inorganic semiconductor interlayer. Surface modification of cadmium sulphide (CdS) on electrospun TiO₂ nanofibers using electrochemical deposition has been employed to improve the performance of the solar cell. Because the band gap energy of CdS is between those of TiO₂ and P3HT, it provides a different absorption peak in the solar spectrum. The effect of such modification has been analysed by measuring the external quantum efficiency and J-V characteristics of the device. In addition, different microscopy techniques, such as field emission scanning electron microscopy and transmission electron microscopy, have been employed to investigate the morphology of nanofibers before and after the deposition.



In an ordinary organic solar cell, a reflective electrode is commonly adopted to ensure a sufficient absorption of light in the active layer. But it is also feasible to use a transparent electrode in the organic solar cell to collect light from both sides. Here, we use graphene as the top electrode of an organic solar cell since graphene is a fascinating material bearing flexible, metallic and transparent properties. After the transfer of graphene on the active layer, a hydrophilic thin layer of poly(3,4-ethylenedioxythiophene):poly(styrene-sulfonate) (PEDOT:PSS) is added to serve as the electron blocking layer. Moreover, due to the doping effect of PEDOT:PSS on graphene, the series resistance of the device is dramatically reduced. In the end, we obtain a semi-transparent device that can absorb light from both sides. The performance of the device under two single-sided and double-sided illuminations has been characterized.

In summary, our results indicate that the efficiency of a hybrid solar cell can be optimized by various strategies, including interfacial modification, control of the nanostructure of heterojunction and broadening the light absorption region of the active layer. In addition, the fabrication of semi-transparent solar cells which can collect light from both sides is also a meaningful way to enhance the energy harvesting of the devices in real applications.



List of Publications

Journal

S. Wu, J. Li, S. C. Lo, Q. Tai and F. Yan, “Enhanced performance of hybrid solar cells based on ordered electrospun ZnO nanofibers modified with CdS on the surface”, *Organic Electronics* 13 (2012) 1569-1575.

S. C. Lo, Z. Liu, J. Li, H. L. W. Chan and F. Yan, “Hybrid solar cells based on poly (3-hexylthiophene) and electrospun TiO₂ nanofibers modified by CdS nanoparticles”, submitted to *Journal of Applied Physics*.

S. C. Lo, Z. Liu, H. L. W. Chan and F. Yan, “Semitransparent hybrid solar cells with graphene electrodes”, unpublished.

S. C. Lo, H. L. W. Chan and F. Yan, “Organic and inorganic-nanomaterial hybrid solar cells – a review”, submitted to *Journal of Nanomaterials*.

Presentation in Conference

S. C. Lo, Z. Liu, H. L. W. Chan and F. Yan, “The application of electrospun TiO₂ nanofibers with effective surface modification in organic-inorganic hybrid solar cells”, International Conference on Materials for Advanced Technologies in Singapore (July 2011).



Acknowledgements

I would like to express my appreciation to my chief supervisor, Prof. Helen L. W. Chan, for giving me an opportunity to take up this challenge and inspiring study and also for her constant encouragement, valuable suggestion and guidance throughout the course of study.

I would like to thank my co-supervisor, Dr. F. Yan, for his patience and guidance. He trained me up to be an independent researcher with good problem solving and analytical skills.

I also wish to express my appreciation to my research group members especially Mr. Z. K. Liu for his informative experience in device fabrication and Dr. J. H. Li for his support of sophisticated TEM technique.

I gratefully acknowledge the encouragement, support and friendship of all my classmates and colleagues in the Department of Applied Physics of The Hong Kong Polytechnic University. Thanks are also extended to Mr. H. Y. Yu, Miss. S. M. Ng and Dr. S. H. Choy for their helpful assistance and discussion on practical experimental skill.

I would like to thank my family, friends and Mrs. Rachel C. T. Lo for their endless support, patience and understanding.



Table of Contents

Certificate of Originality	II
Abstract.....	III
List of Publications.....	VI
Acknowledgements.....	VII
Table of Contents.....	VIII
List of Figures and Tables	XII
Chapter 1 Introduction.....	16
1.1 Background.....	16
1.2 Motivation	18
1.3 Overview	20
Chapter 2 Principle of Photovoltaic Device.....	23
2.1 Organic conjugated polymers	23
2.2 Concept of organic photovoltaic cell.....	25
2.2.1 <i>Coupling of photon</i>	26
2.2.2 <i>Photon absorption</i>	27
2.2.3 <i>Exciton generation</i>	27
2.2.4 <i>Exciton diffusion</i>	29
2.2.5 <i>Exciton dissociation</i>	29



2.2.6 Charge transportation	30
2.2.7 Charge collection.....	30
2.3 Photovoltaic parameters	31
2.3.1 External quantum efficiency (EQE).....	31
2.3.2 Current density versus voltage (J-V) characteristics.....	32
2.4 Organic-inorganic hybrid junction and junction morphology	35
2.4.1 Nanoparticle junction	36
2.4.2 Nanorod junction	38
2.4.3 Ordered junction.....	39
2.4.4 Porous junction.....	41
2.5 Characterization method.....	43
2.5.1 J-V characteristic measurement.....	43
2.5.2 EQE measurement	44
2.5.3 Scanning electron microscopy (SEM).....	45
2.5.4 Transmission electron microscopy (TEM)	47
2.5.5 Ultraviolet – visible (UV-vis) spectroscopy.....	48
Chapter 3 TiO₂/P3HT Hybrid Junction Solar Cell.....	50
3.1 Introduction	50
3.2 Properties of TiO ₂	51
3.3 Properties of P3HT	54
3.4 Electrospinning process.....	57



3.4.1 Process principle	58
3.4.2 Equipment.....	60
3.5 Fabrication of photovoltaic device	61
3.6 Characterization of devices structure and performance.....	64
3.7 Discussion.....	71
Chapter 4 Interfacial Modification	74
4.1 Introduction	74
4.2 Properties of cadmium sulfide (CdS)	76
4.3 Electrochemical deposition.....	78
4.3.1 Theory of electrochemical deposition.....	78
4.3.2 Equipment.....	80
4.3.3 Deposition process of CdS.....	81
4.4 Characterization of modified surface and fibers.....	82
4.5 Characterization of modified devices	87
4.6 Discussion.....	94
Chapter 5 Graphene Electrode Replacement.....	96
5.1 Introduction	96
5.2 Properties of graphene.....	98
5.3 Properties of PEDOT:PSS	100



5.4 Transferring and doping process.....	101
5.5 Graphene characterization	102
5.6 Characterization of non-doping semi-transparent device	103
5.7 Characterization of doped semi-transparent device.....	105
5.7.1 <i>Single-sided illumination analysis</i>	106
5.7.2 <i>Effective thickness</i>	110
5.7.3 <i>Double-sided illumination analysis</i>	111
5.8 Discussion.....	115
Chapter 6 Conclusions and Future Work	116
6.1 Conclusions	116
6.2 Future work	117
References	119



List of Figures and Tables

Figure 1-1 Sun light irradiance and photon flux [4].	19
Figure 2-1 Molecular configuration of four common conjugated photovoltaic polymers.	24
Figure 2-2 Schematic diagram of electron transition.....	28
Figure 2-3 Typical J-V characteristics of a solar cell.....	33
Figure 2-4 Schematic diagram of (a) bilayered junction, (b) disorder bulk hetero- junction and (c) order structure of solid state solar cell.	36
Figure 2-5 Microscopic image of nanoparticles [32,33].....	37
Figure 2-6 Morphology of ordered structure for hybrid solar cells. (a) ZnO/TiO ₂ nanorod [36], the scale bar represents 200 nm. (b) TiO ₂ nanotube [37] and (c) cross-aligned TiO ₂ nanofibers [28].....	40
Figure 2-7 IPCE of porous TiO ₂ device. (a) TiO ₂ /organic dye/OMeTAD and (b) TiO ₂ /Sb ₂ S ₃ /P3HT [41,30].....	43
Figure 2-8 Schematic diagram of EQE measurement.....	45
Figure 2-9 Interaction volume of electron beam.....	46
Figure 3-1 Band diagram (a) and schematic diagram (b) of P3HT/TiO ₂ device.	50
Figure 3-2 Unit cell of (a) anatase [49] and (b) rutile [50].	52
Figure 3-3 Phase diagram of TiO ₂ [51].....	54
Figure 3-4 Absorption spectra of P3HT in solution (black) and in solid state (grey) [69].	55
Figure 3-5 Coupling structure of 3-position alkyl substituted thiophene ring and	



structure of polythiophene.....	57
Figure 3-6 Charged jet bending under instability [83].....	59
Figure 3-7 Schematic diagram of electrospinning set-up.	60
Figure 3-8 Flow chart of device fabrication.	63
Figure 3-9 Morphology and alignment of nanofibers before annealing.	65
Figure 3-10 SEM images of TiO ₂ nanofibers at (a) x4500 (b) x30000 magnification. ...	66
Figure 3-11 (a) Morphology (b) diffraction pattern of TiO ₂ nanofiber under TEM.	67
Figure 3-12 Contact angle of toluene on TiO ₂ film.	68
Figure 3-13 Current density – voltage curves for TiO ₂ /P3HT devices with different number of fiber layers.	69
Figure 4-1 (a) Three-dimensional structure and (b) band structure of modified device.	75
Figure 4-2 Structure of (a) greenockite [114] and (b) hawleyite [115].....	77
Figure 4-3 Schematic diagram of set-up of electrochemical deposition.....	80
Figure 4-4 CdS grown on flat TiO ₂ by a (a) 1 h, (b) 2 h and (c) 3 h deposition process.	82
Figure 4-5 Contact angle of toluene on CdS deposition.	83
Figure 4-6 SEM images of TiO ₂ nanofibers with CdS deposition.....	84
Figure 4-7 (a) Morphology, (b) atomic configuration and (c) diffraction pattern of a CdS-coated nanofiber.	85
Figure 4-8 Absorption spectra of constitutive materials.....	87
Figure 4-9 J-V characteristics of flat devices with different deposition time.	88
Figure 4-10 Comparison of EQE of flat device with and without CdS deposition.	90



Figure 4-11 J-V characteristics of the fibrous devices with different CdS deposition time.92

Figure 4-12 EQE of the fibrous devices with different deposition time94

Figure 5-1 Structure of graphene [144].99

Figure 5-2 Structure of PEDOT:PSS [149].....100

Figure 5-3 Contact angle of water on P3HT (a) before and (b) after O₂ plasma treatment.....101

Figure 5-4 Transmittance of graphene from 300 nm to 800 nm.103

Figure 5-5 J-V characteristics of normal device and non-doped device at different side of illumination.....105

Figure 5-6 J-V characteristics of the doped devices with illumination on the (a) ITO and (b) graphene side.107

Figure 5-7 EQE of the doped devices with illumination on (a) ITO and (b) graphene side.108

Figure 5-8 (a) Transmittance of four active layers and (b) least square fitting of the transmittance at $\lambda = 560$ nm with respect to d.111

Figure 5-9 Schematic diagram of the holder for double side illumination.112

Figure 5-10 J-V characteristics of semi-transparent devices with respect to illumination from ITO, graphene (Gra) and on both side (DS).113

Table 3-1 Material parameters of rutile and anatase [57,58].....53

Table 3-2 Summary of performance parameters of TiO₂/P3HT devices with different number of nanofiber layers.71



Table 4-1	Summary of performance parameters of the modified flat devices.	89
Table 4-2	Summary of performance parameters of the modified fibrous devices.	93
Table 5-1	Summary of performance parameters of the non-doped device and the normal device.	104
Table 5-2	Estimated value of the effective thickness of P3HT.	110
Table 5-3	Summary of performance parameters of the semi-transparent devices with respect to the different illumination cases.	114



Chapter 1 Introduction

1.1 Background

Energy plays a leading supportive role in the world-wide rapid developments. From mining, purification of raw material and synthesis, to agriculture, manufacturing, building, transportation and lighting, huge amount of energy is consumed in every process which is essential to maintain our urban live and cultural activities. There are surveys reported by the International Energy Agency (IEA) that the global energy consumption keeps increasing significantly in the past few decades and it is predicted that this trend will continue.

Among all the sources of energy, fossil fuel, especially coal, has been the most common source all along despite that other renewable energy sources have been investigated and developed. However, fossil fuel reserved under the ground is limited and is close to be exhausted within one to two centuries. Owing to this energy crisis, a novel renewable source of energy is in urgent need. This source is required to be clean, sustainable and capable of mass generation to support our daily live.

Solar energy is one of the most attractive source among other renewable sources. There are some advantages of solar energy that other type of energy sources cannot be compatible. Solar panel can be used almost anywhere while hydroelectricity, wind power and geothermal are subjected to series of strict geographic requirement. In



addition, there is no need for a large generation station, but simple circuit is enough to support a photovoltaic device for energy extraction. In other words, solar energy can be mobile and is suitable for undeveloped place which does not have electrical grids. Other generation approaches usually rely on turbine or other moving parts which is noisy and liable to mechanical fatigue.

At the beginning of this technological invention, the prototype of photovoltaic device based on inorganic semiconductor p-n junction is expensive, but it has been recommended to be installed on satellites because of its high power-to-weight ratio. Afterwards, this technology has been further applied for energy harvesting to mitigate the energy demand. Up to recent decade, although the fabrication of inorganic photovoltaic is more mature, it is still highly desirable to further reduce the cost of solar cells [1]. In this respect, researchers notice that photovoltaic device must be constructed using materials other than bulk silicon in order to significantly reduce the cost. Therefore, organic semiconductor has been introduced to this field. Based on many processing advantages, the cost can be greatly reduced and the tradeoff is low efficiency due to complete different mechanism and interfacial instability [2] which is the intrinsic problem of organic material.

Some researchers used inorganic semiconductors such as CdSe, TiO₂, PbS, ZnO to make a hybrid junction, because those semiconductors generally provide stable surface and possess high electron mobility [3]. Nano-technology is often employed in the synthesis of organic-inorganic hybrid devices to maximize the interfacial area. To date,



hybrid solar cell has been widely studied for many years.

1.2 Motivation

Commercial solar cells making use of bulk silicon need high purity of material to facilitate the photovoltaic function. Despite of the high efficiency (>25%) and stability of the silicon cell, the harsh synthesis conditions, for instance, high temperature close to 1000°C, inevitably increase the cost and limit the production area. This expensive fabrication hinders the replacement of fossil fuel which is very low cost. Therefore, in recent decades, many research works have been redirected to organic materials.

Several reasons support this action. Firstly, the fabrication of organic materials is low cost and fast because it is solution processable and allows room temperature fabrication. This property makes it available for large area production and is flexible for different substrates. Secondly, the material source is abundant and cheap. Organic materials mainly consist of light elements (carbon, oxygen, hydrogen) and are produced by series of synthetic processes. Lastly, the energy band configuration can be tuned by adding electron donating or accepting functional groups. Based on the data from National Renewable Energy Laboratory, we can see that the solar spectrum covers a wide range of wavelength as shown in Figure 1-1. Tunable bandgap is very useful because energy band configuration governs the light absorption range, junction behavior and the suitable electrode material which are of primary importance in solar cell construction.

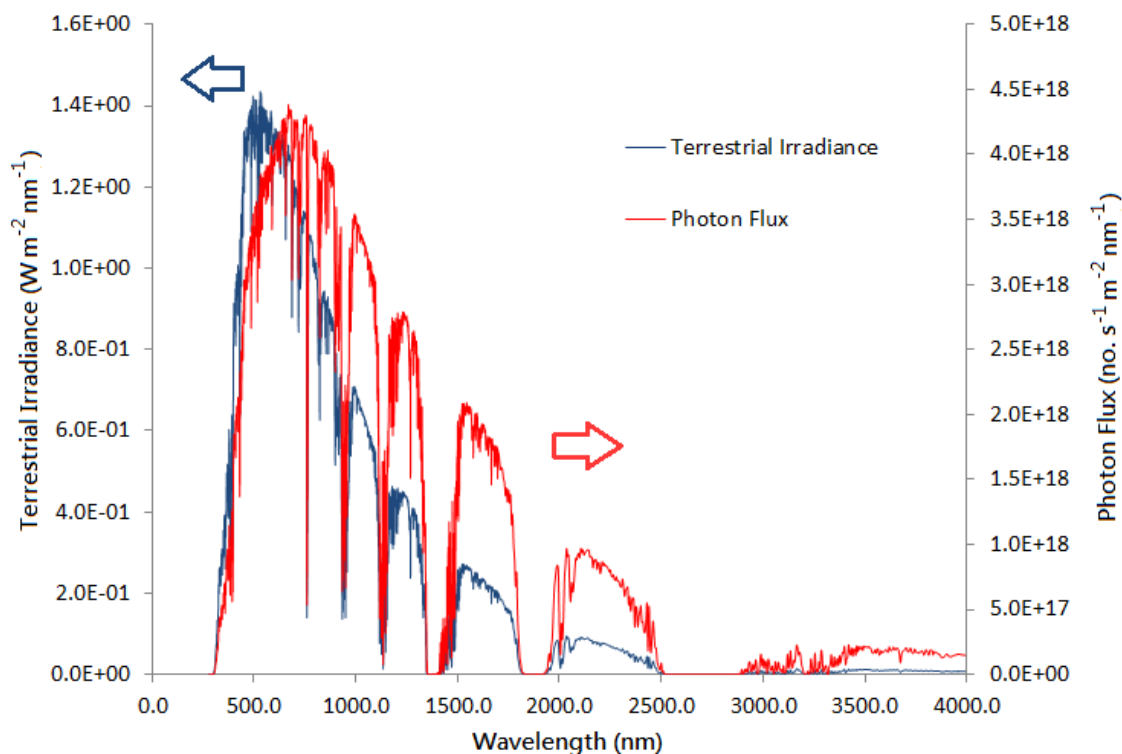


Figure 1-1 Sun light irradiance and photon flux [4].

However, there are some difficulties impeding the application of wholly organic solar cell. The electron mobility of organic material is usually low and the organic-organic interface suffers from phase segregation. Although the extinction coefficient of organic material is high so that thin film is used to boost the collection of carriers, inorganic semiconductor is substituted for organic electron transporter which forms a hybrid solar cell. Inorganic semiconductor commonly exhibits few orders higher carrier mobility than organic counterparts without any doping. In addition, large electron affinity, high dielectric constant and stable surface are also beneficial to the operation and fabrication of photovoltaic devices.



Consider that the bulk heterojunction technique cannot be directly applied to inorganic semiconductor to create large interfacial area junction, in this project, nanotechnology is applied in different ways to construct a photovoltaic device in order to enhance the performance of basic device. Poly(3-hexylthiophene) (P3HT) and titanium dioxide (TiO_2) are used as main building blocks of the solar cells investigated throughout the project for comparison purpose. Nanostructure and interlayer are added to the device aimed to enhance the performance. Besides, transparent back electrode is attempted to replace the traditional metal electrode to make a semi-transparent device which illustrated the feasibility of two way illumination of a single device.

1.3 Overview

The objective of this project is to fabricate hybrid junction solar cells and enhance the cells with different approaches. By systematic control of fabrication condition, the device performance is optimized and the mechanism to enhance its operation is studied.

In Chapter 1, the background of solar cell investigation and development is introduced. It is mainly about the concern for energy crisis and feasibility of commercialization of solar technology. The advantage of hybrid photovoltaic device is discussed.

In Chapter 2, a brief discussion about the theory behind photovoltaic effect is given. The difference in operating principle between traditional photovoltaic device and hybrid



junction device is pointed out. Deriving from the above, the material requirement to boost the device performance and also the limitation of device is discussed.

In Chapter 3, the enhancement by adding nanofibers inside the junction structure is illustrated. Basic principle of fabrication of nanofibers by electrospinning is introduced. The optimal amount of nanofibers beneficial to the operation of device is found out by a systematic work. Different characterization methods are employed to evaluate the structure properties of the junction.

In Chapter 4, surface modification is carried out for further improvement of the optimal device in previous chapter. Electrochemical deposition is introduced to modify the junction interface. The morphology and growth of deposition layer with respect to time is demonstrated by different microscopic techniques. The reason for improvement is discussed based on light response of devices.

In Chapter 5, graphene is used to replace the reflective back electrode of a solar cell and form a semi-transparent device. Transferring process and the problems encountered are presented. Doping of graphene is used to assist the transferring and to solve the junction problem. The performance of device is characterized under various illumination conditions. Probable reasons are suggested about the diversity of light response on different sides.

In Chapter 6, conclusion is drawn upon the work done and findings in this project.



Finally, further work is suggested for further development and investigation.



Chapter 2 Principle of Photovoltaic Device

2.1 Organic conjugated polymers

When the p-orbital of two adjacent atoms (carbon, nitrogen, oxygen or sulfur) of sp^2 hybridization are side-way overlap, it is energetically favored to delocalize two electrons in this overlapped orbital to form a π -bond between these two atoms. A polymer that has a series of π -bonds or delocalized electrons through the backbone is called conjugated polymer. Electrons in such kind of polymer are relatively free and become mobile charges so that the polymer can be conductive and has some meta-stable states [5]. Photons absorbed by the polymer may generate mobile charge carriers which can transport through the polymer matrix. Figure 2-1 shows the chemical construction of four organic semiconductors which are commonly used in photovoltaic devices. They are, from left to right, poly (2-methoxy-5- (3',7'-dimethyloctyloxy)-1,4-phenylene-vinylene) (MDMO-PPV), poly [2,6-(4,4-bis- (2-ethylhexyl)- 4H-cyclopenta [2,1-b;3,4-b'] dithiophene)-alt-4, 7-(2,1,3-benzothiadiazole)] (PCPDTBT), [6,6]-phenyl-C61 butyric acid methyl ester (PCBM) and poly(3-hexylthiophene) (P3HT). Only PCBM has high electron affinity and is an electron acceptor and transporter while all the other behave as electron donor and hole transporter in solar cell applications.

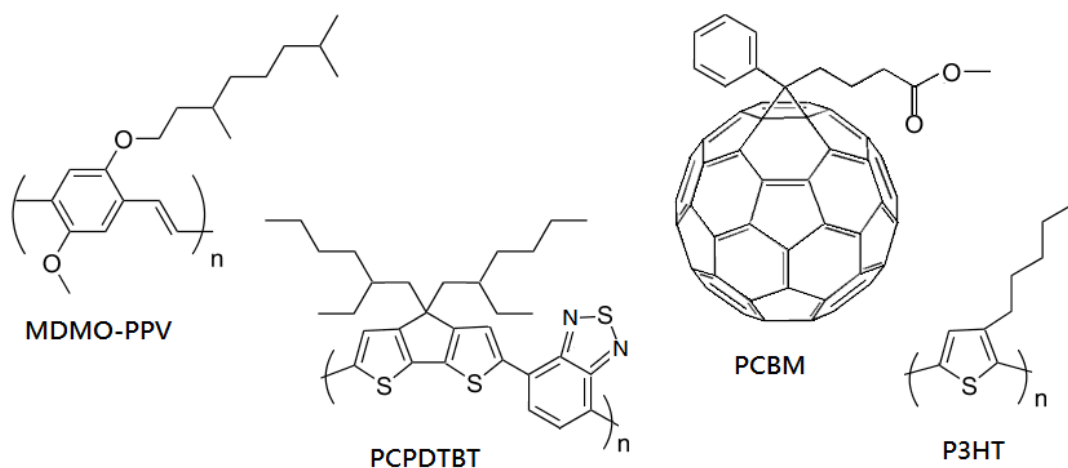


Figure 2-1 Molecular configuration of four common conjugated photovoltaic polymers.

In general, these semiconductors have intrinsic large bandgaps which indicate low intrinsic charge carrier density at room temperature and dark. The light absorption spectrum, unlike inorganic crystalline semiconductors, is a narrow range depending on the inter- or intra-molecular electronic coupling features [6]. As the photon flux peak of solar spectrum is about 700 nm ($\sim 1.8\text{eV}$), small bandgap polymer is desired to absorb larger fraction of light. On the other hand, the high absorption coefficient of organic semiconductor results in that very thin layer (100-500 nm) is enough for effective absorption, while inorganic crystalline semiconductor must be several orders thicker for solar cell application. Another important parameter of solar cell is charge carrier mobility. Polymers of π electron system usually favor hole-transporting except for some polymers with high electron affinity that can be electron transporter [7]. The morphology and crystallinity of the polymer strongly influence the carrier mobility over



several orders of magnitude (from 10^{-6} to $1 \text{ cm}^2\text{V}^{-1}\text{s}^{-1}$) [8].

Physical properties can be tailored in order to simplify the fabrication process. Solubility of polymer in common organic solvent allows the application of many coating and cast methods such as screen printing [9,10], ink jet printing [11,12], dip coating [13] and spin coating. The buckminsterfullerene C_{60} is an example of electron acceptor which has been replaced by its derivative PCBM because of its limited solubility [14]. In addition, all the above cast techniques can be performed under room temperature condition.

2.2 Concept of organic photovoltaic cell

An excitonic solid state solar cell is designed for energy harvesting which involves the conversion of photon energy to electricity. Generally, the active layer of each cell consists of two components including hole transporter and electron transporter. Incident photon absorbed by the active layer creates strongly bound electron hole pair called exciton. The exciton can diffuse within a short distance of typically 1-20 nm before their decay [15]. In such a short range, if there exists an interface of hole transporter and electron transporter, the exciton will be split into free charge carriers. Free holes and electrons follow the path provided by corresponding transporter and move to the anode and cathode, respectively. Each collected free charge gives rise to current flow in the external circuit and gives a little amount of energy output.



By identifying steps in the device operation, it is convenient to recognize the limiting process and find the possibility for improvement. The operation of excitonic solar cell can be divided into seven fundamental physical processes:

- (1) Coupling of the photon
- (2) Photon absorption
- (3) Exciton generation
- (4) Exciton diffusion
- (5) Exciton dissociation
- (6) Charge transportation
- (7) Charge collection

These processes are further explained as follows:

2.2.1 Coupling of photon

Solar cells are commonly constructed in a sandwich fashion and the active layer is placed in between two electrodes and the whole device is isolated from the ambient. Incident light must pass through a transparent substrate and electrode to reach and stimulate the active layer. The thickness of an organic solar cell is just a few hundred nanometers so that the substrate is easily thicker than the device by three to four orders of magnitude. Even a transparent material is applied, reflection must occur at the medium interface. Larger difference in refractive index brings about more serious reflection. Surface antireflection patterning such as pyramidal surface and grating can help to reduce the reflection loss. Furthermore, the device reflection is not only



contributed by the air-substrate interface, but from all layers in the device. Since the thicknesses of layers are close to the scale of wavelength, the layer thickness, ordering and dielectric function can play an important role in this optical behavior [16].

2.2.2 Photon absorption

The active layer should be the only absorber in the device design. It is desirable to have an active layer fully absorbing the solar spectrum. However, organic materials always exhibit strong and narrow characteristic absorption. Besides material synthesis to tune their optical properties, cooperation of materials with different absorption region is beneficial to the device performance. Also, the strong absorption coefficient of organic materials allows complete absorption by a thin layer. The intensity of light passing through a homogeneous medium can be described by:

$$I\alpha = -\frac{dI}{dx}$$

where I is intensity of light beam, α the absorption coefficient and x is travelling distance of the beam. The equation describes that the decrease of intensity with respect to travelling distance is proportional to itself by the absorption coefficient. Combined with the previous step, the absorption efficiency is defined as the ratio of photon number absorbed in the active layer to the number of photon incident on the substrate.

2.2.3 Exciton generation

Electron absorbs the energy of photon and is promoted from a low energy level or the



valence band to a high energy level or the conduction band. The difference of two band edges indicates the minimum energy of photon to induce this promotion. In organic semiconductors, the valence band edge is called highest occupied molecular orbital (HOMO) or first oxidation potential and the conduction band edge is called lowest unoccupied molecular orbital (LUMO) or first reduction potential. After the transition, the promoted electrons and the remaining positive states (holes) are strongly bound by Coulomb interaction and are collectively called excitons. Such exciton is classified as the Frenkel exciton in solid-state physics. Different case is presented by inorganic semiconductors, which have high dielectric constants. The binding energy can be smaller than the thermal energy, and thus free charges are formed instead of bound excitons. Transition 1 in band diagram Figure 2-2 represents the formation of exciton after a photon is absorbed by a polymer or a dye molecule.

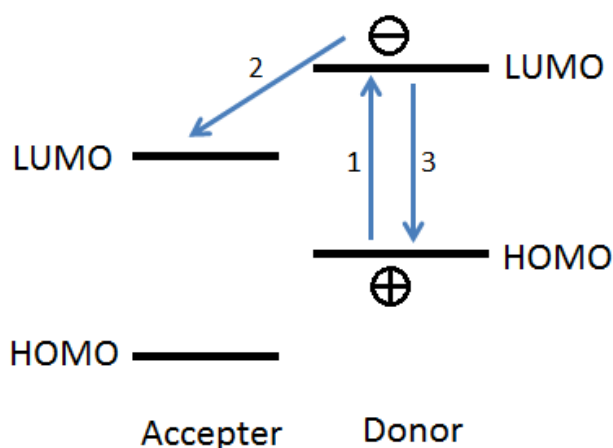


Figure 2-2 Schematic diagram of electron transition.



2.2.4 Exciton diffusion

Exciton can be viewed as a quasi-particle with effective mass. It can move to its vicinity by three-dimensional diffusion during its life time. The diffusion length of exciton in organic semiconductors is very short and depends on the structure and dielectric properties of the material. In order to separate the exciton into free charge carriers, it must reach the dissociation site which is the interface of two materials with offset electron affinity. If the exciton cannot dissociate, it will release its energy by radiative or non-radiative decay. The former mechanism leads to re-emission of photon and results in luminescence of material. Therefore, the quenching of photoluminescence is used as a measure to estimate the dissociation. The latter mechanism leads to vibrational or thermal decay. The exciton diffusion efficiency describes the fraction of excitons which successfully diffuse to dissociation sites.

2.2.5 Exciton dissociation

After an exciton has reached the dissociation site, the electron will be transferred to a lower LUMO because it is energetically favored, while the hole remains. The material with smaller electron affinity is called electron donor and that with higher electron affinity is called electron acceptor. It is represented by transition 2 in Figure 2-2. Systematic analysis has been reported about the efficiency of dissociation. It finds that the difference of LUMO should be at least 0.3 eV to give efficient dissociation [17]. A counter process of dissociation is the geminate recombination of the exciton. Transition 3 in Figure 2-2 represents this recombination. The separated electrons and holes merge



back because of the field is not strong enough to resist the electrostatic force.

2.2.6 Charge transportation

Free charge carriers should transport to corresponding electrode in order to be collected. However, trapping state may be present to localize the free charge during the transportation. The trapping increases the possibility of bimolecular recombination which describes the recombination of free charges from different excitons. In addition, the transport of electrons and holes is also influenced by the mobility in the material. Organic semiconductors normally possess higher mobility of hole than electron so that they are always employed to be hole transporter in hybrid junction and inorganic phase is used as electron transporter. If considerable free charge carriers are retained in the active layer by whatever means, it leads to the build-up of electric field facilitating the recombination in the device.

2.2.7 Charge collection

The final step is charge carrier extraction from the device by electrode. To facilitate the extraction of charge carriers to correct electrode, carrier blocking layer is often employed to selectively transport one type of carrier to the electrode. Moreover, it is believed that the Fermi level of the metal electrode should be as close as possible to the LUMO of the acceptor and the HOMO of the donor to give efficient charge extraction. The charge collection efficiency counts this process and the previous one together to



give the number fraction of collected carriers and the dissociated excitons.

2.3 Photovoltaic parameters

2.3.1 External quantum efficiency (EQE)

The conversion of photon to electron is evaluated by quantum efficiency. The ratio of the number of incident photons to that of output electrons is called incident photon conversion efficiency (IPCE) or EQE.

$$EQE = \frac{\text{number of electron}}{\text{number of photon}} = \frac{J}{P} \times \frac{hc}{e\lambda}$$

where J is photocurrent density in A/m^2 , P incident photon intensity in W/m^2 , h the Planck's constant, c the speed of light, e the elementary charge of electron and λ is the wavelength of light. Since the response of device varies over different wavelengths, EQE is often measured as a function of wavelength by monochromatic light. Its shape would be similar to the absorption spectrum of the active layer.

Although EQE is only an observation of input photons and output electrons, it can be divided into a series of efficiency of involved operation steps.

$$EQE = \eta_A \eta_{ED} \eta_D \eta_C = \eta_A IQE$$

where η_A is the absorption efficiency of the active layer, η_{ED} the exciton diffusion efficiency to dissociation site, η_D the dissociation efficiency and η_C is the charge collection efficiency. Product of the last three can be combined to internal quantum efficiency (IQE) which is defined as the ratio of absorbed photon number to the number



of output electrons.

It seems that the efficiency or current density of a solar cell can be calculated by integration of EQE over the photon flux (N_{ph}) of solar spectrum. However, this method fails. By definition, the value of EQE is unrelated to the light intensity, but it is practically varying non-linearly with illumination intensity. The monochromatic light intensity during the measurement is not comparable to the intensity of full spectrum illumination. Hence, the monochromatic light EQE will not exactly be equal to the EQE under real application. This implicit dependence of photocurrent is called space charge limited photocurrent and has been investigated by Mihailetchi *et al.* in 2005 [18,19].

2.3.2 Current density versus voltage (J-V) characteristics

The efficiency of solar cell is measured under a solar simulator which reproduces the solar spectrum. To evaluate the efficiency of a solar cell, J-V characteristics of the cell under standard illumination are measured. Figure 2-3 shows a typical J-V curve of a solar cell. There are many analytical studies giving a modeling of current as a function of voltage.

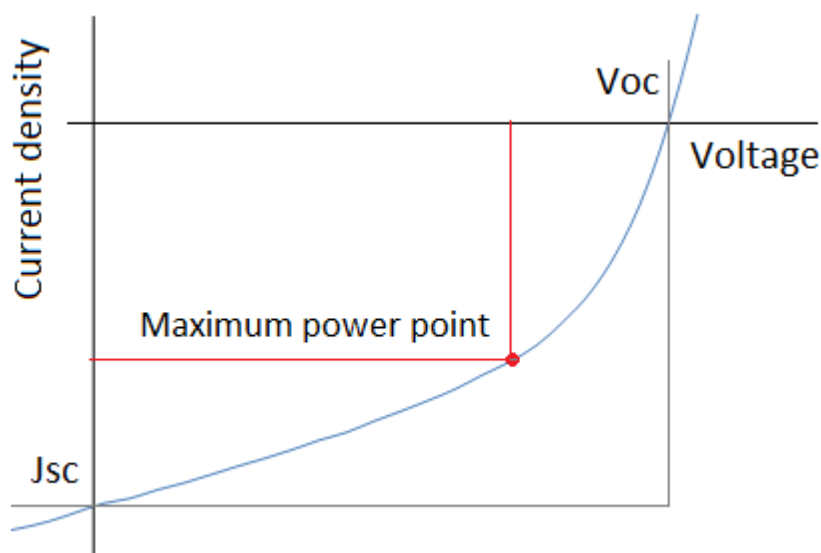


Figure 2-3 Typical J-V characteristics of a solar cell.

The y-intercept of the J-V curve is called the short-circuit current density (J_{sc}). It represents the maximum amount of electron flow in external circuit raised by illumination on the solar cell. The integration of EQE gives a theoretical upper limit of this parameter rather than an actual value.

$$J_{sc} = e \int EQE(\lambda) \times N_{ph}(\lambda) d\lambda$$

Open-circuit voltage (V_{oc}) indicates the maximum energy carried by a unit charge. Improving V_{oc} remains a problem in the design of photovoltaic cell structure. It is commonly believed that it is linearly related to the difference between LUMO of the acceptor and HOMO of the donor [20]. Therefore, new conjugated polymer synthesized with a low HOMO is desired. Another way to improve V_{oc} is construction of multi-junction in a single device named as tandem cell. The resulting V_{oc} is the sum of



individual junction. A tandem structure achieving 1.56 V of V_{oc} has been constructed by Jan Gilot *et al.* [21].

To evaluate the performance of a device, fill factor (FF) is an important parameter indicating the quality of device structure. It can be illustrated in any J-V curve as shown in Figure 2-3 that the area ratio of the rectangle defined by maximum power point (MPP) and the rectangle defined by J_{sc} and V_{oc} .

$$FF = \frac{J_{MPP}V_{MPP}}{J_{SC}V_{OC}}$$

It is obvious that the position of MPP is considerably influenced by the FF under similar V_{oc} and J_{sc} values. The reciprocal of slope near V_{oc} indicates the series resistance of the device. The series resistance results in internal voltage loss during the operation. At short circuit condition, the reciprocal of slope represents the shunt resistance, therefore, non-zero slope is undesirable. In the study of carrier dynamic and recombination processes, it is shown that the recombination process leads to tilting of the low voltage region of the J-V curve [22,23]. The ideal photovoltaic device with FF close to 1 must has weak recombination, small series resistance and low shunt current loss.

Finally, the photo-current conversion efficiency, η , is determined by the product of J_{sc} , V_{oc} and FF divided by the incident photon power density, P_{in} .

$$\eta = \frac{J_{SC}V_{OC}FF}{P_{in}} = \frac{J_{MPP}V_{MPP}}{P_{in}}$$



2.4 Organic-inorganic hybrid junction and junction morphology

In the development of solar cells, the junction morphology has played a crucial role in determining the performance of a photovoltaic cell, especially in hybrid junction. After the development of bilayered structure (Figure 2-4 (a)) [1], researchers realize that the interface in an organic solar cell allows exciton dissociation and they want to increase the contact area of electron transporter and hole transporter in a finite device size. Compared with other efficiency enhancement strategies such as dye sensitizing or blocking layer, it gives more fundamental effect on the device operation.

In full organic solar cells, electron and hole transporters can be dissolved in the same solvent and deposited simultaneously. This method forms intimate bicontinuous nanostructure by self-assembly property and results in disorder bulk heterojunction as shown in Figure 2-4 (b). The efficiency can be drastically increased to 4-5% by this junction morphology [24]. It is believed that hybrid junction can provide similar improvement by increasing the contact area. Nanoparticles [25], nanorods [26,27], nanofibers [28,29] and also porous structure [30,31] have gradually arisen and been investigated in order to get denser interface.

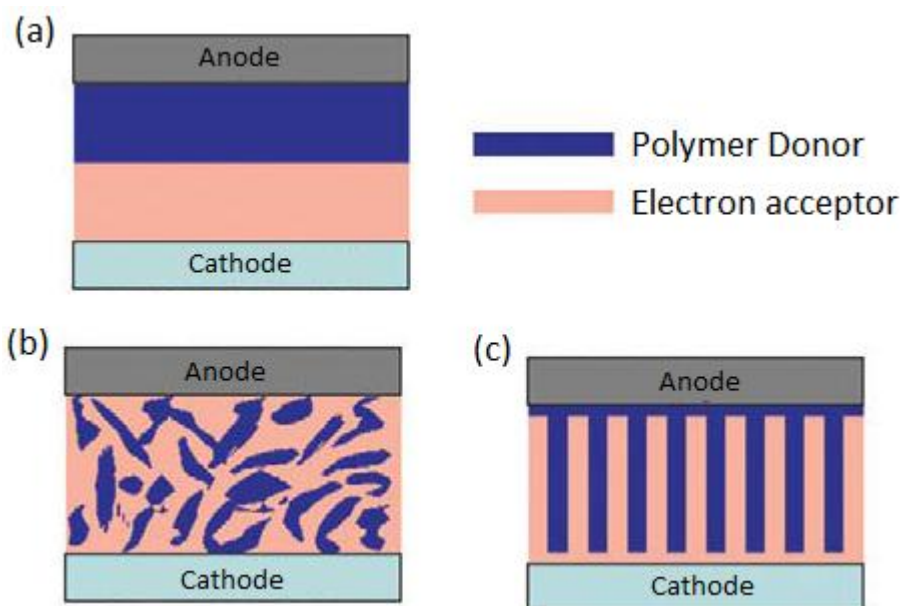


Figure 2-4 Schematic diagram of (a) bilayered junction, (b) disorder bulk hetero-junction and (c) order structure of solid state solar cell.

2.4.1 Nanoparticle junction

Nanoparticles embedded in a polymer matrix are a straightforward ideal to substantially increase the interfacial area owing to the high surface to volume ratio of nanoparticles. Cadmium selenide (CdSe), zinc oxide (ZnO) and TiO₂ have been used to form such composite film with different donor polymers. Greenham *et al.* observed photoluminescence quenching when MEH-PPV intermixes with 5 nm CdSe nanoparticles [32]. Figure 2-5 (a) shows the TEM image of CdSe nanoparticles in MEH-PPV. The efficiency of device is approximately 0.1% at AM1.5 condition with 80 mW/cm². Researchers realized that the efficiency is improved as the weight fraction of nanoparticles is increased. It leads to a conclusion that electron transport in



discontinuous nanoparticles by hopping is the limiting process in the device operation.

This phenomenon also occurs in ZnO and TiO₂ nanoparticle hybrid junction.

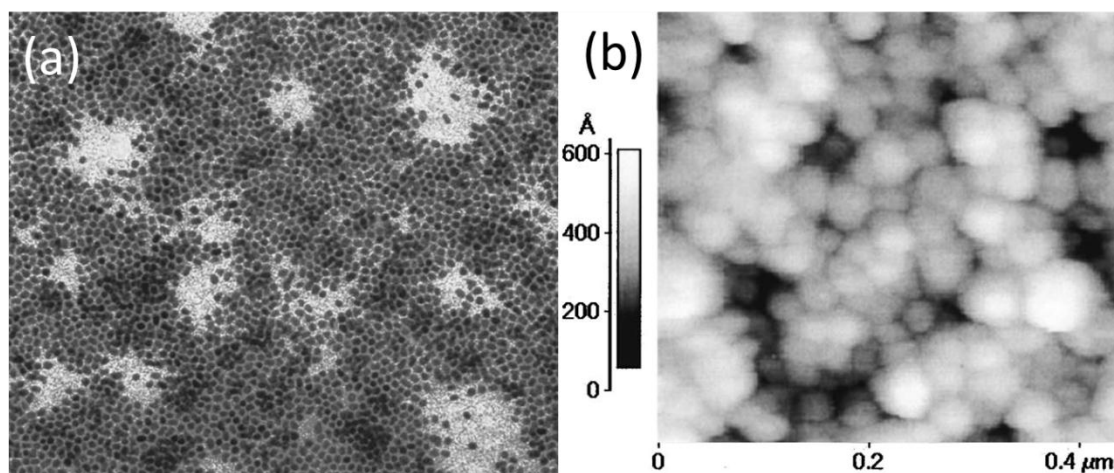


Figure 2-5 Microscopic image of nanoparticles [32,33].

In 2001, Breeze *et al.* studied the effect of mobility and morphology on the properties of the device consisting of MEH-PPV and 13 nm TiO₂ nanoparticles as the active layer [33]. Figure 2-5 (b) is the AFM image of the TiO₂ nanoparticle layer. The device demonstrates J_{sc} of 0.4mA/cm², V_{oc} of 1.1V, FF of 0.4 at illumination intensity of about 100mW/cm². They point out that short exciton diffusion length and low carrier mobility are the primary limitations of this device. Similar morphology of ZnO accompanied with electron blocking layer was investigated by Waldo *et al.* in 2004 [25]. The efficiency of optimum device is greatly improved to 1.6%. They show the importance of electron blocking layer which allows high fraction of ZnO and current density without concurrent drop of V_{oc} .



2.4.2 Nanorod junction

The involvement of nanorods began in 1999 when Huynh *et al.* observed the improvement of composite film conductivity caused by slightly increase of aspect ratio of CdSe nanoparticles [34]. The effect is attributed to longer electron transport pathway and reducing the number of interparticle hopping. Few years later, Huynh *et al.* gave a remarkable work that 7 nm by 60 nm CdSe nanorods are blended with regioregular P3HT [26]. The device gives power conversion efficiency of 1.7% under AM1.5G solar condition with Voc of 0.7 V and FF of 0.4. The absorption edge is at 720 nm. About the efficiency peak, the EQE of wavelength at 515 nm reaches over 54%. A monochromatic light at this wavelength with intensity of 0.1 mW/cm² provides power conversion efficiency of 6.9% and Voc of 0.5 V.

In 2008, Chang *et al.* investigated the microscopic mechanisms of charge separation and transportation of TiO₂ nanorod with 20 - 40 nm in length and 4 nm in diameter blended in P3HT [35]. The weight fraction was optimized as 50%, in which both electron and hole mobility in the composite are maximized and less dispersive with electric field. However, the device shows only 0.17% efficiency with Voc of 0.58V, Jsc of 0.91 mA/cm² and FF of 0.32. They further improved the device performance by thermal annealing and removal of insulating surfactant. The device exhibits a high power conversion efficiency of 1.14% with Voc of 0.69V, Jsc of 2.62 mA/cm² and FF of 0.63. Next year, they reported an application of dye sensitizing technique on this structure [3].



Different ligands are attached on the surface of TiO_2 nanorods with similar size to previous report. The best device gives efficiency of 2.2% with V_{oc} as high as 0.78V and J_{sc} 4.33 mA/cm^2 under 100 mW/cm^2 .

2.4.3 Ordered junction

In order to occupy more nanocrystals with higher aspect ratio, researchers seek an ordered heterojunction rather than dispersive structure mentioned above. Such ordered structure can be nanorod array, aligned nanofiber, regular pores, etc. Figure 2-4 (c) shows an example of nanorod array structure. Ideally, short direct channels can be provided to charge carriers to corresponding electrodes. Therefore, TiO_2 and ZnO attract more attention because they can easily be synthesized and grown in different shapes, available for modification and are also non-toxic. Figure 2-6 shows various ordered nanostructures for hybrid solar cell applications.

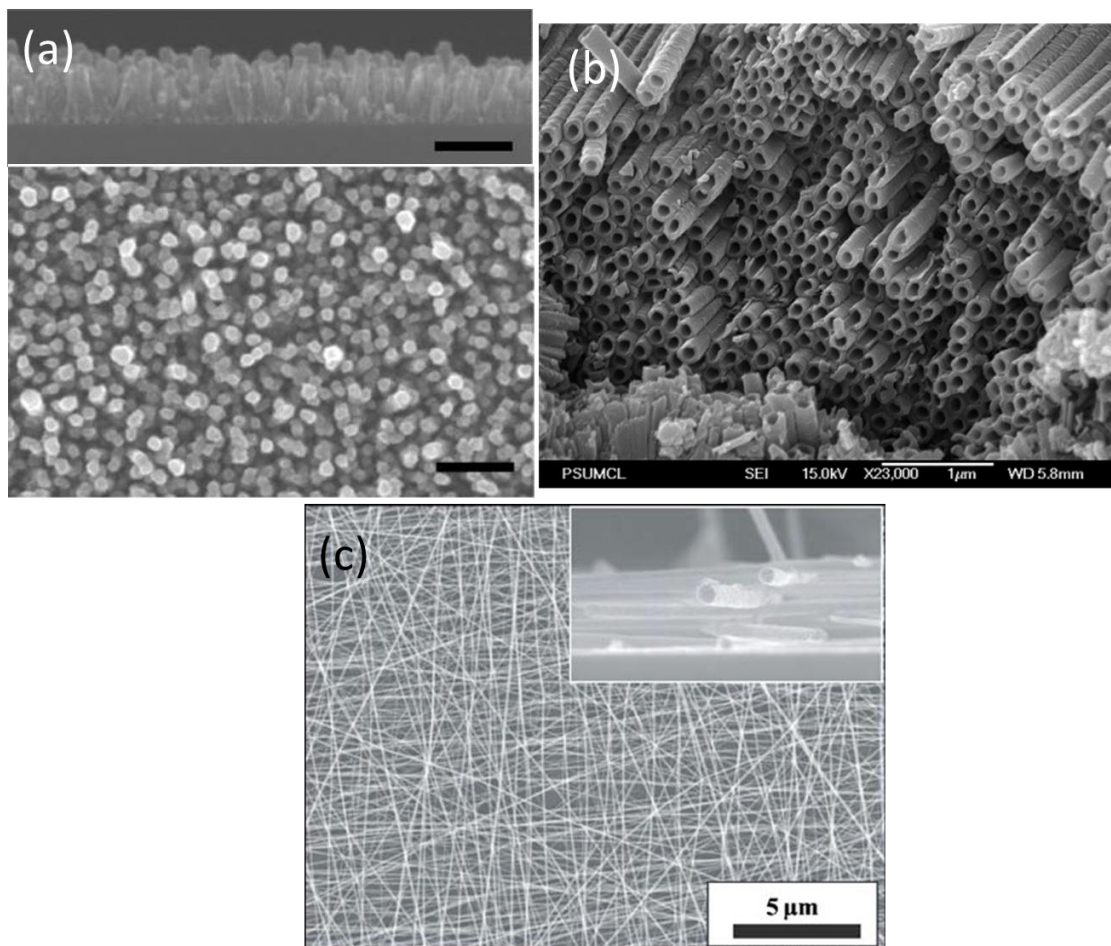


Figure 2-6 Morphology of ordered structure for hybrid solar cells. (a) ZnO/TiO₂ nanorod [36], the scale bar represents 200 nm. (b) TiO₂ nanotube [37] and (c) cross-aligned TiO₂ nanofibers [28].

Greene *et al.* demonstrated the performance of hybrid photovoltaic device using ZnO-TiO₂ core-shell nanorod structure with P3HT [36]. The ZnO nanorods are 150 - 225 nm long and 15 - 25 nm in diameter and the thickness of TiO₂ shell is within 20 nm. Figure 2-6 (a) gives the SEM images of side view and top view of the nanorod array. The devices show acceptable FF of 0.5 - 0.55 and Voc of 0.45 - 0.5 V, but low current



density suppressing the overall efficiency to less than 0.3%. Researchers proposed a possible reason that the nanostructure contributes little absorption of light. Another group showed a hybrid solar cell using 4 μm long TiO_2 nanotube array grown by anodizing Ti foils [37]. A SEM image of the nanotubes is shown in Figure 2-6 (b). They filled the nanotubes with a blend of P3HT and C60-methanofullerene resulting in double junction in the device. Electron blocking is also employed. It gives a maximum IPCE of 53% in the visible region and high J_{sc} of 6.5 mA/cm^2 under AM1.5 illumination condition. However, the efficiency is limited to about 1% by the low V_{oc} and FF. The nanorod and nanotube arrays are perpendicular to the substrate, while Shim *et al.* investigated an ordered structure laid on the substrate surface [28]. They fabricated a device consisting of TiO_2 nanofibers and MEH-PPV to study the influence of nanofiber alignment. Cross-aligned TiO_2 nanofiber is shown in Figure 2-6 (c). Their results point out that the alignment of nanofiber significantly increases the current density of the device and slightly reduces the generated voltage, while the FF remains similar in all devices which is about 0.5. The device with aligned nanofibers exhibits an overall power conversion efficiency of 0.41% which is 70% higher than that with random nanofibers.

2.4.4 Porous junction

The last important morphology is TiO_2 porous structure which has also been investigated for a long time, because dense and large interface accompanied with continuous interpenetrating network is provided for both electron and hole. In 1998,



Bach *et al.* described a dye-sensitized mesoporous TiO₂ heterojunction with an amorphous organic hole transporter 2,2',7,7'-tetrakis(N,N-di-p-methoxyphenyl-amine)-9,9'-spirobifluorene (OMeTAD) [38]. This device gives a strong response in the visible region and a maximum EQE of 33%. Under weak light illumination (9.4 mW/cm²), the FF is 0.62 and overall efficiency is 0.74%. It is an impressive result at that time. Afterward, the carrier transport properties of porous TiO₂ with organic materials are studied by other research groups [39,40].

Recently, Moon *et al.* in Switzerland and Chang *et al.* in Korea reported high performance sensitized porous TiO₂ solar cell with efficiency of 4.4% and 5.1%, respectively [41,30]. The former group uses organic dye and OMeTAD as hole transporter to give Voc of 0.8 V, Jsc of 9.64 mA/cm² and FF of 0.57, while the latter group uses inorganic Sb₂S₃ crystallites as sensitizer and P3HT as hole transporter to give Voc of 0.65 V, Jsc 13.0 mA/cm² and FF of 0.61. To compare their performance, the IPCE or EQE of the former one in Figure 2-7 (a) is rather flat and responds weakly to wavelength longer than 600 nm. In Figure 2-7 (b), since Sb₂S₃ contributes extra absorption in the red light region beginning at 700 nm, the lower Voc in the latter one is compensated by the increase in current density.

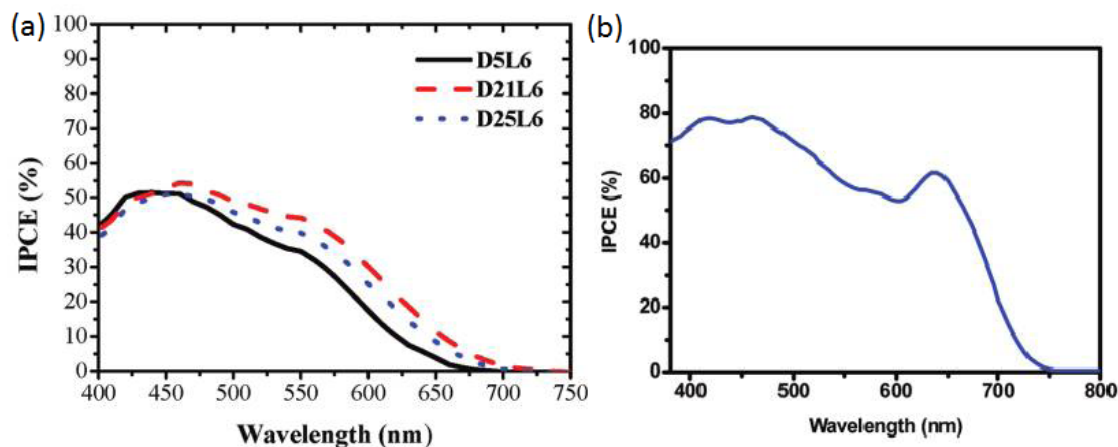


Figure 2-7 IPCE of porous TiO₂ device. (a) TiO₂/organic dye/OMeTAD and (b) TiO₂/Sb₂S₃/P3HT [41,30].

2.5 Characterization method

2.5.1 J-V characteristic measurement

The solar radiation well matches the black body radiation at about 5800K. When it penetrates through the atmosphere, part of it, especially ultraviolet, is absorbed or scattered by gas molecule such as H₂O, O₂ and O₃. Therefore, the solar spectrum reaching the sea level is strongly confined in the visible to infrared region. The air mass (AM) coefficient indicates the effective optical path length compared with the thickness of Earth's atmosphere. It is used for specification of terrestrial solar illumination condition. The standard spectrum is given by American Society for Testing and Materials (ASTM) and government research and development laboratories. The AM1.5 (Figure 1-1) standard spectrum, corresponding to the sunlight received at an angle of 48.19° from zenith, is used as a common illumination condition for solar cell



characterization.

The performance of solar cells is measured under the condition of AM1.5 of 100 mW/cm² reproduced by a Newport 91160 solar simulator equipped with Xenon arc lamp and AM1.5 filter. The Xenon arc lamp is the most common light source for solar simulation, because it gives high intensity and unfiltered spectrum close to sunlight. A standard silicon solar cell is utilized for the light intensity calibration. Solar cells are connected to a Keithley 2400 source meter to give a voltage bias on the devices. Generally, the ramping voltage is ranged from -0.5 V to 1 V.

2.5.2 EQE measurement

A schematic diagram of EQE measurement is shown in Figure 2-8. The monochromatic light is generated by an Oriel 66902 300W xenon lamp through a Newport 66902 monochromator. The light comes from a narrow aperture is recorded and calibrated by a silicon photodetector connected to a Newport 2931_C dual channel power meter. After calibration, the solar cell fixed on holder is placed at the same position of the photodetector to ensure that the same illumination is projected on the solar cell. The response is recorded by another channel of the power meter. The calibration and measurement is performed in dark so that the monochromatic light is the only source of light. In general, the measurement is carried out over 300 – 800 nm with steps of 10 nm.

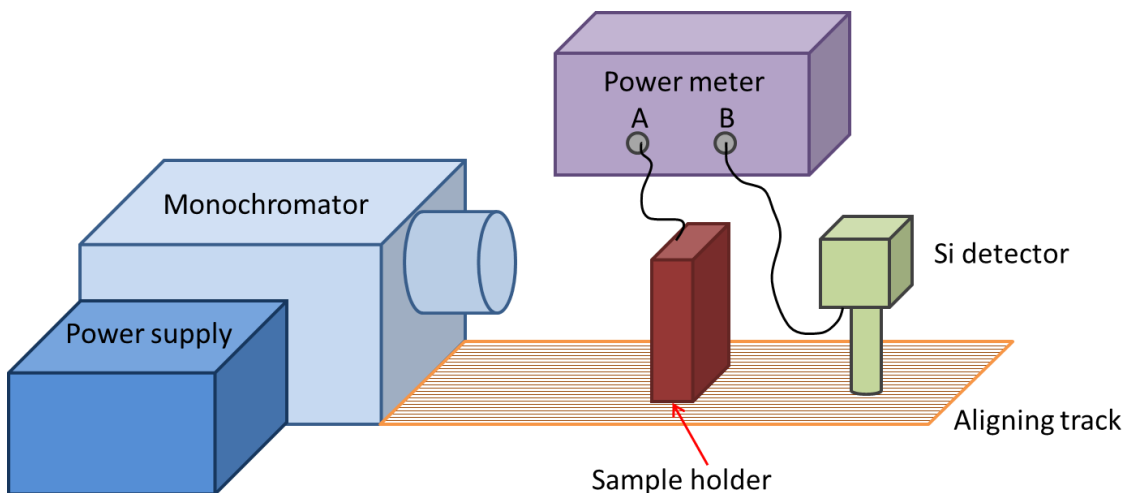


Figure 2-8 Schematic diagram of EQE measurement.

2.5.3 Scanning electron microscopy (SEM)

The SEM technique provides a simple and non-destructive way to study the structure and surface features in sub-micron scale. High energy electron beam produced by the filament hits on the material surface and interacts with the interior atoms of the material. The interaction volume depends on the atomic mass of the constituent. Figure 2-9 roughly shows the shape and size of it. Rebounded electrons and electromagnetic wave come from different regions of the interaction volume and carry different material information.

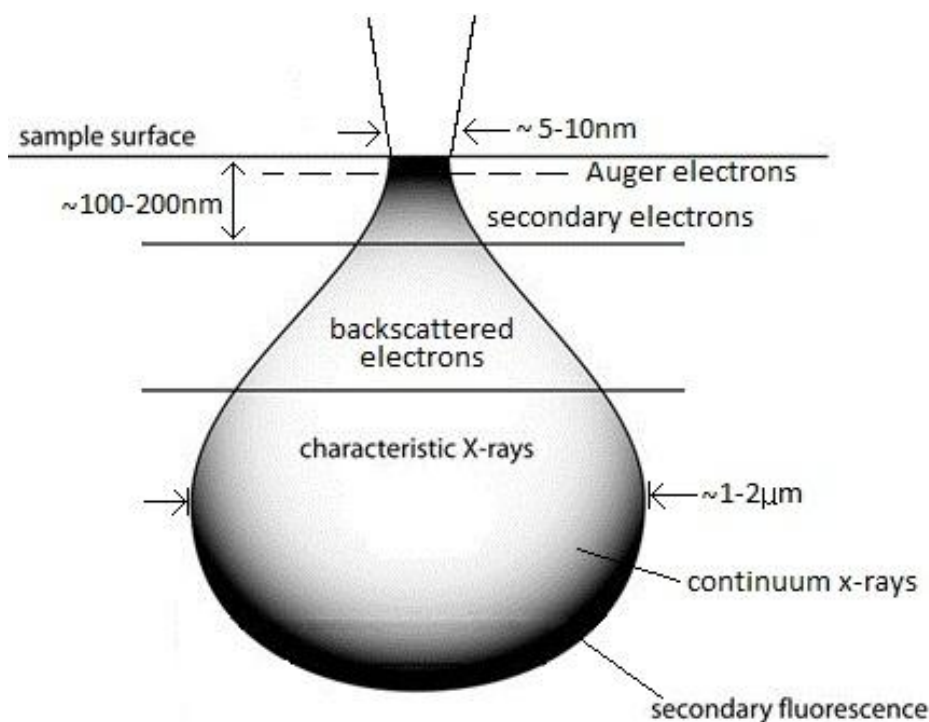


Figure 2-9 Interaction volume of electron beam.

Typically, secondary electrons would be collected for surface imaging. It is produced by inelastic scattering at the material surface. Therefore, it can reflect the morphology of the sample. By continuously scanning the electron beam on the sample surface and collecting the secondary electron signal, the details of surface can be visualized in a relatively large area. Besides, the resolution of SEM depends of the conductivity of target material. If the sample is non-conducting, it will be charged up by the electrons and the trajectories of electrons will be deviated. Practically, this problem is solved by a thin coating of gold to give a conducting surface. Although TiO_2 is semi-conducting, the coating can avoid accumulation of local charges to give higher resolution. Samples are



stuck on conducting carbon tape and viewed by a JSM-6335F Field Emission Scanning Electron Microscope.

2.5.4 Transmission electron microscopy (TEM)

If the electron beam hits a target sample with very thin thickness about few hundred nanometers, the interaction volume shown in Figure 2-9 is no longer completed. Most of the electrons penetrate the target without deviation of their path, but some of them are diffracted by the crystallite of the target and obey the Bragg's law:

$$\sin \theta = \frac{n\lambda}{2d_{hkl}}$$

where θ is the scattering angle, n an integer representing the order of diffraction, λ the de Broglie wavelength of electrons and d_{hkl} is the distance between crystal planes. And, the de Broglie wavelength depends on the accelerating voltage of the electron beam:

$$\lambda = \frac{h}{(2Vem_0)^{1/2}}$$

where h is the Planck's constant, V the accelerating voltage of electron beam, e the elementary charge of electron and m_0 is the mass of electron. For electron beam accelerated by 50 kV potential, the de Broglie wavelength is only about 0.05 Å. The crystal structure of the target can be distinguished by the obtained diffraction pattern.

The morphology and crystal phase of samples are characterized by a JEOL JEM2010 Transmission Electron Microscope. The resolution of TEM is very high in sub-nanometer scale. This resolution is sufficient to probe the atomic configuration and



defect. Also, some X-ray signals are generated and can be collected to analyze the composition of the target. This technique is called energy-dispersive X-ray spectroscopy (EDX). Since the atomic configuration and orbital energy of an atom are unique, the X-ray emitted from different atoms can be recognized.

2.5.5 Ultraviolet – visible (UV-vis) spectroscopy

The UV-vis light absorption of material is directly related to the electron jump from valence band to conduction band or, in conjugated polymer, from π -bonding orbital to anti-bonding orbital, because the photon energy of this part is about 2 – 4 eV and matches the bandgap energy of most semiconductor. Hence, by continuously varying the wavelength of incident beam and measuring the transmission, the bandgap of semiconductor can be determined. The absorption and reflection in this range govern the color of the substance. In organic semiconductors, the absorption profile is of significant importance for the optoelectronic application, because they often have complicated electronic transitions and confined optically active range. The complementary technique is fluorescence spectroscopy which observes the electron transition from excited state to ground state.

A spectrophotometer consists of a continuous radiation source such as tungsten filament, deuterium arc lamp or xenon arc lamp. The light is separated in different wavelengths by a diffraction grating or prism and then filtered to be single wavelength. The transmittance of a sample is defined as the intensity ratio of the transmitted beam



and the original beam. Samples are measured by a Shimadzu UV-2550 UV-VIS spectrophotometer, which is in double beam configuration. Before the beam reaches the sample, it is split into two equal beams. One acts as reference beam and is assumed to be 100% transmission. Another one is sent to the sample. The obtained transmittance is the comparison of the intensity of these two beams.



Chapter 3 TiO₂/P3HT Hybrid Junction Solar Cell

3.1 Introduction

A simple TiO₂/P3HT hybrid junction solar cell can easily be constructed by stacking each layer on the starting substrate which is indium tin oxide (ITO) coated glass. ITO is a transparent conductor with good physical and chemical stability used to be the front electrode of solar cell. Considering the energy band structure of TiO₂ and P3HT (Figure 3-1 (a)), ITO and gold (Au) are chosen to attach to TiO₂ for electron collection and P3HT for hole collection. As mentioned previously, there are different methods to increase the interfacial area between the donor and acceptor material. Therefore, cross-aligned TiO₂ nanofibers are designed to build a porous TiO₂ film for infiltration of P3HT. The schematic diagram of device construction is shown in Figure 3-1 (b).

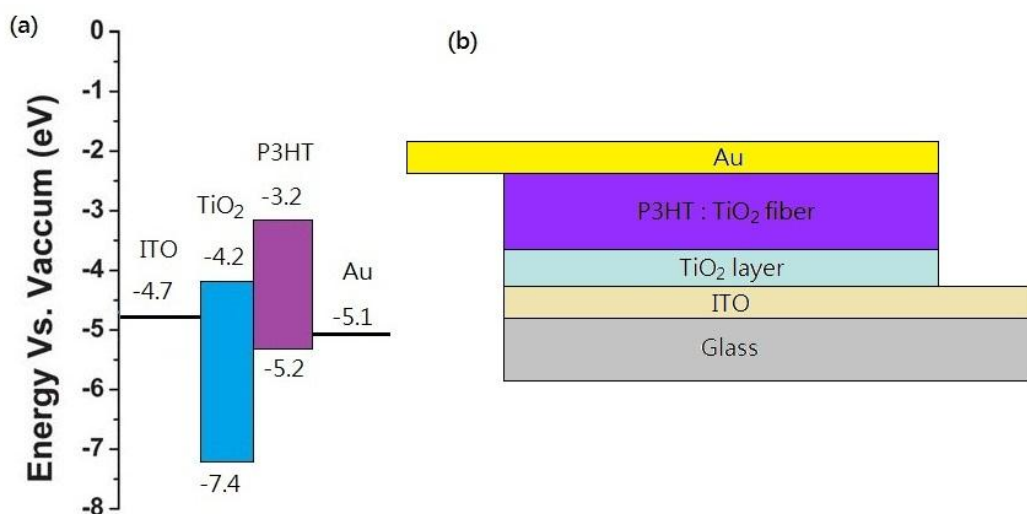


Figure 3-1 Band diagram (a) and schematic diagram (b) of P3HT/TiO₂ device.



In this device, sun light coming from the bottom will pass through the ITO coated glass and reach the active layer. Because of the large bandgap of TiO₂, this layer will only absorb ultra-violet and high energy photon ($>3.2\text{eV}$) and is transparent to the rest. For this reason, TiO₂ will not obstruct the absorption of P3HT which will absorb large portion of visible light. Both of them can generate exciton for dissociation by their own absorption. After the dissociation at P3HT and TiO₂ interface, electrons and holes will be collected by ITO and Au, respectively. As the valence band edge of TiO₂ is very low, holes from P3HT cannot transport to it. This property dictates holes to diffuse toward another electrode only, and thus TiO₂ is commonly used as hole blocking layer in solar cell application. Among various metal, the Fermi level of Au is very close to the HOMO of P3HT and ohmic contact is formed so that it is more suitable as hole collecting electrode of P3HT.

3.2 Properties of TiO₂

Titanium oxide or titania, appears as white solid in the bulk, is a versatile material used in our daily lives in many ways, for examples, sunscreen, food coloring, cosmetics, etc. Recently, more potential applications (air purification [42], water treatment [43], self-cleaning coating [44-47]) based on its photocatalytic effect have attracted substantial research interest. Non-toxic, simple synthesis and slow recombination rate of charge carrier [48] are also important advantages of it.

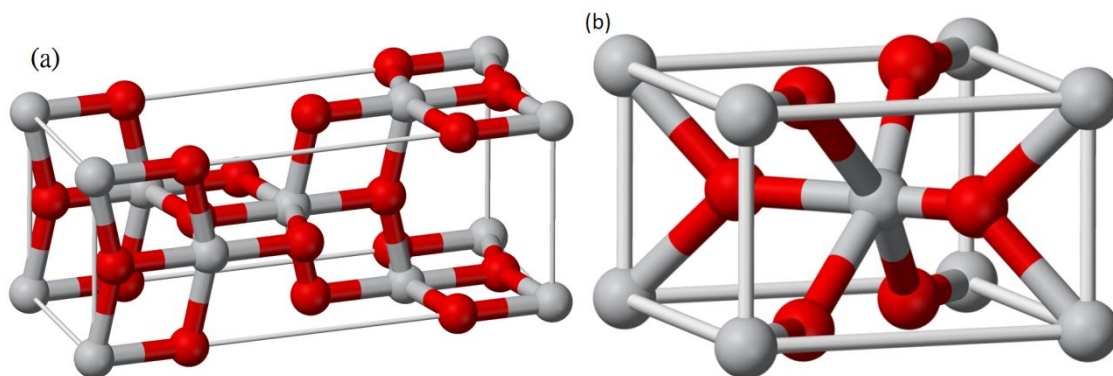


Figure 3-2 Unit cell of (a) anatase [49] and (b) rutile [50].

At atmospheric pressure, TiO₂ exists in three polymorphs, rutile, anatase and brookite [51,52]. All of them are tetragonal and consist of TiO₆ octahedra in different constructions. There are also a number of phases reported at high pressure [53,54]. Brookite is difficult to synthesis and study [55] so that most daily applications only involve rutile and anatase phases. The atomic configuration of rutile and anatase are shown in Figure 3-2. Rutile is the most stable phase at all temperatures [53,56].

Table 3-1 gives a comparison of material parameters of anatase and rutile. Both anatase and rutile have indirect bandgap and absorb ultraviolet light. For solar cell construction, both phases have a suitable bandgap, but the effective electron mass of anatase is significantly smaller than that of rutile. The electron mobility μ_e and diffusion constant of anatase governed by effective electron mass should be considerably higher than that of rutile. Therefore, anatase is preferable in the construction of active layer.



Table 3-1 Material parameters of rutile and anatase [57,58].

	Anatase	Rutile
Atoms per unit cell	4	2
Lattice parameter (nm)	a = 0.3785	a = 0.4594
	c = 0.9514	c = 0.2959
Density (kg*m ⁻³)	3894	4250
Experimental bandgap (eV)	3.2	3
Refractive index	2.5	2.85
Effective electron mass (m _e)	1	20
Dielectric constant	31	100

The phase of TiO₂ greatly depends on the synthesis conditions. In order to well control the microstructure of TiO₂, the kinetics in anatase to rutile transformation is widely studied especially for high temperature applications. Although experiments show different onset of the transformation depends on the process and measuring method [59,60], it is widely accepted that bulk anatase will begin to transform to rutile at 600°C in air [52,59]. John C. Jamieson and Bart Olinger performed thermodynamic study on TiO₂ and proposed the phase diagram of it as shown in Figure 3-3.

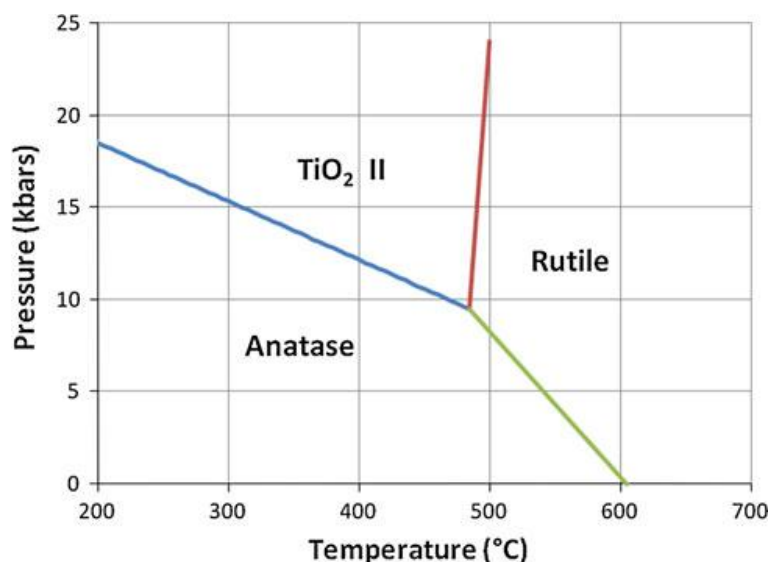


Figure 3-3 Phase diagram of TiO₂ [51].

To evaluate the phase component of the synthesized TiO₂, X-ray diffraction (XRD) is often carried out to determine weight ratio of the two phases W_R/W_A . Such semi-quantitative analysis is known as the method of Spurr and Myers [61], which used an empirical formula shown below:

$$\frac{W_R}{W_A} = 1.22 \times \frac{I_R}{I_A} - 0.028$$

I_R/I_A is an intensity ratio of rutile (110) peak to anatase (101) peak. However, the signals collected from XRD vary with many other factors so that the result is not very accurate. Owing to distinct Raman spectra of those phases, laser Raman microspectroscopy is also commonly employed for the same purpose [62,63].

3.3 Properties of P3HT

Poly (3-hexylthiophene) (P3HT) is a most widely studied conducting polymer. The



bandgap is about 1.9eV in well crystallized solid state, corresponding to 650 nm wavelength. Many potential uses of P3HT have been proposed such as thin film transistors [64,65], light emitting diodes [66], photoelectric cells [67,68] and etc. Investigations about P3HT find that the optical and electrical properties of P3HT can be largely influenced by molecular conformation and polymer chain arrangement.

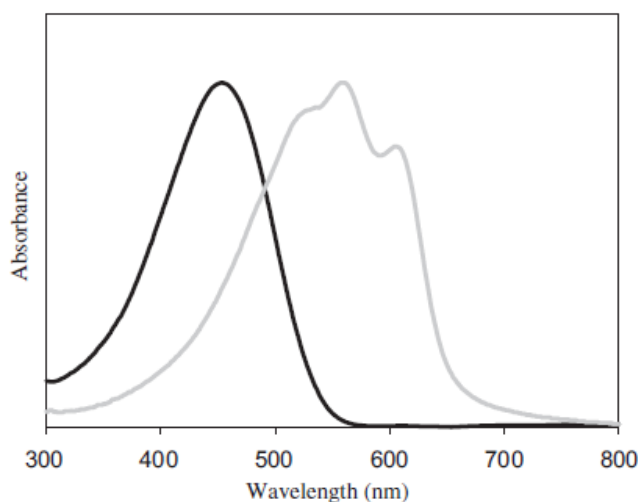


Figure 3-4 Absorption spectra of P3HT in solution (black) and in solid state (grey) [69].

The conjugation of polythiophene is planar along the thiophene ring so that the conduction of its family is one dimensional. P3HT, as the derivative of polythiophene, shares the same conducting properties so that twist or bend also cause shorter conjugation of the polymer. It is known that the longer conjugation will absorb light with longer wavelength and reduce the transition energy [70]. Some researchers try to figure out the saturation conjugated length of bandgap shift. However, a tiny red shift of



absorption maximum is still observed from 72 units to 96 units [71]. Then, they draw a conclusion that a large number of monomers is required to converge the bandgap of this polymer family. In addition, P3HT exhibits significant difference in absorption and bandgap in solution and in solid film (Figure 3-4) [69]. This reveals the influence of polymer chain organization of P3HT in the solid state.

In order to reduce the bandgap, sufficient long thiophene chain is essential. However, increasing of chain length will inevitably reduce the solubility of the product. Therefore, alkyl group is added to improve the solubility which is beneficial to the fabrication process [69]. Hexyl group is the balanced length to raise steric effect in the polymer packing without losing the conductivity. Tokio Yamabe *et al.* showed that the electric conductivity of polymer film will decrease with increase in the length of alkyl group [72].

As shown in Figure 3-5, the polymerization of thiophene ring will only take place at the head (2 position) or the tail (5 position). This configuration results in three possibilities of coupling: head-to-tail coupling, head-to-head coupling and tail-to-tail coupling. We can see that only head-to-tail coupling can repeat to form a uniform macromolecule. Thus, regioregularity is commonly defined as the percentage of monomers which adopt head-to-tail coupling to describe the structure homogeneity [73]. Moonhor Ree *et al.* studied the influence of regioregularity on the absorption, photoluminescence, packing of P3HT and performance of P3HT/PCBM bulk heterojunction device [74]. They demonstrated that higher regioregularity induces a closer and better molecular chain



organization. The increase of absorption and luminescence effect is attributed to stronger interchain interaction.

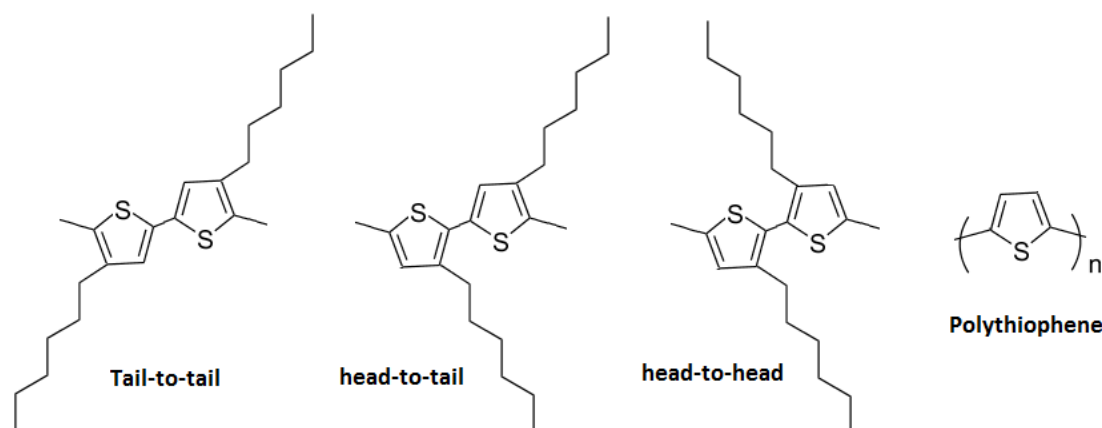


Figure 3-5 Coupling structure of 3-position alkyl substituted thiophene ring and structure of polythiophene.

Similar to inorganic semiconductor, the conductivity of P3HT is found to be thermally sensitive. The temperature dependence of d.c. conductivity of P3HT was investigated by Kirt A. Page *et al.* The results show that the d.c. conductivity varies by three orders of magnitude over the temperature range of -80°C to 70°C [75]. This implies that the variation in temperature of application environment will bring considerable deviation in the performance of solar cell fabricated with P3HT.

3.4 Electrospinning process

TiO₂ nanofibers are employed to form an infiltrated structure with P3HT by the electrospinning process. Using electrospinning to produce TiO₂ nanofibers is



extensively investigated and reported before [76-79] and it is a convenient technique to fabricate high aspect ratio fibers with nanoscale diameter. Nevertheless, the mechanism of this technique is quite complicated. It involves a number of parameters about not only the operation condition, but also the properties of solution [80,81]. As ordered structure of nanofibers can lead to higher current and efficiency [28], a rotating collector has been introduced in the electrospinning system. Such alignment enables denser deposition of nanofibers while keeping small thickness of device.

3.4.1 Process principle

Basically, a solution or melt of polymer, which serves as fiber former, including fiber precursor is prepared. The solution is pumped to flow through a thin nozzle with high electric tension and a counter electrode is placed in front of the nozzle. Because of the high electric field, induced charge will accumulate at the front of solution resulting in the deformation of solution toward the counter electrode. As the electric potential is increased, a semi-spherical shape of solution drop will be deformed to a conical shape known as Taylor cone. As the surface charge repulsion eventually exceeds the surface tension of solution, solution will be ejected from the tip of the Taylor cone [82].

When charged jets travel along the electric field lines, the solvent evaporates rapidly and is subjected to different fluid instabilities causing violent banding and stretching [83]. The electrostatic repulsion between the surface charges leads the jet to deflect laterally and form a conically shaped travelling path. D. H. Reneker *et al.* illustrated this



envelop cone as shown in Figure 3-6. At the initial of charged jet path, there exists a stable zone in which the flight path is straight. According to conductivity and viscosity of the polymer jet, jet radius and applied electric field, Rayleigh and whipping instability will grow at different rates with respect to flying distance. Whipping instability usually dominates in following zone in which the flight path of jet is chaotic and unpredictable [84]. Large stretching force caused by the instability gives rise to fibers with very thin diameters ranging from few micrometers to nanometers and with high aspect ratios.



Figure 3-6 Charged jet bending under instability [83].



3.4.2 Equipment

Figure 3-7 shows the schematic diagram of the electrospinning setup. The main part of the system is enclosed by a large transparent PMMA box. Because the process involves high electric field, PMMA box provides good isolation of the inner field from outer environment. A syringe pump is used to inject sol-gel of TiO₂ through a metallic nozzle fixed on the PMMA wall. A high voltage supply (0 – 40 kV) is connected to the hollow metallic needle to give high potential to the solution inside. Negative end is connected to ground and a planar counter electrode. The substrate is stuck on a metallic rotor, which is controlled by a motor, for fiber alignment.

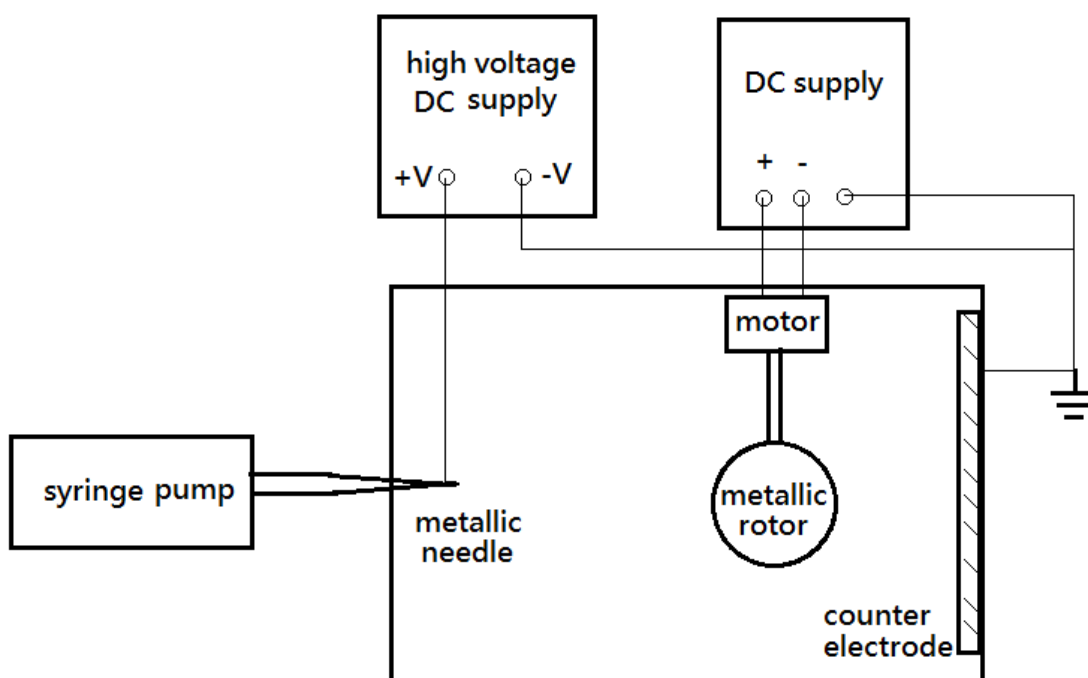


Figure 3-7 Schematic diagram of electrospinning set-up.



3.5 Fabrication of photovoltaic device

Before the fabrication process, the glass substrates are cut to 12 mm x 12 mm for convenience of processing. The patterned ITO at the center of substrates is 4mm wide and has 15 Ω /sq sheet resistance. The substrates are cleaned in an ultrasonic bath using acetone, isopropyl alcohol (IPA) and ethanol sequentially and 20 min for each step. Three minutes oxygen plasma cleaning is subsequently applied to remove organic remnant.

A TiO₂ layer is fabricated on the ITO by a sol-gel method. The sol-gel solution is prepared by adding 0.05 g acetylacetone and 0.06 g ethanolamine in 3.55 ml ethanol first. After roughly mixing, 0.34 ml titanium (IV) n-butoxide precursor is dissolved in the solution. It must be mixed by a magnetic stirrer for 1 day to ensure the uniformity of the solution. The resulting solution is clear and yellowish.

Because titanium (IV) n-butoxide is unstable and very active to moisture, acetylacetone and ethanolamine are added for stabilizing purpose and heating is also avoided. The well-mixed solution is spin-coated on the cleaned ITO at 6000 rpm for 30 s. The coating environment is filled with dried compressed air to control the moisture in air. Sintering of the coated film is performed at 500°C for 2 min in oxygen rich environment. This layer not only serves as a hole-blocking layer in device operation but also provides a rough surface to improve the adhesion of electrospun nanofibers in the next step.



To fabricate nanofibers of TiO₂ by electrospinning, a solution contained titanium (IV) tetra iso-propoxide (TTIP) and poly(vinylpyrrolidone) (PVP) is prepared. First of all, 0.2 g high-molecular-weight PVP ($M_w = 1,300,000$ g/mol) is mixed in 2.92 ml 2-methoxyethanol (EGME) and 0.9 ml IPA and stirred for 1 day. The stirring ensures completely dissolution of PVP and excludes the trapped air in the PVP powder. Then, 0.01 g acetylacetone, 0.02 g acetic acid and 0.2 g TTIP are added and stirred for 2 days because the PVP solution is very viscous. Similar to the TiO₂ film sol-gel, the solution should be clear and yellowish.

The metallic rotor is normally placed at 17-20 cm in front of the needle. After substrates with TiO₂ thin film are stuck on it, the PMMA box is closed and filled with dried compressed air. Then, the motor is turned on and a high voltage up to about 10 kV is gradually applied on the metallic needle to establish an electric field of about 40 kV/m. A syringe containing the solution is placed on a syringe pump for injection into the electric field. The feeding rate of solution is 0.1 ml/h. Each layer of nanofibers is collected for about 30 min to fully occupy the surface. The next layer is collected perpendicular to the previous one to create a porous structure. Devices with different number of layers are fabricated to illustrate the effect. Subsequently, the nanofibers are sintered at 500°C for 10 min in oxygen to remove organic compound and to activate nucleation of TiO₂.

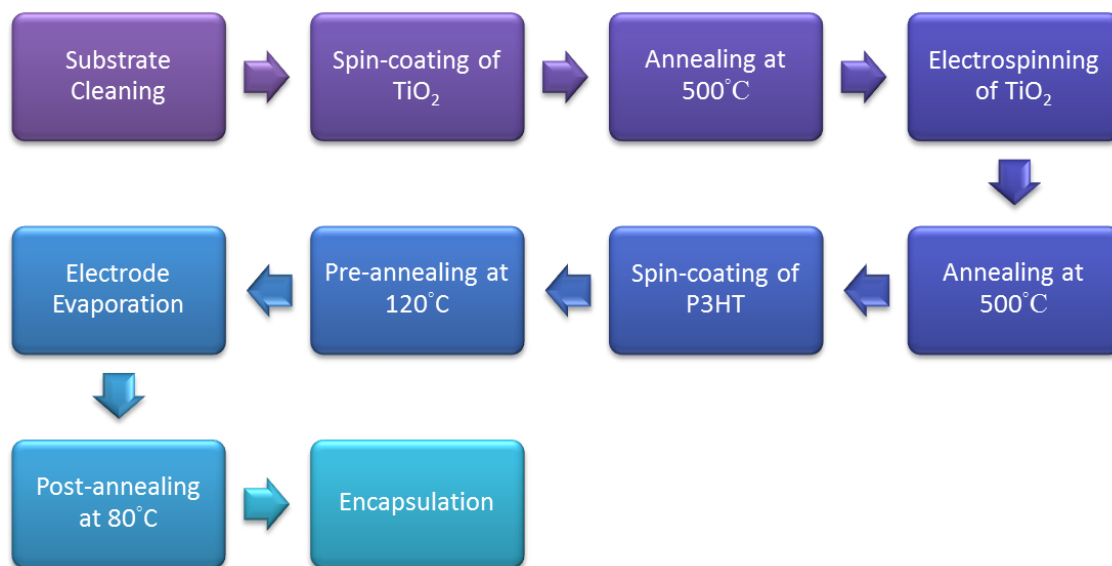


Figure 3-8 Flow chart of device fabrication.

P3HT purchased from Rieke Metals, Inc. with regioregularity 93% is dissolved and mixed in toluene at 50°C. The resulting solution is reddish brown and spin-coated on the fibrous film at 1500 rpm for 30 s. The coated samples are immediately transferred to a glove box filled with high purity nitrogen and annealed at 120°C for 20 min to reduce oxygen vacancy and crystallize the polymer. Then, the samples are taken out from the glove box. Thermal evaporation is employed to deposit Au electrode of about 80 nm on the P3HT layer through a patterned mask to define the area of the devices. Post-annealing at 80°C for 15min is carried out in the glove box to improve the contact of P3HT and electrode. Finally, devices are encapsulated by glass pieces for isolation. A complete flow chart of the device fabrication is shown in Figure 3-8.



3.6 Characterization of devices structure and performance

The TiO₂ layer thickness and roughness is measured by atomic force microscopy (AFM). The thickness of the TiO₂ layer is about 40 nm with 10 nm roughness. It can be seen that the film tends to shrink into island during the nucleation. This roughness provides a better surface for nanofiber deposition.

After the electrospinning process, the alignment of nanofibers is revealed by optical microscopy. Figure 3-9 shows the morphology of 2 layers of nanofibers before the annealing process which means the nanofibers are a composite of polymer and TiO₂ precursor. The image shows that the diameters of nanofibers are mostly below 1 μm and just occasionally thicker than 1 μm. In addition, the perpendicular alignment between two adjacent nanofiber layers is clear. By assuming the morphology will not change after the annealing of nanofibers, a porous continuous layer is expected to form in the same configuration of this state. Much thinner fibers are expected because of the removal of organic content and nucleation of TiO₂ during the annealing process.

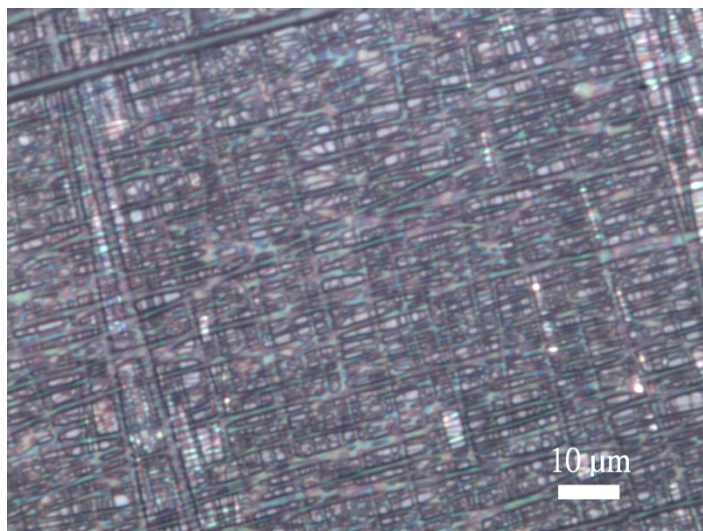


Figure 3-9 Morphology and alignment of nanofibers before annealing.

SEM is employed to reveal the nanostructure with resolution ranging from hundred to few nanometers. Figure 3-10 shows two SEM images of intercrossed nanofibers formed on the TiO₂ layer with different magnifications. High magnification image (Figure 3-10 (b)) illustrates that the nanofiber diameter is further reduced by the annealing process. The thickness of nanofibers ranges from 30 nm to 100 nm and the most popular thickness is 70 nm. However, low magnification image (Figure 3-10 (a)) shows that the alignment of nanofibers is not as good as nanofibers before annealing which are straighter and more parallel. A possible reason for this is that the nanofibers deposited on the substrate are not strongly attached to each other. Consider the weight ratio of polymer and TiO₂ precursor is 1 to 1 in the nanofibers, a large amount of gas is released by the combustion of organic part. This gaseous pressure may influence the alignment of nanofibers. Furthermore, during the nucleation of TiO₂, atomic migration inside nanofibers may cause inner stress to distort the geometry of nanofibers.

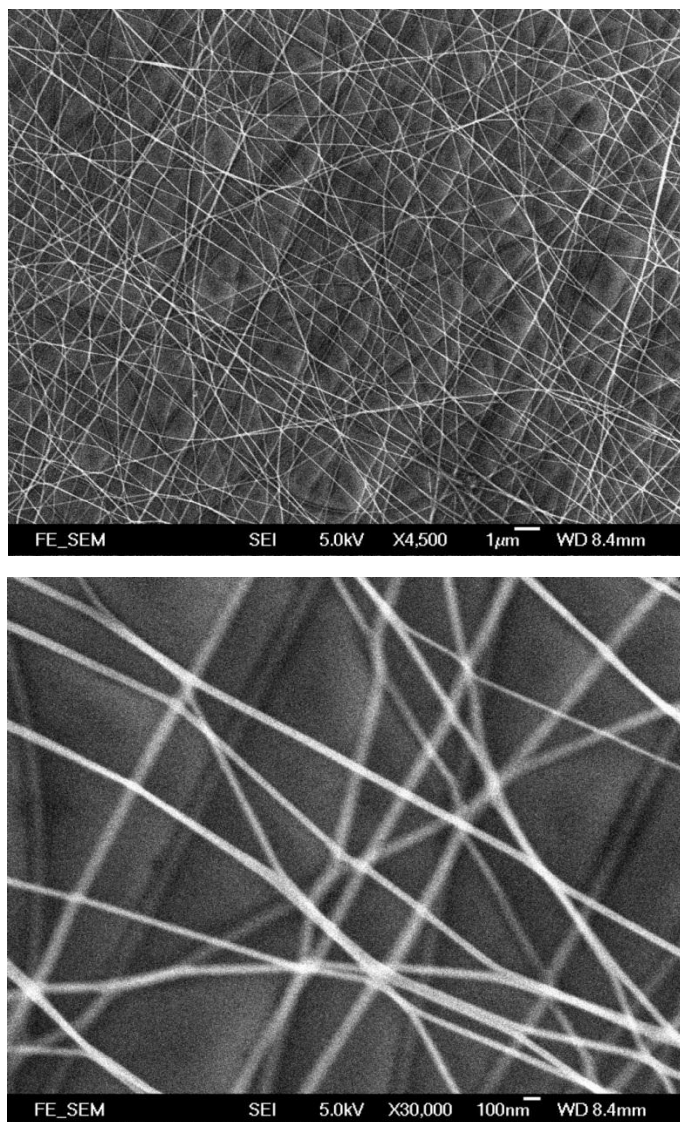


Figure 3-10 SEM images of TiO₂ nanofibers at (a) x4500 (b) x30000 magnification.

Figure 3-11 shows the morphology and diffraction pattern of a TiO₂ nanofiber under TEM. We can see that this fiber has 80 nm diameter and smooth surface. The diffraction spectrum is performed at the location marked by the circle in Figure 3-11 (a). By matching the diffraction pattern to crystal plane, the polycrystalline structure of anatase



phase of the nanofiber is confirmed. The brightest fringe corresponding to (101) plane at 25° is the strongest peak of anatase. The following two fringes are (103) and (200) planes at 37° and 48°, respectively.

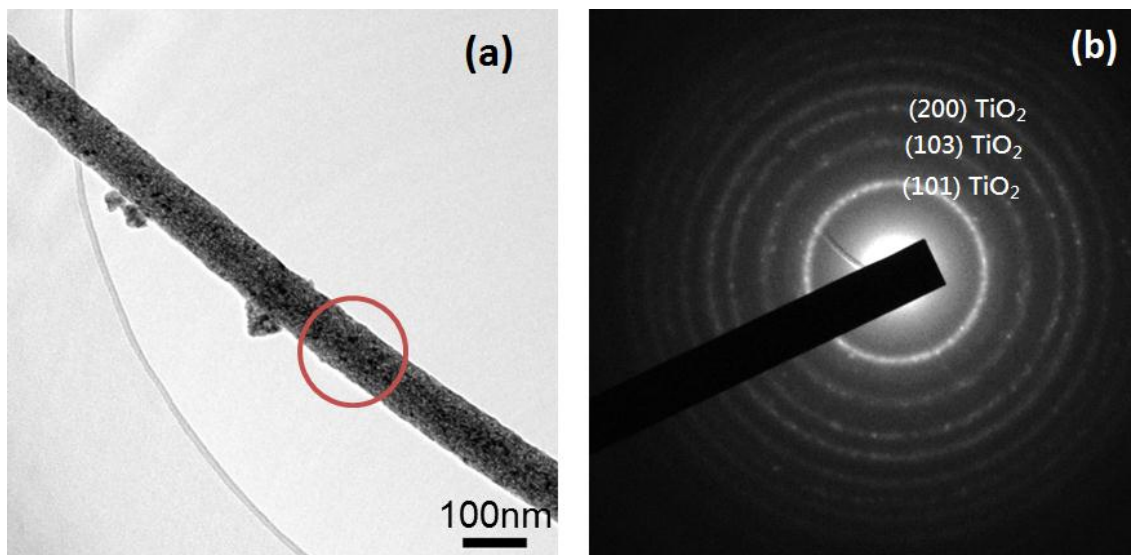


Figure 3-11 (a) Morphology (b) diffraction pattern of TiO₂ nanofiber under TEM.

Afterwards, a P3HT layer is spin-coated on the annealed TiO₂ nanofiber structure which is rough and porous. To know whether the P3HT solution can infiltrate into this structure, contact angle of the solvent on TiO₂ is a crucial parameter. If the contact angle is large, it means that the solvent cannot spread out on the TiO₂ surface so that it is difficult to bring P3HT into the TiO₂ fibrous structure in the coating process. Therefore, the contact angle of toluene on TiO₂ is measured and shown in Figure 3-12. We can see that the toluene drop spread on the TiO₂ film surface. The contact angle is around 6° to 9° so that toluene is a suitable solvent to infiltrate P3HT in TiO₂ nanofibrous film.

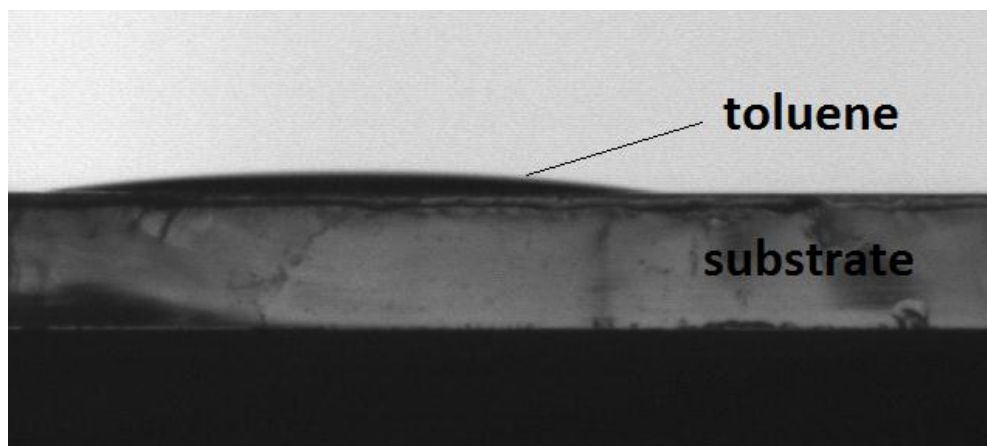


Figure 3-12 Contact angle of toluene on TiO₂ film.

The devices with different number of nanofiber layers are characterized under xenon lamp solar simulator. Figure 3-13 shows the J-V characteristics of the devices under illumination intensity of 100mW/cm² (condition AM1.5G). We can see that the current generated by the devices increases with the addition of fiber layers up to three layers. After adding the fourth layer, the J-V curve obviously gives distortion and lower current than the 3-layer device.

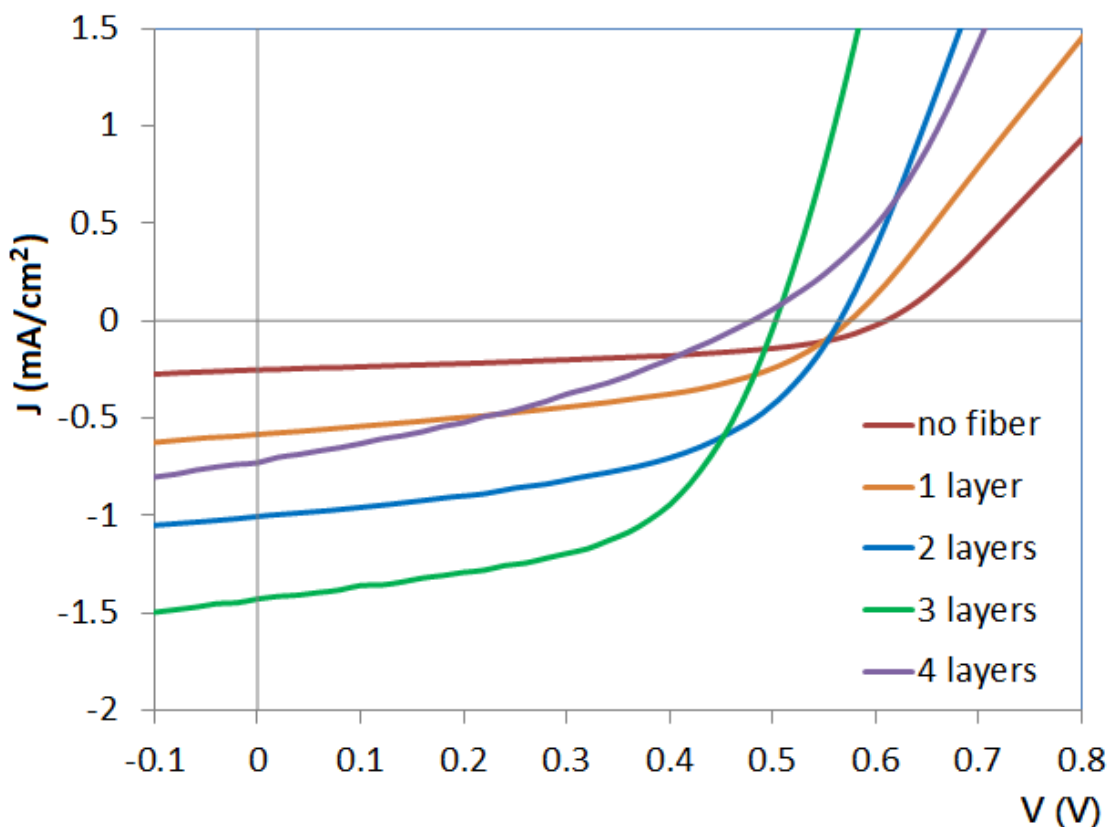


Figure 3-13 Current density – voltage curves for TiO₂/P3HT devices with different number of fiber layers.

The device without fibers gives high $V_{oc} = 0.61V$, low $J_{sc} = 0.25 \text{ mA/cm}^2$, $FF = 0.49$ and efficiency = 0.074%. Although V_{oc} is the highest among this set of devices, the short circuit current is very low. Addition of fiber layer can dramatically increase the roughness and the surface area of the TiO₂ film which can enhance exciton dissociation in the active layer. This effect is proved by the increase of generated current with number of fiber layer. The V_{oc} of devices slightly drops when the TiO₂ fiber layer becomes thicker, which is probably due to the increased series resistant of the solar cell. On the other hand, the rough surface of multilayer TiO₂ fibrous film may decrease the



shunt resistance of the devices, which is another possible reason for the decreased open circuit voltage.

The sudden drop of performance for the device with 4 fiber layers is caused by too thick an active layer of the device. This is indicated by the low FF of this device. The large slope in the low voltage region shows that electron-hole pair recombination is serious. Although more dissociation site is created in the active layer, the charge carriers cannot be collected by electrode before recombination. The limited diffusion distance of charge carriers restricts the device thickness. Another feature of the J-V curves is that the slope at high voltage region firstly increases when the fibrous layer is thin and then decreases when the fourth layer is added. We can see that the thin fibrous layer reduces the series resistance and helps the carrier transportation of the devices.

All the important parameters of this measure are listed in Table 3-2 below. The area of each device is different, because the device area is defined by the overlapping area of two electrodes (ITO and Au). It is characterized under the optical microscope. The most efficient device is given by 3 layers of nanofibers in the active layer. This device demonstrates an efficiency of 0.39% which is about five-fold increase of the device without fiber layer. This should be attributed to the great increase in current density (1.43mA/cm²) while keeping moderate value of FF (0.54) and Voc (0.5V).



Table 3-2 Summary of performance parameters of TiO₂/P3HT devices with different number of nanofiber layers.

	Area (cm ²)	Voc (V)	Jsc (mA/cm ²)	FF	η (%)
4 fiber layers	0.017	0.48	-0.73	0.34	0.12
3 fiber layers	0.019	0.50	-1.43	0.54	0.39
2 fiber layers	0.014	0.56	-1.01	0.49	0.28
1 fiber layer	0.017	0.57	-0.58	0.45	0.15
No fiber	0.012	0.61	-0.25	0.49	0.074

3.7 Discussion

In the construction of TiO₂ nanofiber structure, the electrospinning process is rather random that it cannot control the exact position of fibers on the substrate. Although the same fiber alignment condition is held every time, the difference in configuration will produce certain deviation in each device. Only the total amount and main orientation of fibers can be controlled by deposition time and rotation. Variation of local fiber density and overlapping of fiber in the same orientation are inevitably found in each time. Indeed, much research effort has been made to align nanofibers from electrospinning [85-87]. W. Hutmacher *et al.* recently developed a direct writing method of melt electrospinning by which precise position and alignment of fibers can be controlled [88], because the nanofibers are collected in the stable zone very close to the nozzle. However, polymer solution requires distance for evaporation so that instabilities always influence the morphology of fibers. To minimize the deviation from fiber configuration, samples of the same set will be placed on the rotor together to deposit the nanofibers in



a single process.

Furthermore, devices involving micro- or nano-structures will encounter a problem that organic material cannot completely infiltrate into the structure. In the spin-coating process of P3HT on TiO₂ fibrous structure, some trial devices also have the same problem. Those devices generally show low FF or low current density. The incomplete infiltration of P3HT will leave pores and form trap states in the active layer. Excitons near pores are difficult to dissociate and lead to recombination. In macroscopic view, the series resistance of device will increase because of the presence of pores in the composite layer.

Several reasons will lead to incomplete infiltration of P3HT. The solution of P3HT in toluene is viscous and opaque at room temperature so that, before coating, it must be pre-heated to about 50°C to become fluidic, reddish and transparent. Also, substrate at similar temperature is preferred for the coating process. Only a small droplet of P3HT solution is used in coating. If the substrate is cold, the droplet will instantly be cooled down after being in contact with the substrate. After a solution drop is deposited on the substrate, it is necessary to wait for a few seconds. Because there are many spaces inside the TiO₂ nanofiber structure, the solution may not immediately reach all the positions. When more layers are constructed on the substrate, more time is needed to ensure complete infiltration. However, toluene is a volatile solvent. If waiting for too long, the P3HT layer will be very thick and uneven. To accelerate the infiltration of P3HT solution, toluene is sometimes spin-coated on nanofiber structure first. Pure



toluene is much easier to go into the structure. In addition, this can avoid trapping of air in the P3HT solution.



Chapter 4 Interfacial Modification

4.1 Introduction

In order to enhance the efficiency of the hybrid solar cells, interfacial modification is a feasible approach that can facilitate exciton dissociation at the inorganic–organic heterojunction. Different from traditional solar cells, excitonic solar cells rely on the interfacial energetics of the acceptor-donor heterojunction to separate excitons. To change the interfacial energetics, interfacial modifier can be attached to the surface before the formation of junction. Semiconductor quantum dot [89] and thin layer [90], organic dye [91,3] and small dipole molecule [92,93] can serve as interfacial modifier to affect the interaction of materials. Interfacial modifier can block charge recombination or facilitate the transport of charge carriers. Some dipole molecules attached to surface with specific orientation can induce shifting of energy band at the material surface [92]. Owing to the semiconductor nature, interfacial modifier also absorbs part of the sun light and it is often chosen to be complementary to the absorption spectrum of the junction materials.

A range of semiconductors can be used for interfacial modification, for instance, CdSe [89,94], PbS [95], Se [96], In₂S₃ [97] and Cu_{2-x}S [98]. Because junction interface becomes bulky in most investigation, thin layers of those semiconductors are commonly fabricated through solution medium such as chemical reaction, chemical bath deposition, successive ionic layer adsorption and reaction, electrochemical deposition or



other nanotechnology. In the work presented below, cadmium sulfide (CdS) is chosen to modify the optimized device obtained from Chapter 3. Figure 4-1 (a) shows the three-dimensional diagram of the target device. CdS layer is deposited on the TiO₂ fibrous layer before P3HT infiltration.

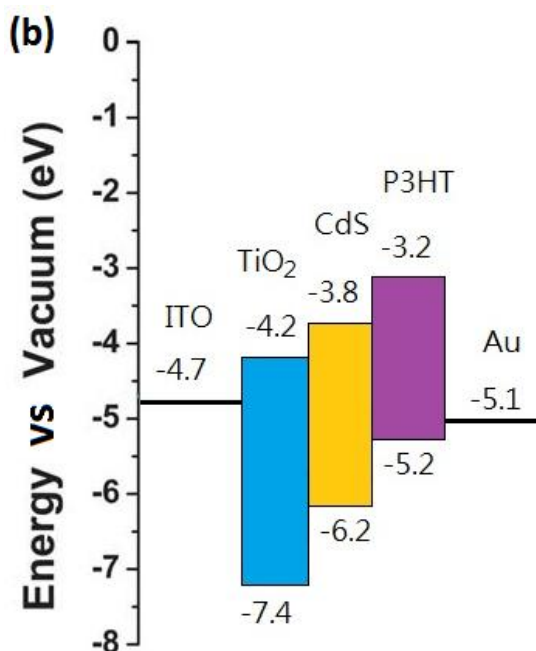
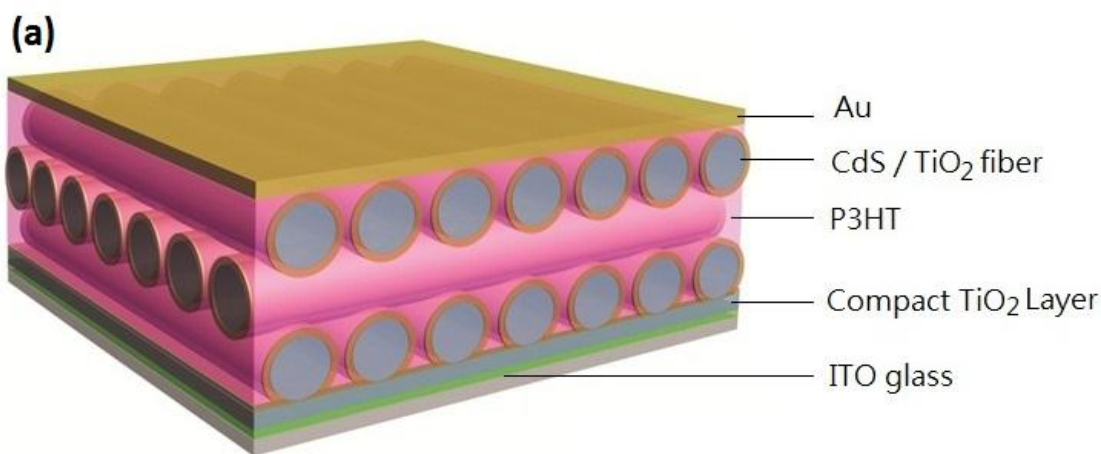


Figure 4-1 (a) Three-dimensional structure and (b) band structure of modified device.



Consider the band structure of CdS shown in Figure 4-1(b). This band alignment allows the excitons contributed from the different parts to dissociate at the CdS/P3HT or TiO₂/CdS interface. All free electrons and holes are directed to the ITO side and Au side, respectively. Moving in the reverse direction is forbidden by the energy barrier. From previous reports [99,100], the CdS layer can significantly increase the Voc of similar hybrid junction by passivating the surface state to reduce recombination and charge trapping. Also, CdS provides extra light absorption to increase Jsc in the device.

4.2 Properties of cadmium sulfide (CdS)

CdS is a II-VI semiconductor having two polymorphs, greenockite and hawleyite. Figure 4-2 shows the atomic configuration of these two phases. Greenockite appears as shade yellow and orange while hawleyite as bright yellow. The appearance depends on the synthesis condition and both phases are stable at room temperature. Greenockite has a hexagonal structure with lattice parameters $a = 4.136 \text{ \AA}$ and $c = 6.713 \text{ \AA}$ [101] while hawleyite is cubic with lattice parameter $a = 5.818 \text{ \AA}$ [102].

A number of studies are reported about the structural, optical and electrical properties of CdS from different synthesis methods because of its diversity [103-107]. Among different growth methods of CdS, electrochemical deposition and chemical bath deposition are available for bulky substrate. Chemists have demonstrated the deposition of CdS by several ligands such as ammonia [108], triethanolamine [109],



ethylenediamine [110], nitrilotriacetic acid [111], cirtatocomplex [112] and tartaric acid [113]. Because CdS is insoluble in water, when aqueous solution of those Cd^{2+} salts react with sulfide carrying molecules, homogeneous precipitation occurs slowly.

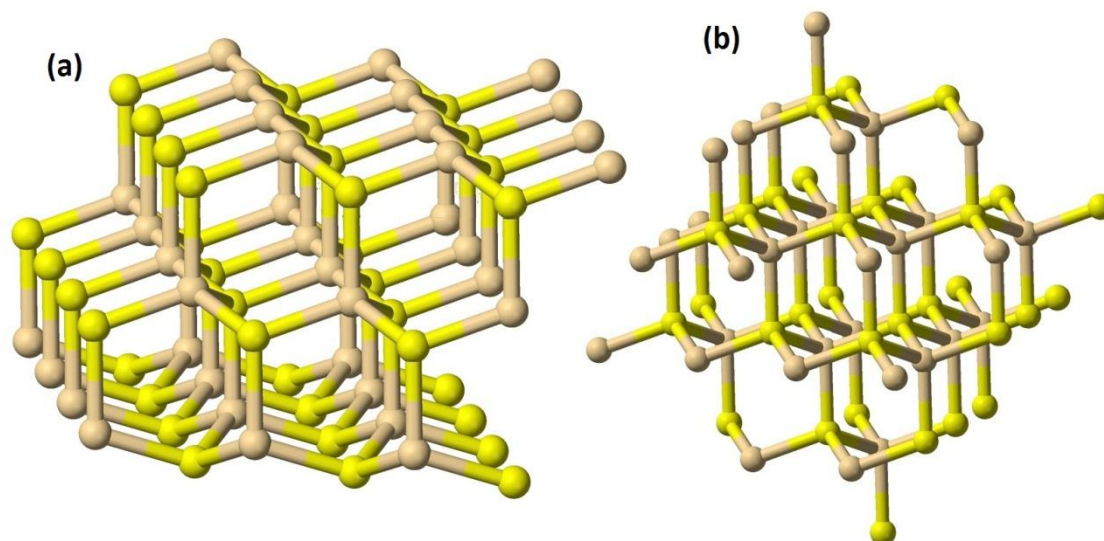


Figure 4-2 Structure of (a) greenockite [114] and (b) hawleyite [115].

Due to its sharp yellowish color, CdS is mainly used as pigment. In the development of optoelectronic devices, its direct band gap of 2.4 – 2.5 eV, equivalent to about 500 nm, has drawn considerable research interest for applications such as semiconductor laser and light emitting diode [103]. In addition, its conductivity is found to be in the order of $10^{-8} (\Omega\text{cm})^{-1}$ in dark and about $1 (\Omega\text{cm})^{-1}$ under illumination at room temperature [112]. Such photoconductivity makes it available for photoresistor and photodetector applications.

In spite of the usefulness of CdS, Cd^{2+} salts are generally considered to be toxic and



hazardous to environment. According to materials safety data sheet from American National Standards Institute, CdS is carcinogenic and damages kidneys and lungs upon long term exposure. It will react with acid to form toxic hydrogen sulfide [116].

4.3 Electrochemical deposition

Electrochemical deposition is a surface treatment commonly employed to deposit thin film on conducting substrate from chemical bath. The densification takes place at the solution-solid interface so that it is possible to deposit dense layer on the porous electrode. Since this method is a facile, low cost and low-temperature technique and the deposited composition can also be well controlled, it has shown much importance in the synthesis of different materials. Zinc oxide [117,118], copper oxide [119], TiO₂ [120] and nickel oxide [121] are the most widely studied semiconductors grown from this method. I. Zhitomirsky contributed many work in the growth of organoceramic films [122] and polymer films [123]. Furthermore, versatile morphologies of different materials have also been fabricated, such as single crystal [124], mesoporous metal film [125] and “3D structure” [126] etc.

4.3.1 Theory of electrochemical deposition

When an electrode is immersed in an electrolyte, equilibrium potential is established at their interface. This equilibrium will be broken, if external current is applied to shift the potential across the interface. This shifting is called overpotential, η . The overpotential activates the overall electrode reaction which includes charge transfer, diffusion,



chemical reaction and crystallization. Following the electric field established between two electrodes, cations or positive molecules move towards the cathode and release their charges by a reduction reaction:



where Ox is the oxidized form, Re the reduced form, e the electron and z is number of electrons transferred across the electrolyte-electrode interface. The time, t, derivative of the transferred charge, Q, is closely related to current density, J:

$$J = \frac{dQ}{dt} = zF \frac{dm}{dt}$$

where F is the Faraday's constant giving charges carried by one mole of electrons and m is the number of transferring event in mole per unit area. This equation has the same meaning of the Faraday's first law of electrolysis which states that the total amount of chemical change at an electrode is directly proportional to the quantity of electrical charges transferred to that electrode. We can see that $\frac{dm}{dt}$ represents the rate of reaction in mole. The rate constant, k is defined as

$$\frac{dm}{dt} = k [Ox]$$

where [Ox] represents the concentration of Ox. Based on the above relation, pioneers finally formulate the relation between current and overpotential by introducing the transfer coefficient α and the well-known Arrhenius equation:

$$k = A \exp\left(-\frac{\Delta G}{RT}\right)$$

where A is a constant, ΔG the activation energy of reaction, R the gas constant and T is absolute temperature. The resulting relation is:



$$J = J_0 \left[\exp\left(\frac{(1 - \alpha)uzF}{RT}\right) - \exp\left(-\frac{\alpha uzF}{RT}\right) \right]$$

The equation is named as Butler-Volmer equation. J_0 is called the exchange current density which is an important parameter to define the kinetics of the electrochemical cell.

4.3.2 Equipment

In the deposition system, a three-electrode configuration in a single-compartment cell is employed. A schematic diagram is shown in Figure 4-3. A platinum plate is used as the counter electrode because of its chemical stability. The reference electrode is a silver/silver chloride electrode in saturated potassium chloride solution. ITO on the sample acts as the cathode. It is placed in parallel to the platinum plate in order to get a uniform deposition.

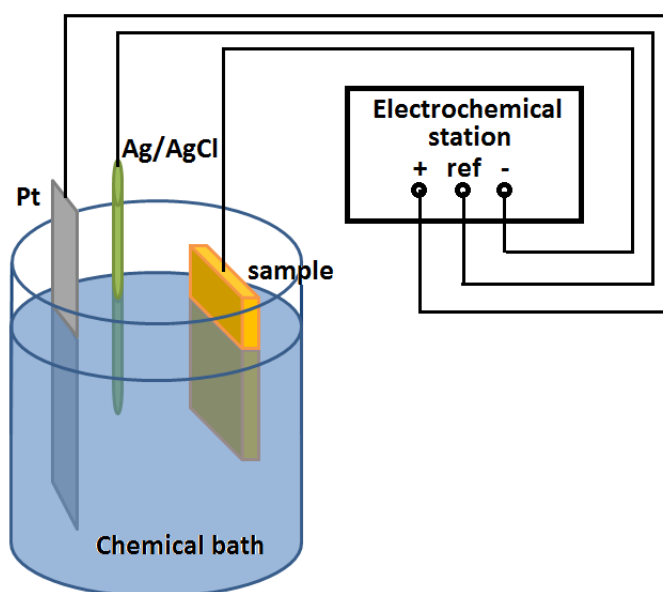
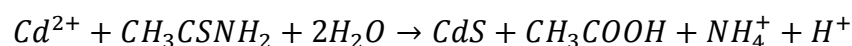


Figure 4-3 Schematic diagram of set-up of electrochemical deposition.



4.3.3 Deposition process of CdS

An aqueous bath containing Cd^{2+} and sulfide carried molecule is prepared by reacting the same volume of 0.1M cadmium nitrate ($\text{Cd}(\text{NO}_3)_2$) solution and 0.1M thioacetamide ($\text{C}_2\text{H}_5\text{NS}$) solution. The mixture is initially clear and CdS nanoparticles formed in the solution slowly according to the following equation [127]:



After the fabrication of TiO_2 nanostructure on ITO electrode, the ITO electrode is connected to the negative end of the electrochemical station. According to the reduction potential of Cd^{2+} , a voltage of -0.7 V is applied to the ITO electrode to activate the reaction [128]. In order to obtain uniform deposition on the fibrous layer, this threshold voltage is kept constant and results in a small negative current. Such current decreases slowly and saturates in the order of $\sim 10^{-5}\text{A}$ within ten minutes. When the deposition is carried out on the TiO_2 thin film without fibrous structure, the current is smaller than the previous process by an order of magnitude. This indicates that the connection with nanofibers increases the available area for reduction. The whole process is performed under room temperature. The deposition amounts of CdS are controlled by the time of the treatment. Since precipitation of CdS particles occurs continuously in the bath, the samples after deposition are rinsed for several times by deionized water in order to remove any physisorbed particle.



4.4 Characterization of modified surface and fibers

To characterize the morphology, thickness, absorption property and phase of the deposit, SEM, TEM and UV-vis absorption spectroscopy are employed. In order to determine the thickness of the deposit with respect to the deposition time, the process is carried out on three TiO₂ films for different time. Figure 4-4 shows the SEM images of the cross section of the samples in the same scale.

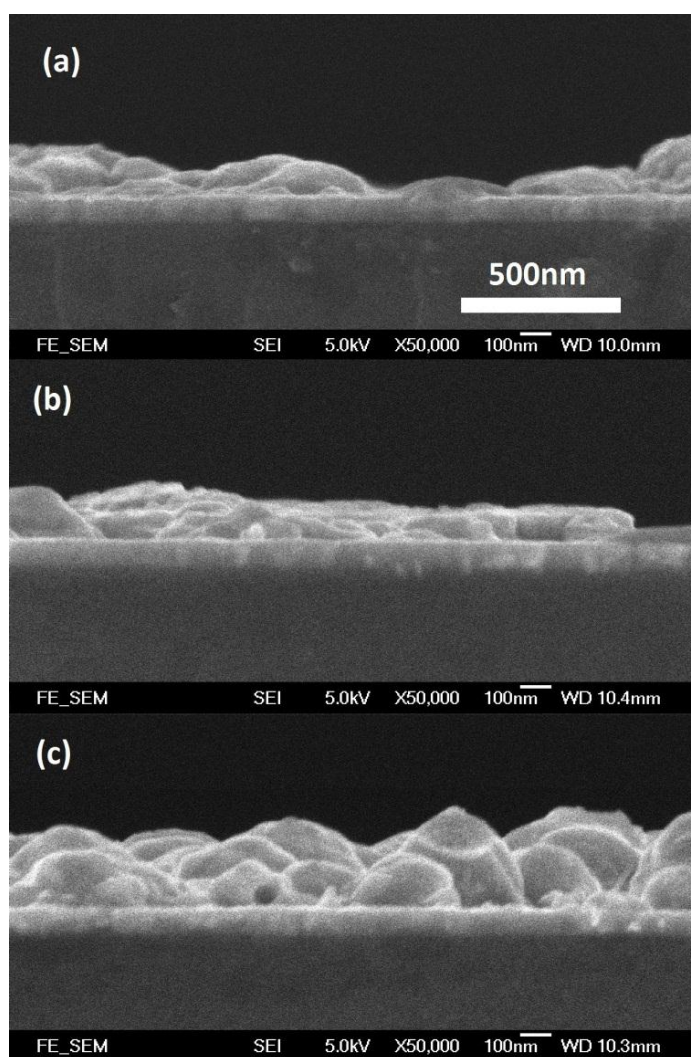


Figure 4-4 CdS grown on flat TiO₂ by a (a) 1 h, (b) 2 h and (c) 3 h deposition process.



We can clearly see the TiO₂ film with sharp boundary and the deposit grown on it. For 1-hour deposition, the growth of CdS is not quite even and cannot fully cover the surface of TiO₂. After 2-hour deposition, the CdS layer becomes more even with an average thickness of about 100 nm. For longer time deposition, a very thick (>150 nm) and rough CdS layer is observed. It seems that CdS tends to cover the surface first rather than stack up in its growth.

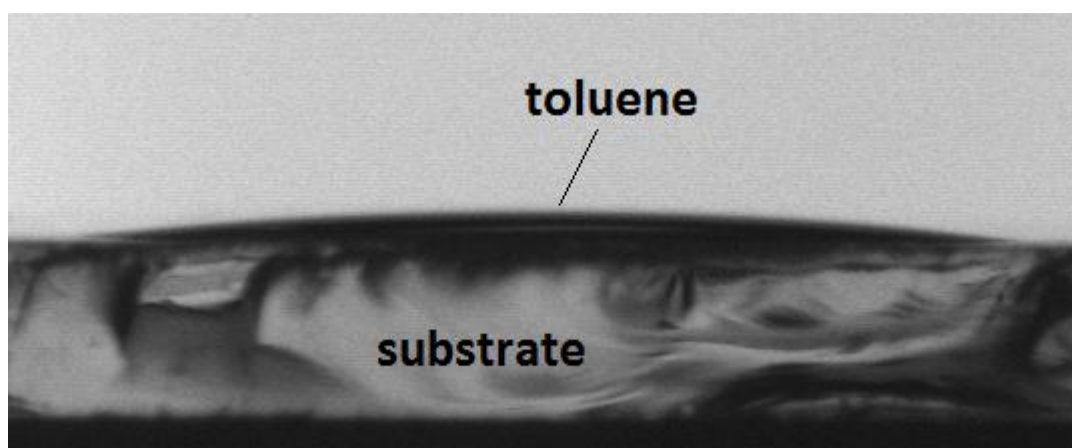


Figure 4-5 Contact angle of toluene on CdS deposition.

Subsequently, the contact angle of toluene on the CdS deposition is measured and found to be around 9° to 11°. Toluene can therefore be the solvent to coat P3HT on it.

Afterwards, CdS layer is deposited on substrates with TiO₂ nanostructure. To get reasonable amounts of CdS on nanofibers, 2-hour deposition is applied to the substrate with 3 layers of nanofibers. Figure 4-6 shows the top view of nanofiber structure after deposition of CdS. The images reveal that nanofibers are remained on the substrate with



numerous nanoparticles uniformly attached to the surface and nanofibers. The diameters of the nanofibers after deposition range from 70 nm to 180 nm.

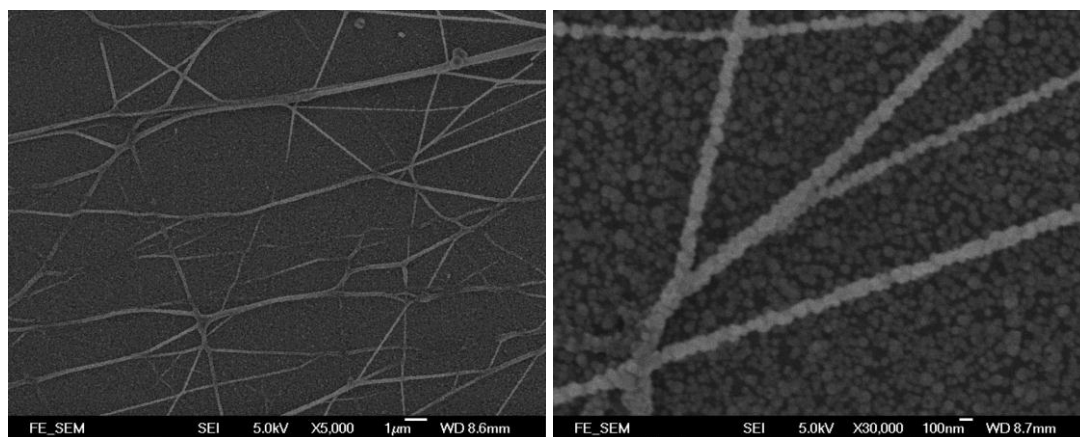


Figure 4-6 SEM images of TiO₂ nanofibers with CdS deposition.

To obtain further information of crystallinity and phase about the deposited particles, an individual nanofiber is inspected by TEM. The morphology of deposited CdS is shown in Figure 4-7 (a). There are many CdS nanoparticles grown on the TiO₂ nanofiber and their diameters range from 20 nm to 80 nm. The total fiber diameter is about 180 nm. Figure 4-7 (b) shows the high resolution image of an attached particle. The particle is polycrystalline with grain size about 5 nm to 30 nm. The distance between crystal planes is measured to be 3.19 Å.

Figure 4-7 (c) is the electron diffraction pattern performed at the location marked by the circle in Figure 4-7 (a). Because TiO₂ and CdS are both present in this location, we can find the diffraction pattern of these two materials. The phase of CdS is confirmed to be



hexagonal greenockite by eliminating the TiO_2 patterns. The most obvious evidence is the third ring which comes from the (110) plane of CdS solely. The brightest diffraction pattern consists of three rings from (100) of CdS, (101) of TiO_2 and (101) of CdS because of their similar interplane distances and high intensity. The diffraction of (102) and (103) of CdS overlap those of (103) and (200) of TiO_2 to form the second and fourth rings. And, the interplane distance found from Figure 4-7 (b) corresponds to the (101) plane of this phase.

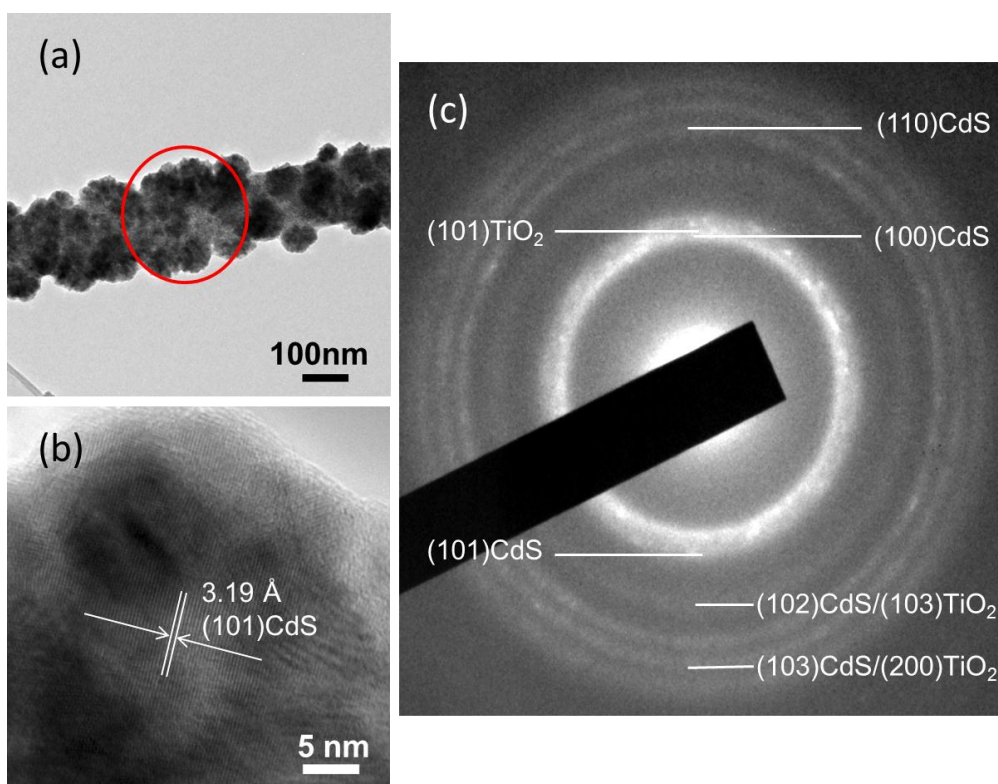


Figure 4-7 (a) Morphology, (b) atomic configuration and (c) diffraction pattern of a CdS-coated nanofiber.



The absorption characteristics of the synthesized CdS were measured by UV-vis absorption spectroscopy. To compare the absorption of TiO₂, CdS and P3HT, two TiO₂ thin films with and without CdS deposition and P3HT thin film about 50 nm thick were prepared on the transparent substrate. Figure 4-8 shows the measured results in 300 nm to 800 nm. We see that the TiO₂ thin film is fully transparent in the visible light range and gives a strong absorption for wavelengths shorter than 370 nm. The deposition of CdS largely enhances the absorption in the green to ultra-violet range. As a result of the CdS layer, a sharp increase of absorption is observed at 510 nm which corresponds to the bandgap of 2.4eV.

The absorption of P3HT shows two peaks at 516 nm and 550 nm and a shoulder at 600 nm. According to the results from Peter J. Brown *et al.* [129], the peak at 516 nm is related to the intrachain $\pi - \pi^*$ transition coupled with one phonon mode. And, the peak at 550 nm corresponds to the $\pi - \pi^*$ transition solely. The shoulder at 600 nm is contributed by interchain interaction and its position is independent of ordering. The P3HT film gives weak absorption for wavelengths shorter than 450 nm so that CdS is a suitable complementary absorber.

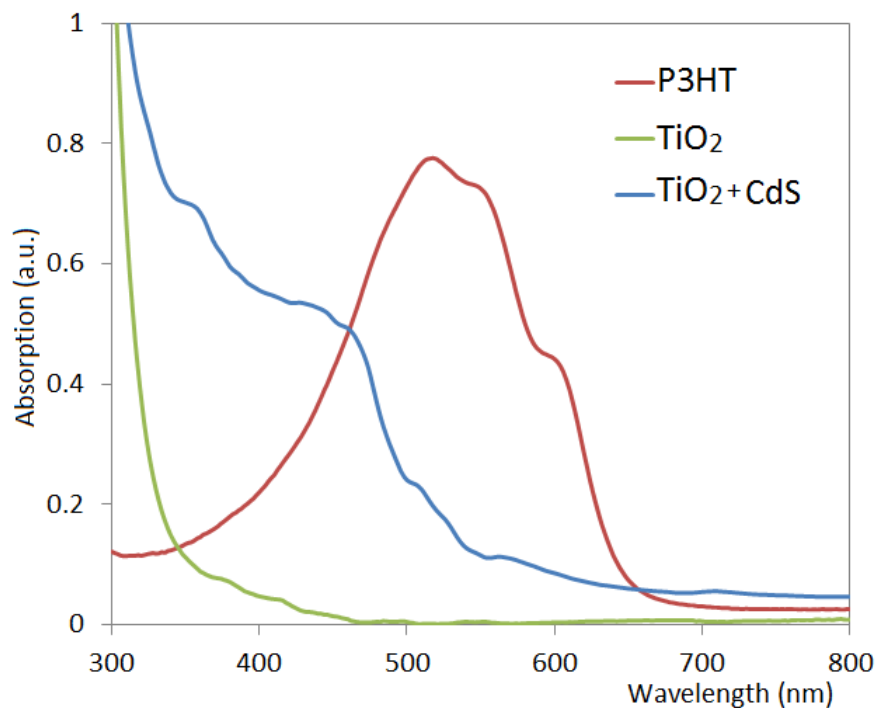


Figure 4-8 Absorption spectra of constitutive materials.

4.5 Characterization of the modified devices

Devices with CdS interlayer modification were fabricated and characterized by a solar simulator. All the fabrication conditions remained the same as mentioned in previous chapter. Initially, devices without nanostructure were modified to illustrate the effect of modification. Three deposition time were employed and compared. Figure 4-9 shows the J-V characteristics of the devices with different amounts of CdS deposition together with those of the device without deposition. All the devices were fabricated in the same set of the process. The illumination intensity was $100\text{mW}/\text{cm}^2$ by AM1.5G filter.

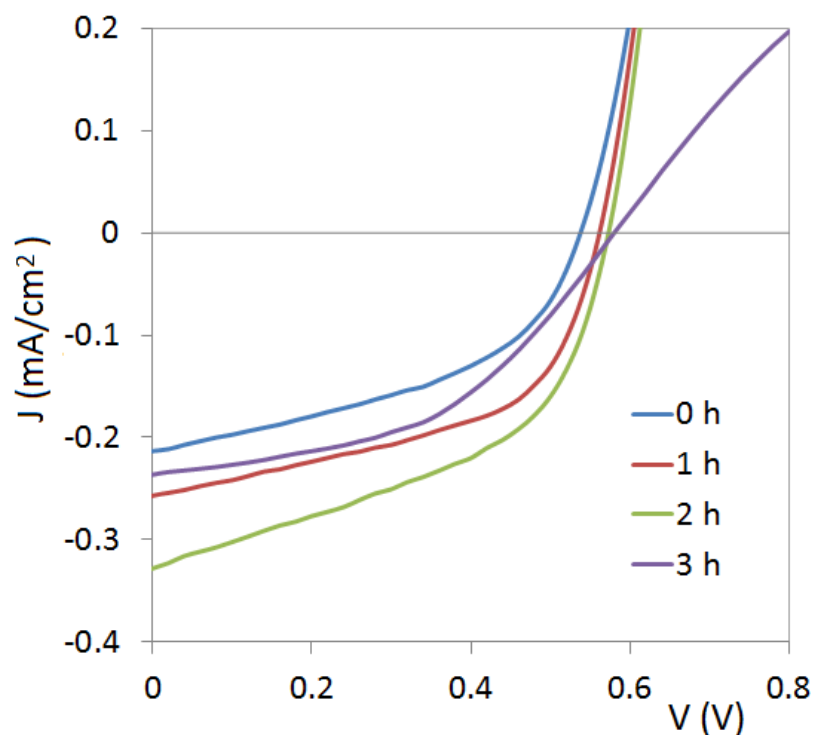


Figure 4-9 J-V characteristics of flat devices with different deposition time.

Obviously, the device with 2-hour deposition gives the highest photo-current conversion efficiency (0.099%) and J_{sc} (0.33 mA/cm^2). The V_{oc} of devices exhibit a monotonic increase with longer deposition time while the J_{sc} increases at the beginning and decreases in the sample with 3-hour deposition. The slight increase in V_{oc} may be attributed to more effective exciton dissociation by involving the CdS layer. The FF is also higher after the deposition except for the 3-hour sample. It is probably because the recombination of electron hole pair is suppressed.

Electrons in TiO_2 and holes in P3HT are blocked by the CdS from the electric field extraction. The absorption of CdS also causes more exciton generation in the device so



that the current is increased. The drop of current of the device with long time deposition should result from a too thick active layer. We notice the distortion of J-V curve in the high voltage region which indicates that a high series resistance is present in the device. Table 4-1 lists the important characteristic parameters of the devices. The improvement of efficiency is about double that of the device without CdS deposition.

Table 4-1 Summary of performance parameters of the modified flat devices.

	Voc (V)	Jsc (mA/cm ²)	FF	η (%)
0 h	0.54	-0.21	0.46	0.052
1 h	0.56	-0.26	0.52	0.075
2 h	0.57	-0.33	0.53	0.099
3 h	0.58	-0.24	0.46	0.064

To verify the origin of the improvement, the quantum efficiencies of 0 h and 2 h devices were measured with respect to monochromatic light range from 300 nm to 800 nm which is the major absorption range as illustrated by the absorption spectra. Figure 4-10 gives the EQE results of the devices. The blue curve is measured from the device without modification. We can see that the highest efficiency is found at about 490 nm to 600 nm which is strongly absorbed by P3HT. The peak at 516 nm and shoulder at 600 nm is matched to the absorption spectrum of P3HT. Furthermore, there is a small peak present at about 350 nm. It should be contributed by the absorption of TiO₂ in this region.

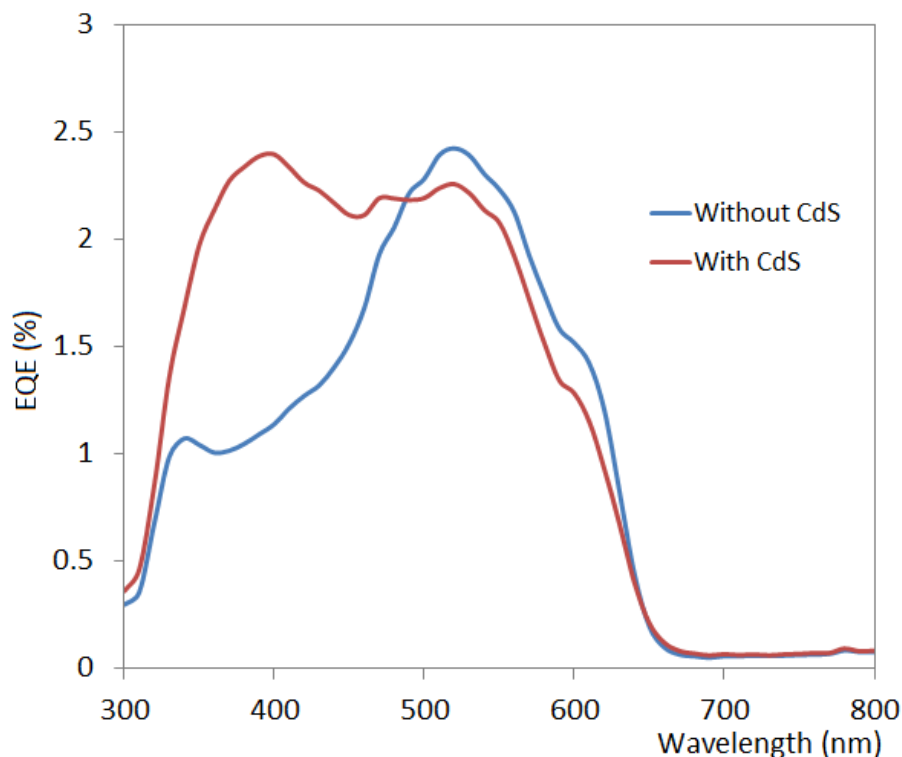


Figure 4-10 Comparison of EQE of the flat devices with and without CdS deposition.

The red curve in the figure is measured from the device with 2-hour deposition. A higher EQE is found in the short wavelength region and one more peak is present at 400 nm. The higher J_{sc} is explained by the fact that more excitons and charge carriers are harvested in green to violet range resulting from the absorption of CdS. However, a slight decrease in the P3HT absorption range is observed. It indicates that some charge carriers cannot be collected because of the presence of CdS. It may be due to the limited charge carrier diffusion length.



The next step is to characterize the effect of CdS deposition on the fibrous device. The measured J-V curves are shown in Figure 4-11. The resulting changes by deposition are similar to the device without nanofibers. The Voc also increases with the increase in deposition time and the highest current density is found in the 2-hour device. The increase of Voc is more significant this time. Comparing the original device and the 2-hour device, the Voc only increases by 30 mV in the previous analysis while it increases by 70 mV in this time. It is probably because larger interface and more CdS are present in the device. Current also drops in the last device and now it suffers more drastic decrease resulting in the current even lower than that of original device. This can be accounted for by the same reason of limited diffusion length.

On the other hand, the FF shows different change with respect to deposition time. A small decrease is seen from the modification. The highest FF obtained by modification in previous analysis is only 0.53 while the fibrous device without modification already gives 0.55. The deposition cannot boost the FF to higher values. Possible reason is that the fibrous nanostructure with larger interface already reduces the recombination by enhancing the charge carrier injection so that the CdS layer may not contribute further in the same manner.

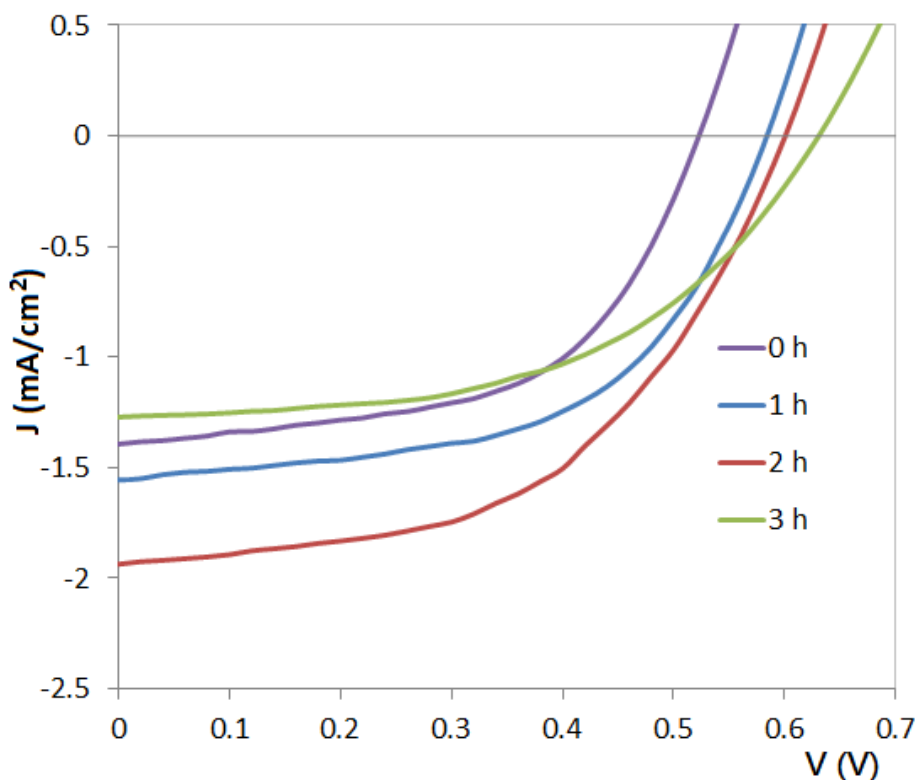


Figure 4-11 J-V characteristics of the fibrous devices with different CdS deposition time.

To summarize this analysis, Table 4-2 shows important parameters of the J-V curves. The optimum deposition time is about 2 hours which increases the efficiency from 0.41 to 0.6. As the FFs of devices are similar, the higher efficiency is attributed to the larger open-circuit voltage and short-circuit current. Nevertheless, the efficiency in this case does not increase as much as the flat device. The possible reason is that many nanofibers are dropped out in the deposition process leading to reduction of interfacial area. This can be revealed from the increasing ratio of current. The J_{sc} value increases by a factor of 1.57 after deposition in previous analysis, while it only increases by 1.38



this time. Also, the FF change contributes to this outcome slightly.

Table 4-2 Summary of performance parameters of the modified fibrous devices.

	Voc (V)	Jsc (mA/cm ²)	FF	η (%)
0 h	0.53	-1.39	0.55	0.41
1 h	0.58	-1.56	0.55	0.50
2 h	0.60	-1.93	0.52	0.60
3 h	0.61	-1.27	0.53	0.42

Afterwards, EQE of these four devices are measured and the results are plotted in Figure 4-12. By carefully comparing the EQE curves shown in Figure 4-12 and Figure 4-10, we can find that they not only differ from their magnitude, but also in their shapes. The top of EQE curves is not flat, but there are two well defined peaks belonging to P3HT and CdS. Although we find suppression of the P3HT peak previously, the modification also enhances the contribution from P3HT this time. A possible reason is that the rough interface in the device allows more charge carrier injection before recombination.

By observing the evolution of the curves, we can see that more CdS sample gives broader peak and flatter region from 400 nm to 460 nm. According to the absorption spectrum of CdS, the EQE curve shape becomes closer to the absorption curve of CdS and dominant in long time deposition. The emerged narrow peak at 400 nm resulted from the involvement of thin CdS layer was also reported by Spoerke *et al.* [99]. As the



CdS layer becomes thicker, the shrink of P3HT absorption peak is observed. The contribution of P3HT is lower than CdS in the last device. In addition, the peak position of P3HT suffers from a little blue shift from 510 nm of the original device to 500 nm in the last device. It may indicate that the thick CdS layer leads to low P3HT ordering. Finally, the high energy region corresponding to the absorption of TiO₂ shows weak dependence on the deposition time.

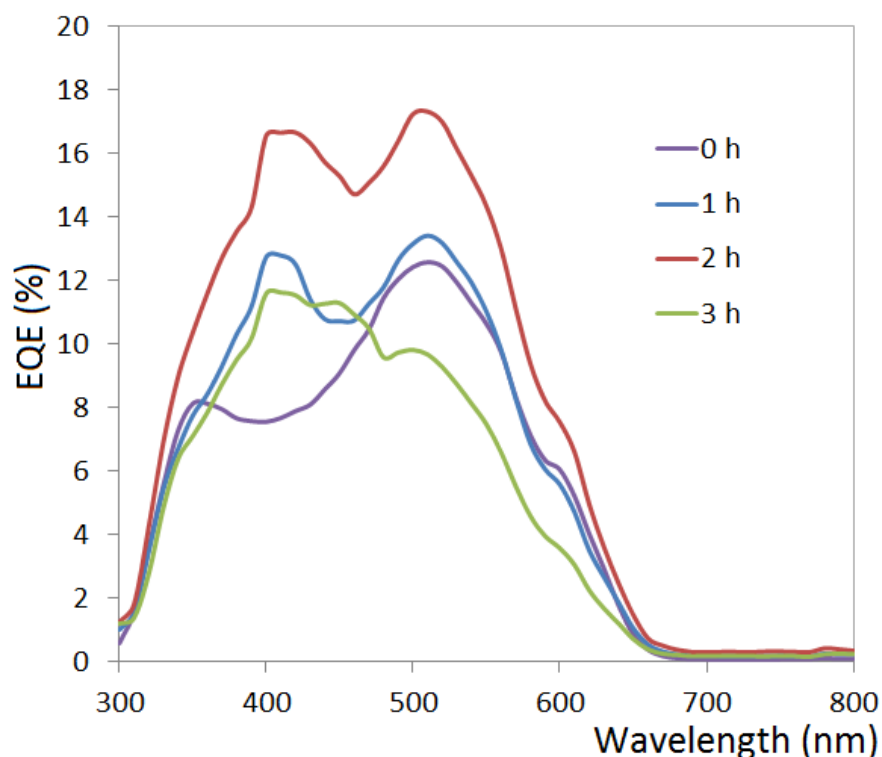


Figure 4-12 EQE of the fibrous devices with different deposition time.

4.6 Discussion

In the above analysis, the optimal modification time is 2 hours. According to the presented image of cross section of CdS deposition (Figure 4-4), the thickness is about



100 nm. However, the top view SEM (Figure 4-6) and TEM (Figure 4-7) images reveal the deposition composed of many nanoparticles. It is believed that the judgment upon cross section may be influenced by some particular particles in the background so that the effective thickness of deposition is believed to be less than 100 nm.

Fabrication processes such as annealing, electrospinning and Au evaporation are performed to all devices in the same set to reduce the deviation of outcome. However, the electrochemical deposition process should be performed one by one in the same electrolyte bulk for better repeatability. The presence of more than one substrate inevitably leads to non-uniform coating of CdS between the substrates. It depends on the position of substrates. Also, current passing through each substrate is ambiguous. Therefore, deposition is performed sequentially on each substrate. The position of substrate should also be retained at the same position in each time.

Furthermore, as revealed by the EQE results, the effect of deposition indeed varies with the morphology of interface. In case of 2-hour deposition, the contribution of P3HT is suppressed in the flat interface device, while improvement is found in the nanostructure device. The later one has nanostructure to provide more charge dissociation site to boost the electron injection to n-type transporter so that the difference may come from the injection property of the junction. It is reasonable to conclude that the optimum amount of modification varies with the morphology and material properties. The coincidence of optimum deposition time in the above analysis is probably because the sampling interval (1 hour) is a bit wide.



Chapter 5 Graphene Electrode Replacement

5.1 Introduction

Recently, graphene has attracted intensive research activities in studying its physical properties and potential applications. Beginning with a free-standing atomically thin carbon film accidentally obtained by Novoselov, K. S. *et al.* [130] few years ago, many research groups follow his work on this monocrystalline graphitic film. It is a groundbreaking result because such structure is theoretically predicted to be unstable under ambient condition. Afterwards, two very important experiments [131,132] reveal that charge carriers in graphene are governed by the Dirac equation with zero rest mass. This two-dimensional system draws large amount of attention worldwide, because quantum effect can be observed on this material on bench-top experiments. Besides quantum effect, the unique macroscopic properties of this novel material are studied in plenty of research works and many of them indeed outmatch those of ordinary bulk materials.

From the view point of solar energy device, graphene also has potential to bear different roles in a solar cell. Y. S. Chen *et al.* reported their organic photovoltaic devices with graphene as the acceptor material [133]. This application is based on the fact that the work function of graphene is 4.5eV which is lower than the LUMO of common donor polymer such as P3HT and poly(3-octylthiophene) (P3OT). The active layer of their devices consists of functionalized graphene dispersion to achieve large interfacial area.



Recently, another group also reported a graphene/CdSe composite film for quantum dot sensitized solar cell [134] in which graphene serves as a good conducting network for electron transportation.

Graphene electrode should be the most straightforward idea to utilize the advantages of graphene on solar cell applications because it is transparent and conducting. Transparent electrode in solid state solar cell is of fundamental importance to allow photovoltaic effect. In fact, a well prepared single layer graphene film can offer high transmittance comparable to ITO in the visible and near-infrared range [135]. X. Wang *et al.* have made a dye-sensitized organic solar cell with graphene anode [136], but their graphene was obtained by a reduction method which results in a thick graphene with low transmittance. Another example was presented by K. P. Loh *et al.* who replaced ITO by graphene as a transparent electrode [137]. The properties of graphene are modified by doping or coating to align the band structure as reported by Loh's group.

Compared to traditional metal electrode fabrication such as sputtering and thermal evaporation, the transfer process of graphene on devices is low cost and no need for vacuum environment which is commonly time-consuming on lowering the pressure. Therefore, graphene electrode is aimed to replace the top Au electrode and form a semi-transparent photovoltaic device. In such configuration, the device can receive light from both sides to increase the chance of illumination.

Furthermore, Poly(3,4-ethylenedioxythiophene): poly(styrenesulfonate) (PEDOT:PSS)



is introduced in the device mainly because of a practical consideration that graphene cannot be directly transferred on the hydrophobic P3HT. PEDOT:PSS layer is fabricated on the P3HT before the transferring process. This layer offers better contact between graphene and P3HT by chemical doping and also serves as an electron blocking layer. Both doped and non-doped devices are fabricated and characterized to illustrate the doping effect. For convenient to analyze, graphene is transferred on the optimum structure described in Chapter 3.

5.2 Properties of graphene

Graphene is, up to now, the most ideal free-standing 2D system as it is an only one-atom-thick crystal. Carbon atoms connect each other through delocalization of their valence electrons into sp^2 -hybridized orbitals to form hexagonal or so called honeycomb structure. Such delocalized electrons and extremely thin structure allow graphene to appear as a transparent conductor. Also, this condense matter system exhibits fascinating electronic properties (large breakdown current density [138] in the order of $10^8 A/cm^2$, ultrahigh charge carrier mobility [139] and ballistic transport of carriers), strong mechanical properties [140] (breaking strength of $\sim 40N/m$ which is nearly the theoretical limit, elastic limit as much as 20% and elastic modulus of TPa) and new quantum phenomena (chiral quantum hall effect [132] and conductivity without charge carrier [131]). Many graphene-based application ideas have been generated, such as flexible displays, gas sensors and high-speed transistors due to its exceptional mechanical, electrical, chemical and biocompatible properties [141-143].

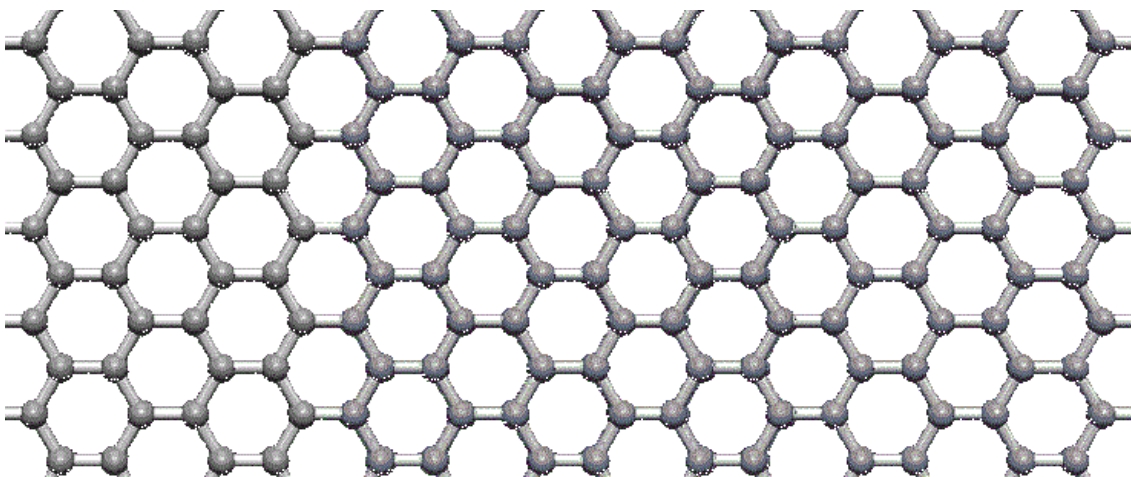


Figure 5-1 Structure of graphene [144].

Furthermore, abundant sources of carbon and well developed synthesis methods make graphene a low cost and environmental friendly material. Four main synthesis methods have currently been developed by researchers. Two top-down approaches are mechanical exfoliation of graphite [130] and chemical oxidation or exfoliation [145]. Two bottom-up approaches are epitaxial growth [146] and chemical vapor deposition [147] (CVD). Top-down approaches often require high quality graphite crystal but are difficult to control the size of graphene product. In contrast, bottom-up approaches are readier for mass production and easier to get single layer graphene with considerable area. Therefore, CVD grown single layer graphene on copper foil supplied by Hefei University of Technology has been used to construct our devices.



5.3 Properties of PEDOT:PSS

PEDOT:PSS is a polymer mixture of PEDOT and PSS. PEDOT, as a member of polythiophene, possesses good conductivity and transparency, but it is insoluble in common solvents and unstable in air [148]. PSS acid is thus added to improve the solubility and stability. This results in an aqueous dispersion in which the acid deprotonates to carry a negative charge and PEDOT is in oxidized form as shown in Figure 5-2. The ratio of PEDOT and PSS also influences the conductivity of PEDOT:PSS [149] so that commercial suppliers often tailor the solution to suit different applications. A high conductivity PEDOT:PSS aqueous solution with concentration of 2.5% is supplied by Sigma-Aldrich Co. LLC. and used in this work.

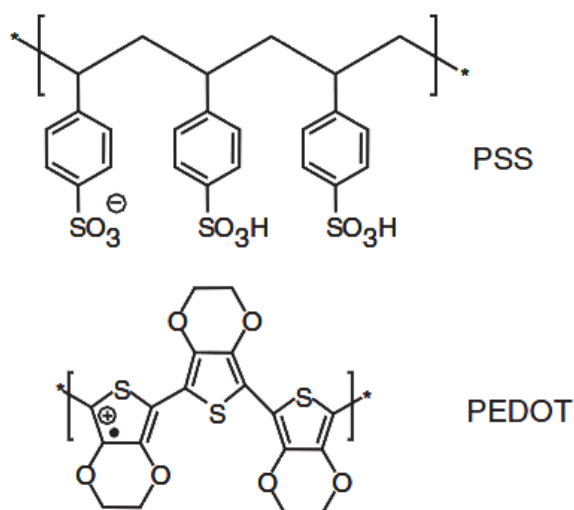


Figure 5-2 Structure of PEDOT:PSS [149].

Using this polymer mixture, thin, transparent, ductile and conductive film can be coated on a hydrophilic surface. PEDOT:PSS has been used as electron blocking layer in many



organic electronic devices. Also, because of the brittleness of ITO, PEDOT:PSS is one of the candidate being used as electrodes for flexible or even stretchable photovoltaic devices [149,150]. Another advantage is that it can be patterned in micro- or nano-meter scale by soft-lithographic methods [151].

5.4 Transferring and doping process

After the spin-coating of P3HT layer, oxygen plasma treatment is carried out for a few seconds on the P3HT surface to tune it from hydrophobic to hydrophilic. Figure 5-3 shows the contact angle change before and after the treatment. PEDOT:PSS is then spin-coated on the surface at 3000 rpm for 30 s. This layer is annealed at 120°C for 20 min in nitrogen ambient. Some region apart from ITO is wiped off and Au film is deposited on it. This film is prepared to connect with graphene for the convenience of measurement.

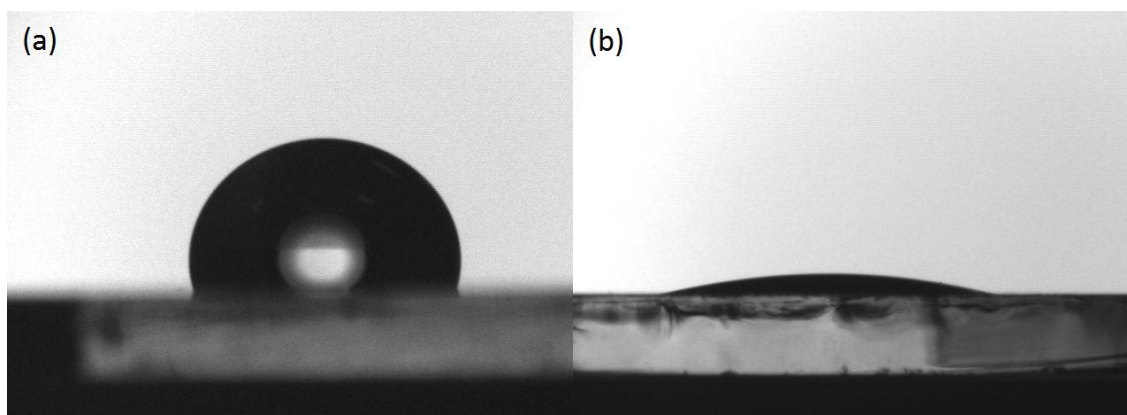


Figure 5-3 Contact angle of water on P3HT (a) before and (b) after O₂ plasma treatment.



Many processes to transfer graphene from copper foil have been described in papers and the method reported by Ruoff *et al.* [135] is followed. In the beginning, 0.06 g PMMA is dissolved uniformly in 1 ml ethyl methyl ketone. About 300 nm-thick PMMA layer is spin-coated on a CVD grown graphene on copper substrate. After slow curing at 40°C on hot plate for an hour, the copper substrate is etched by an iron(III) chloride water solution overnight. The PMMA/graphene film is floated on DI water to wash out chemicals and residue. The washing process should go on with fresh DI water until no more color change of water is observed. At this stage, the PMMA/graphene film is ready to be placed on the active layer with annealed PEDOT:PSS and overlapped with ITO and Au film region at the same time. For non-doping process, it is dried directly on a heater. For doping process, a small amount of PEDOT:PSS solution is dropped near the graphene film to float it and dried by spin-coating. The cell is then placed in a nitrogen box for annealing at 120°C for 20 min to remove any oxygen and moisture. Note that there is no need to wash out the PMMA layer before encapsulation.

5.5 Graphene characterization

At the beginning, we check the quality of the purchased CVD grown graphene by measuring its sheet resistance and transmittance. Graphene is firstly transferred on the SiO₂/Si plate because of its smoothness. Two gold electrodes are deposited on it by thermal evaporation through a patterned mask to form ohmic contact. The sheet resistance of graphene over a 5mm x 5mm area is found to be about 200 Ω/sq. Although



ITO usually has sheet resistance about $40 \Omega/\text{sq}$, both these values become negligible if they are compared with series resistance of hybrid junction which is typically 10^4 - $10^5 \Omega$.

In order to measure the transmittance, another graphene is transferred on a normal glass substrate and scanned over the UV-visible range. The graphene film demonstrates quite good transmittance over this relevant spectral range as shown in Figure 5-4. Over 95% of light intensity can transmit through the graphene layer except for a small portion of high energy photon which gives small contribution in the exciton generation. With good conducting and transmission properties, the transferred graphene film is basically capable for used as the electrode in solid state solar cell.

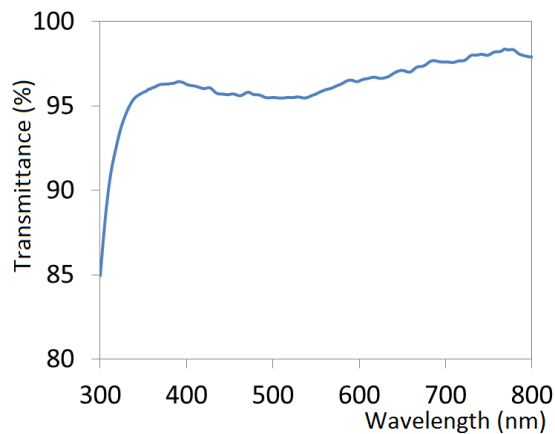


Figure 5-4 Transmittance of graphene from 300 nm to 800 nm.

5.6 Characterization of non-doping semi-transparent device

The J-V characteristics of a non-doped device about 0.16 cm^2 are measured. The performance of this device with respect to the different side of illumination is shown in



Figure 5-5. To compare the performance, the J-V characteristics of a normal device with Au top electrode is also plotted in the figure. The key parameters are summarized in Table 5-1. The J-V characteristics of the semi-transparent device give V_{oc} of 0.45 V when illuminated from the ITO side and 0.30 V from the graphene side. Compared to the normal device, these V_{oc} is a bit low. Nevertheless, when the device is illuminated from ITO, the J_{sc} of it is the same as that of the normal device. This result indicates that both devices have the same exciton generation process but the electrode contact or structure of graphene device is not as good as the Au device so that it exhibits lower V_{oc} and FF. The bad contact probably comes from the morphology mismatch of graphene film and the annealed PEDOT:PSS layer. The CVD grown single layer graphene is not flat but is a replica of the surface of copper substrate. Meanwhile, annealed PEDOT:PSS layer also has a certain roughness.

Table 5-1 Summary of performance parameters of the non-doped device and the normal device.

Curve	J_{sc} (mA/cm ²)	V_{oc} (V)	FF	η (%)
ITO	-1.53	0.44	0.47	0.32
Gra	-0.98	0.30	0.45	0.13
Au	-1.52	0.55	0.55	0.46

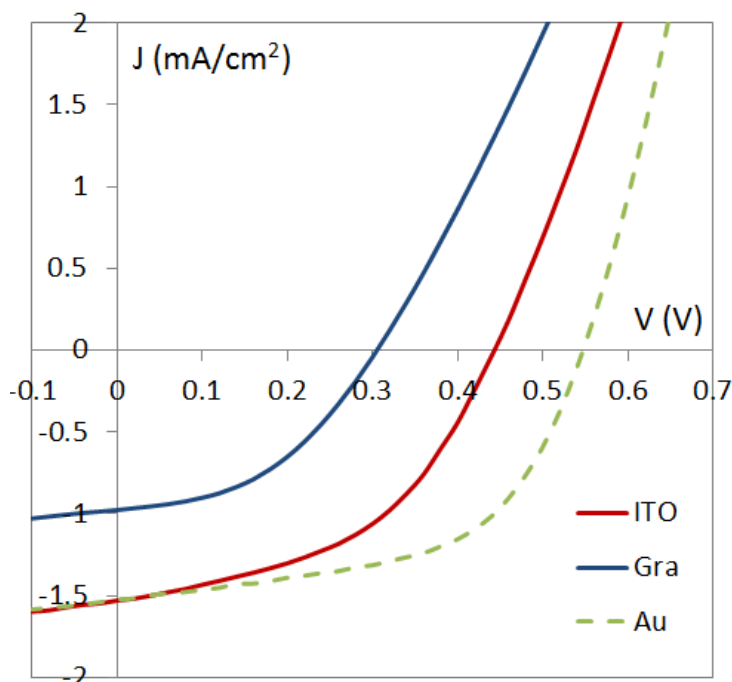


Figure 5-5 J-V characteristics of normal device and non-doped device at different side of illumination.

5.7 Characterization of doped semi-transparent device

To deal with the contact problem, the graphene film is doped with PEDOT:PSS solution. The additional PEDOT:PSS solution dried by spin-coating can fill up the gaps in-between and avoid the involvement of extra medium interface. The performance of the doped device with the same structure is measured and corresponds to the red curves in Figure 5-6. The V_{oc} increases by almost 0.1 V when illuminated from ITO while it has no improvement when illuminated from graphene. This leads to a conclusion that contact problem is not the cause of low V_{oc} in the latter case.



To further investigate, the EQE of the device on both sides was measured and corresponds to the red curves in Figure 5-7. The shapes of EQE curves surprisingly indicate that the contribution of P3HT is very low when illuminated from graphene. In this case, light rays penetrate through the P3HT layer first, but the absorbed light does not favor to generate current. It is probably because excitons are mainly generated near the interface of P3HT and PEDOT:PSS rather than the interface of TiO₂ and P3HT which is a charge dissociation site. From the above consideration, a hypothesis is suggested that the low performance may be due to high attenuation and limited exciton diffusion length in the P3HT layer.

5.7.1 Single-sided illumination analysis

To verify the hypothesis, devices with similar area but different P3HT thickness are fabricated and characterized on both sides. By adjusting the concentration of P3HT solution, TiO₂ fibers are covered by P3HT layers with different thickness. Figure 5-6 shows the corresponding J-V characteristics of the obtained devices with respect to illumination from different sides.

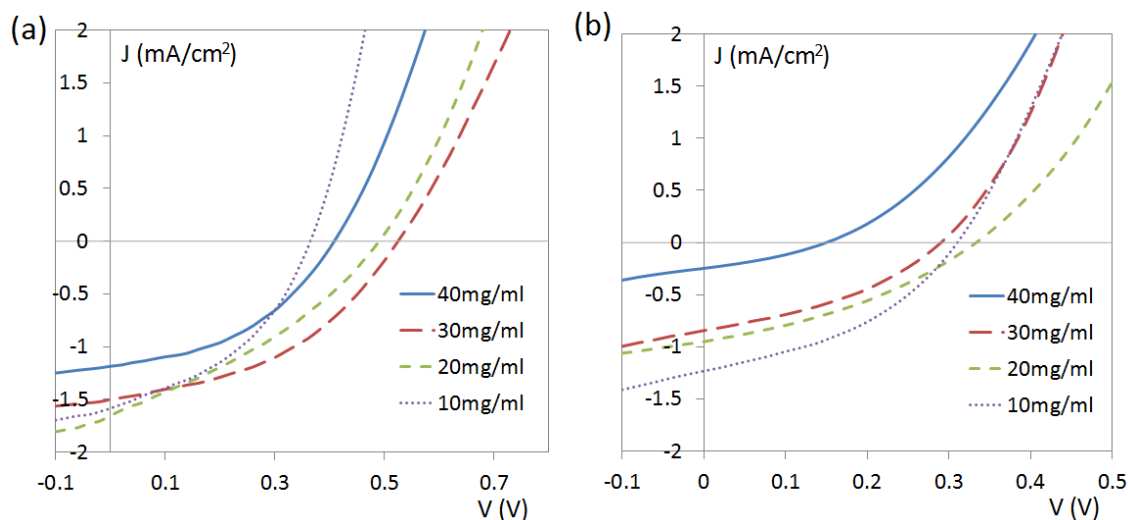


Figure 5-6 J-V characteristics of the doped devices with illumination on the (a) ITO and (b) graphene side.

For illumination from the ITO side, the maximum efficiency of 0.33 % and Voc of 0.53 V are given by 30 mg/ml P3HT solution. Voc drops because of the smaller shunt resistance in thinner active layer, while charge carriers are subjected to serious recombination in thick active layer. And, devices with thin P3HT layer also demonstrate similar Jsc. For illumination from the graphene side, the thinnest device demonstrates the highest efficiency of 0.15 % and Jsc of 1.23 mA/cm². Generally, the devices show lower current and voltage in this case. The Jsc drops monotonically with increase in the thickness of P3HT. The Voc values of the three thinner devices exhibit weak dependence of P3HT thickness.

In both illumination cases, the thinner devices give higher Jsc. It illustrates that the exciton separation and charge collection is better in thinner devices. However, high



efficiency is impeded by low generated voltage. The Voc behaves differently in these two cases. When illumination comes from the ITO side, it increases remarkably with increase in the thickness of P3HT. When illumination comes from the graphene side, it keeps at a low value. Such discrepancy is further studied by the EQE measurement.

Figure 5-7 is the EQE results of the devices with respect to different P3HT thickness. We can observe from the curves that devices work as normal for all active layer thicknesses when illuminated from ITO. However, only the thinnest device gives normal EQE curve when illuminated from graphene. Figure 5-7 (a) shows that the effect of P3HT thickness on the photocurrent conversion process weakly depends on the photon energy.

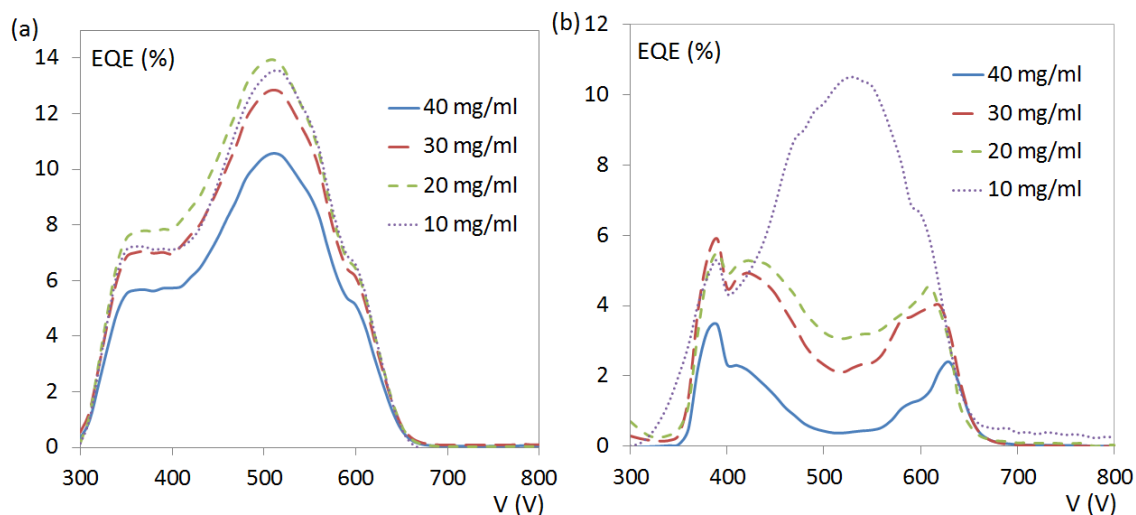


Figure 5-7 EQE of the doped devices with illumination on (a) ITO and (b) graphene side.



It can be seen in Figure 5-7 (b) that when illumination comes from the graphene side, charge carriers generated by high energy (300 - 400 nm) and low energy photons (400 - 700 nm) are subjected to different limitation. The low energy part drops continuously while the high energy part drops suddenly in the thickest device.

The EQE curves of the thick P3HT layer devices have the same shape of the inverse of P3HT absorption spectrum. It confirms that the light ray from the graphene electrode is subjected to severe absorption and loss. Obviously, thicker P3HT layer hinders excitons from charge dissociation so that the EQE curves for low energy photon are upside-down. It can be imagined that the exciton generation is proportional to the light intensity in that region so that the exciton concentration is expected to decrease exponentially with respect to thickness. Therefore, the majority of excitons are mainly generated at the interface of PEDOT:PSS and P3HT and cannot diffuse to the dissociation site and transform into the device current.

For high energy part, devices show a sharp absorption peak when illuminated from graphene rather than an absorption shoulder when illuminated from ITO. The variation of this part is similar to Figure 5-7 (a). It is probably because P3HT weakly absorbs this part of light. Although P3HT and TiO₂ also absorb this part of light, high energy excitons in P3HT will easily decay through thermalisation and lose the energy. Therefore, this part is expected to be more useful when light comes from ITO and absorbed by TiO₂.



5.7.2 Effective thickness

It is desirable to determine the amount of P3HT in the active layer, but it is actually a matrix containing unknown volume fraction of TiO₂ nanofibers. Hence, the transmittance of the active layer is utilized as an indicator to estimate what is the effective thickness of P3HT it is optically equivalent to. Figure 5-8 (a) shows the transmittance of four active layers. The transmission of the characteristic peak at $\lambda = 560$ nm of four P3HT thin films with definite thickness are measured and shown in Figure 5-8 (b). This wavelength is chosen because TiO₂ is transparent to this part of light. The least square fitting curve is calculated using a simple attenuation model:

$$T = 100\exp(-\alpha d)$$

where T is the transmittance, α the absorption coefficient and d is the penetration depth. The value of α is about 0.016 nm⁻¹ and the calculated effective thicknesses of P3HT are shown in Table 5-2.

Table 5-2 Estimated value of the effective thickness of P3HT.

condition	Transmittance at 560 nm (%)	Estimated thickness (nm)
40mg/ml	0.594	320
30mg/ml	2.669	226
20mg/ml	10.06	144
10mg/ml	33.18	68.9

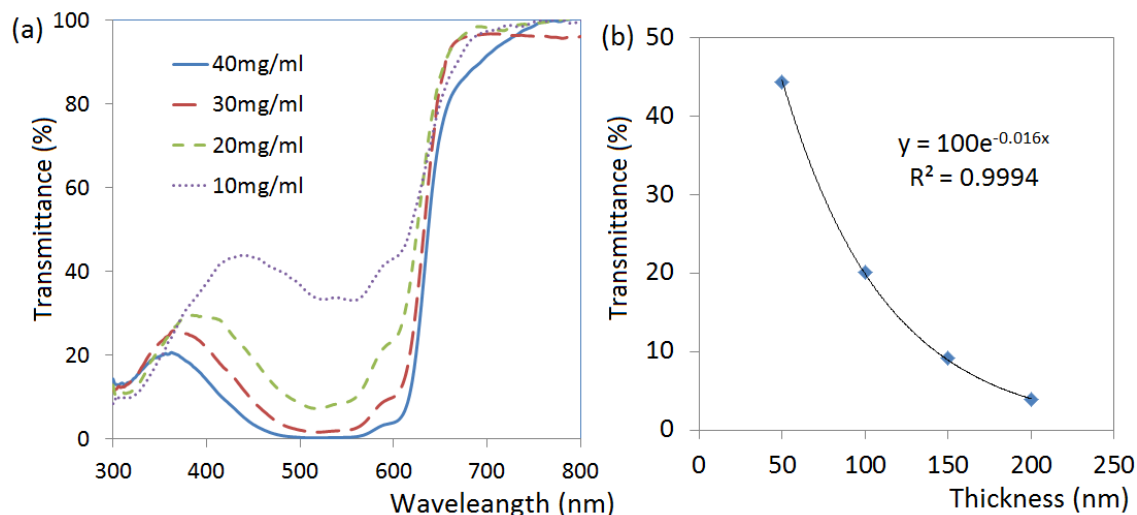


Figure 5-8 (a) Transmittance of four active layers and (b) least square fitting of the transmittance at $\lambda = 560$ nm with respect to d .

An optimum thickness of about 220 nm is obtained in ITO-illuminated case but not in graphene-illuminated case in which a thinner layer is better. The discrepancy between the optimum thicknesses in the two cases can be attributed to the anisotropy of the photo-response of the whole active layer. According to the EQE change in Figure 5-7 (a), we see that the free charges dissociated at the vicinity of TiO₂/P3HT interface become difficult to be collected when the effective thickness of P3HT is larger than 220 nm. Hence, the EQE change of the low energy part in Figure 5-7 (b) should result from the exciton diffusion to dissociation sites.

5.7.3 Double-sided illumination analysis

Furthermore, receiving light from both sides at the same time is the advantage of having



two transparent electrodes. It is worth and possible to measure the cell performance under both sides illumination simultaneously from the same light source. To achieve this purpose, two mirrors are utilized to construct a holder as illustrated in Figure 5-9. The tilting angle of the mirrors are fixed at 45° with respect to the bottom while the cells are held vertically.

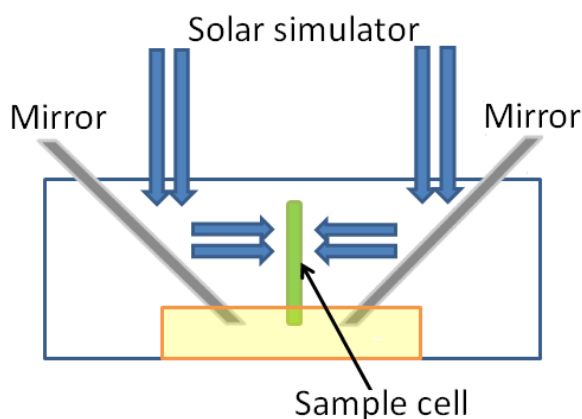


Figure 5-9 Schematic diagram of the holder for double side illumination.

The J-V characteristics of those four semi-transparent cells are shown in Figure.5-10. The obtained current is generally larger than single side illumination and only the values of J_{sc} are simply the superposition of the two cases in single side illumination. A high current density of 2.92 mA/cm^2 is produced by the thinnest device. Moreover, the V_{oc} remain at the higher values in the two cases. There exists a region that the graphene case does not contribute any current, but it exhibits an increase in current. Such increase may result from less leakage current in the double-side illumination case or the photoconductivity of P3HT.

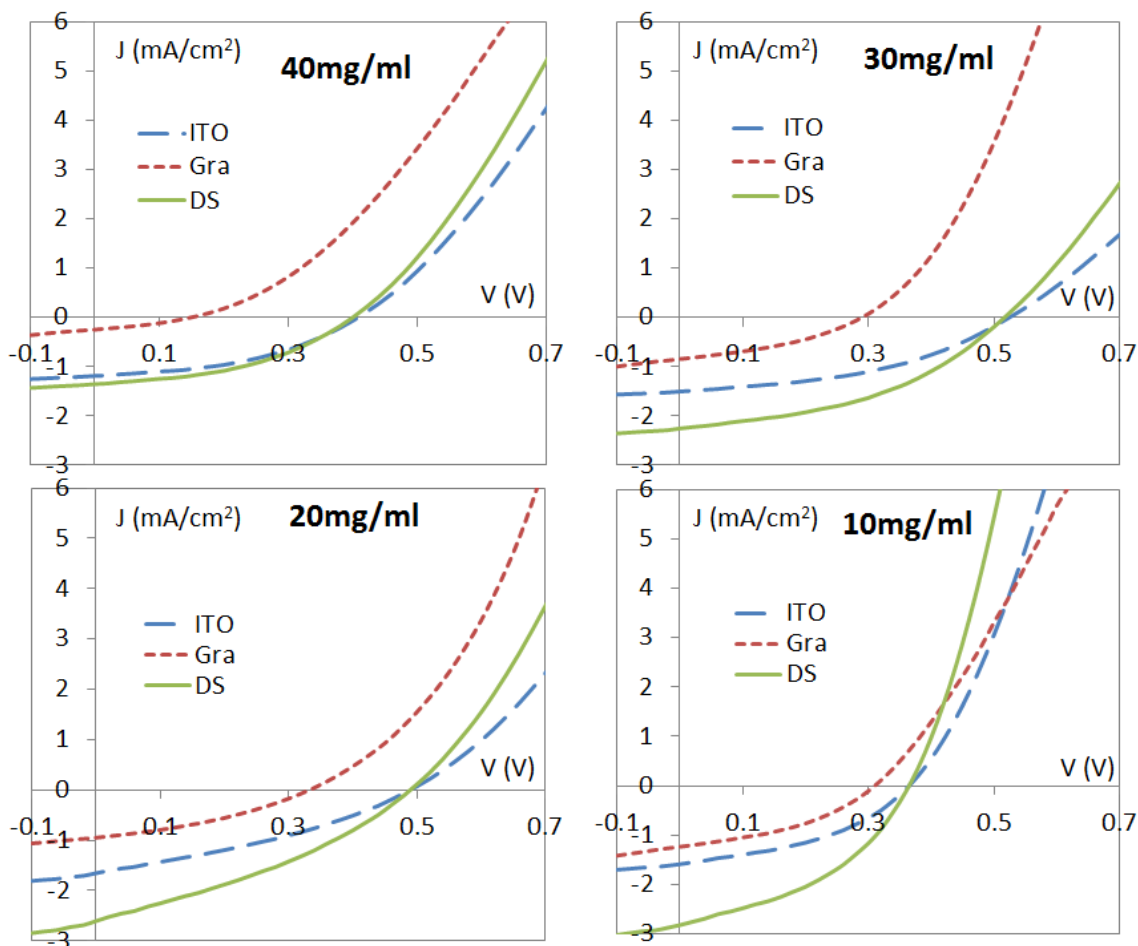


Figure 5-10 J-V characteristics of semi-transparent devices with respect to illumination from ITO, graphene (Gra) and on both side (DS).

Although the thinnest device gives the highest current, the efficiency is restricted by the low voltage. The 20 mg/ml sample has a high J_{sc} of 2.49 mA/cm² and V_{oc} of 0.48 V at the same time, but the FF of this device is low. The highest efficiency of 0.49 % is given by the 30 mg/ml sample. The FF demonstrated in the double side illumination is similar to that obtained by ITO illumination case. It is probable that feature of this curve is



dominated by the ITO illumination case. As benefited from the current increment, the efficiencies under double-side illumination are higher than the sum of the two single-side cases. Therefore, one can maximize the output of a single semi-transparent cell by illuminating both sides simultaneously. The summary of all analytical parameters are listed in Table 5-3.

Table 5-3 Summary of performance parameters of the semi-transparent devices with respect to different illumination cases.

Sample	Illumination	Jsc (mA/cm ²)	Voc (V)	FF	η (%)
40mg/ml	ITO	1.19	0.41	0.428	0.209
	Graphene	0.25	0.15	0.320	0.012
	Both side	1.35	0.40	0.428	0.231
30mg/ml	ITO	1.50	0.53	0.421	0.335
	Graphene	0.84	0.29	0.374	0.091
	Both side	2.25	0.50	0.437	0.492
20mg/ml	ITO	1.65	0.49	0.336	0.272
	Graphene	0.95	0.33	0.354	0.111
	Both side	2.49	0.48	0.341	0.407
10mg/ml	ITO	1.59	0.36	0.416	0.238
	Graphene	1.23	0.31	0.399	0.152
	Both side	2.92	0.37	0.414	0.447



5.8 Discussion

In the fabrication of the semi-transparent device, the PMMA layer is not washed out from the top of the graphene. The reason is that PMMA is transparent in the relevant range of wavelength so that it does not obstruct light absorption of the active layer. In addition, washing of PMMA will inevitably contaminate the device by organic solvent.

All the semi-transparent devices discussed in the above analysis have larger area of around 0.2 cm^2 . Compared to the area of devices discussed in Chapters 3 and 4, the area of graphene device is about ten times of their area which is typically smaller than 0.02 cm^2 . The difference comes from the fabrication method. The graphene transferring process involves spin-coating and other mechanical process in which defects are easily induced at the corner or edge of the graphene film. If the device area is defined by these corner or edge, defects will lead to uncertainty of the device area. Therefore, the area of graphene film should not be too small to ensure enough intact area overlap with the ITO electrode to sharply define the area of devices. The larger-area graphene film is also convenient for handling.



Chapter 6 Conclusions and Future Work

6.1 Conclusions

From the above systematic analysis, we can draw some conclusions about the principle of improvement and intrinsic properties of the analyzed devices.

In Chapter 3, the solid state $\text{TiO}_2/\text{P3HT}$ bilayered junction is an injection limited configuration and it can be improved by increasing the interfacial area of the junction. Adding TiO_2 nanofiber structure is one of the methods to achieve this purpose. The recombination rate is also reduced by such a manner so that geminate pair recombination in this junction is reduced by increasing the electron injection site to promote their dissociation. The optimized improvement by this method enhances the efficiency from around 0.07% to 0.4% which is mainly contributed by the increase of J_{sc} from around 0.25 to 1.4 mA/cm^2 .

In Chapter 4, interfacial modification of $\text{TiO}_2/\text{P3HT}$ junction is performed by depositing a CdS layer in between. This layer can promote the charge separation by cascaded band structure and provide more excitons in the junction by complementary absorption spectrum. The optimized amount or thickness of modification depends on the morphology of the junction. It is decided by the competition between more absorption and longer diffusion path. Higher V_{oc} and J_{sc} are generally given in this $\text{TiO}_2/\text{CdS}/\text{P3HT}$ configuration, but FF seems to be limited to about 0.55.



In Chapter 5, semi-transparent, large area, hybrid junction solar cells with intact graphene anode have been fabricated and show maximum efficiency of about 0.34% and 0.15% when illuminated from ITO and graphene, respectively. The contact problem of graphene after the transferring process can be improved by a solution doping treatment. The discrepancy of performance results from the existence of favor illumination direction of the active layer structure. Generation of excitons at the vicinity of dissociation site is beneficial to device operation. Optical paths and sequence of passing in medium of light ray influence the exciton distribution in different layers which is a crucial consideration to design and optimize the performance of a solar device.

6.2 Future work

Finally, some extension ideas can be suggested upon the presented work in this project. As we know that the organic device composed of P3HT, CdS and TiO₂ utilizes the solar spectrum of wavelength shorter than 650 nm. The integration over the energy and photon flux of solar spectrum shows that only 40 % of solar energy and 25% of photon is contained in this part of light. Therefore, it is desirable to make use of photovoltaic polymers or semiconductors with lower bandgap energy to enlarge the absorption range of device. For examples, poly [4,8-bis-substituted- benzo [1,2-b4,5-b'] dithiophene- 2,6-diyl- alt-4-substituted- thieno [3,4-b] thiophene- 2,6-diyl] (PEDTTT) and PCPDTBT are two possible organic candidates with bandgaps of 1.77eV and 1.4eV, respectively



[152,153].

In addition, the charge injection property largely depends on the junction morphology and constitutive materials. To further increase the interfacial area, junction morphology with smaller features could be developed either by improving the electrospinning process to synthesize thinner and more regular nanofibers or by seeking other nanotechnology for material growth. Nanorods or porous TiO_2 may give smaller features to enlarge the interface.

Besides, the concept of tandem solar cells can be introduced to enhance the performance. A different junction can be constructed upon the previous one to form multi-junctions. Single multi-junction device can boost the device V_{oc} by cascaded effect, but it involves more technical problems such as current matching and recombination layer. Another possibility is provided by the semi-transparent device because it is transparent to wavelength longer than 650 nm. A photovoltaic device using infrared region could be placed behind the semi-transparent device so that the two devices operate separately at the same time. This method also reduces the technical problem in designing and fabricating a single series tandem solar cell.



References

1. C. W. Tang, "Twolayer organic photovoltaic cell", *Appl. Phys. Lett.* **48**, 183-185 (1986).
2. X. Yang, J. K. J. van Duren, R. A. J. Janssen, M. A. J. Michels, and J. Loos, "Morphology and thermal stability of the active layer in poly (p-phenylene vinylene)/methanofullerene plastic photovoltaic devices", *Macromolecules* **37**, 2151-2158 (2004).
3. Y.-Y. Lin, T.-H. Chu, S.-S. Li, C.-H. Chuang, C.-H. Chang, W.-F. Su, C.-P. Chang, M.-W. Chu, and C.-W. Chen, "Interfacial nanostructuring on the performance of polymer/TiO₂ nanorod bulk heterojunction solar cells", *J. Am. Chem. Soc.* **131**, 3644-3649 (2009).
4. Solar spectrum data from National Renewable Energy Laboratory. Website: <http://rredc.nrel.gov/solar/spectra/am1.5/>
5. Y.-J. Cheng, S.-H. Yang, and C.-S. Hsu, "Synthesis of conjugated polymers for organic solar cell applications", *Chem. Rev.* **109**, 5868–5923 (2009).
6. B. Kippelen and J.-L. Bredas, "Organic photovoltaics", *Energy & environ. Sci.* **2**, 251-261 (2009).
7. A. Babel and S. A. Jenekhe, "Electron transport in thin-film transistors from an n-type conjugated polymer", *Adv. Mater.* **15**, 371-374 (2002).
8. V. Coropceanu, J. Cornil, D. A. da Silva Filho, Y. Olivier, R. Silbey, and J.-L. Bredas, "Charge transport in organic semiconductors", *Chem. Rev.* **107**, 926-952



- (2007).
9. F. Pschenitzka and J. C. Sturm, "Three-color organic light-emitting diodes patterned by masked dye diffusion", *Appl. Phys. Lett.* 74, 1913-1915 (1999).
 10. S. E. Shaheen, R. Radspinner, N. Peyghambarian, and G. E. Jabbour, "Fabrication of bulk heterojunction plastic solar cells by screen printing", *Appl. Phys. Lett.* 79, 2996-2998 (2001).
 11. A. Dodabalapur, Z. Bao, A. Makhija, J. G. Laquindanum, V. R. Raju, Y. Feng, H. E. Katz, and J. Rogers, "Organic smart pixels", *Appl. Phys. Lett.* 73, 142-144 (1996).
 12. S.-C. Chang, J. Liu, J. Bharathan, Y. Yang, J. Onohara and J. Kido, "Multicolor organic light-emitting diodes processed by hybrid inkjet printing", *Adv. Mater.* 11, 734-737 (1999).
 13. G. Wang, J. Swensen, D. Moses, and A. J. Heeger, "Increased mobility from regioregular poly(3-hexylthiophene) field-effect transistors", *J. Appl. Phys.* 93, 6137-6141 (2003).
 14. F. Wudl, "The chemical properties of buckminsterfullerene (C₆₀) and the birth and infancy of fullerenes", *Acc. Chem. Res.* 25, 157-161 (1992).
 15. J. J. M. Halls, K. Pichler, R. H. Friend, S. C. Moratti, and A. B. Holmes, "Exciton diffusion and dissociation in a poly(*p*-phenylenevinylene)/C₆₀ heterojunction photovoltaic cell", *Appl. Phys. Lett.* 68, 3120-3122 (1996).
 16. J. Y. Kim, S. H. Kim, H.-H. Lee, K. Lee, W. Ma, X. Gong and A. J. Heeger, "New architecture for high-efficiency polymer photovoltaic cells using solution-based titanium oxide as an optical spacer", *Adv. Mater.* 18, 572-576 (2006).



17. T. M. Clarke and J. R. Durrant, "Charge photogeneration in organic solar cells", *Chem. Rev.* 110, 6736-6767 (2010).
18. V. D. Mihailetschi, L. J. A. Koster, P. W. M. Blom, C. Melzer, B. de Boer, J. K. J. van Duren, R. A. J. Janssen, "Compositional dependence of the performance of poly(p-phenylene vinylene):methanofullerene bulk-heterojunction solar cells", *Adv. Funct. Mater.* 15, 795-801 (2005).
19. V. D. Mihailetschi, J. Wildeman, and P. W. M. Blom, "Space-charge limited photocurrent", *Phys. Rev. Lett.* 94, 126602 (2005).
20. M. C. Scharber, D. Mühlbacher, M. Koppe, P. Denk, C. Waldauf, A. J. Heeger, and C. J. Brabec, "Design rules for donors in bulk-heterojunction solar cells-towards 10% energy-conversion efficiency", *Adv. Mater.* 18, 789-794 (2006).
21. J. Gilot, M. M. Wienk, and R. A. J. Janssen, "Optimizing polymer tandem solar cells", *Adv. Mater.* 22, E67-E71 (2010).
22. D. Veldman, O. Ipek, S. C. J. Meskers, J. Sweelssen, M. M. Koetse, S. C. Veenstra, J. M. Kroon, S. S. van Bavel, J. Loos, and R. A. J. Janssen, "Compositional and electric field dependence of the dissociation of charge transfer excitons in alternating polyfluorene copolymer/fullerene blends", *J. Am. Chem. Soc.* 130, 7721-7735 (2008).
23. P. Peumans, S. R. Forrest, "Separation of geminate charge-pairs at donor-acceptor interfaces in disordered solids", *Chem. Phys. Lett.* 398, 27-31 (2004).
24. G. Li, V. Shrotriya, J. Huang, Y. Yao, T. Moriarty, K. Emery, and Y. Yang, "High-efficiency solution processable polymer photovoltaic cells by self-organization of polymer blends", *Nat. Mater.* 4, 864 – 868 (2005).



25. W. J. E. Beek, M. M. Wienk, and R. A. J. Janssen, "Efficient hybrid solar cells from zinc oxide nanoparticles and a conjugated polymer", *Adv. Mater.* 16, 1009-1013 (2004).
26. W. U. Huynh, J. J. Dittmer, and A. P. Alivisatos, "Hybrid nanorod-polymer solar cells", *Science* 295, 2425-2427 (2002).
27. K. Das, and S. K. De, "Optical properties of the type-II core-shell $\text{TiO}_2@\text{CdS}$ nanorods for photovoltaic applications", *J. Phys. Chem. C* 113, 3493-3501 (2009).
28. H.-S. Shim, S.-I. Na, S. H. Nam, H.-J. Ahn, H. J. Kim, D.-Y. Kim, and W. B. Kim, "Efficient photovoltaic device fashioned of highly aligned multilayers of electrospun TiO_2 nanowire array with conjugated polymer", *Appl. Phys. Lett.* 92, 183107 (2008).
29. Y. Tak, S. J. Hong, J. S. Lee, and K. Yong, "Fabrication of ZnO/CdS core/shell nanowire arrays for efficient solar energy conversion", *J. Mater. Chem.* 19, 5945-5951 (2009).
30. J. A. Chang, J. H. Rhee, S. H. Im, Y. H. Lee, H.-J. Kim, S. I. Seok, Md. K. Nazeeruddin, and M. Gratzel, "High-performance nanostructured inorganic-organic heterojunction solar cells", *Nano Lett.* 10, 2609-2612 (2010).
31. R. Zhu, C.-Y. Jiang, B. Liu, and S. Ramakrishna, "Highly efficient nanoporous TiO_2 -polythiophene hybrid solar cells based on interfacial modification using a metal-free organic dye", *Adv. Mater.* 21, 994-1000 (2009).
32. N. C. Greenham, X. Peng, and A. P. Alivisatos, "Charge separation and transport in conjugated-polymer/semiconductor-nanocrystal composites studied by photoluminescence quenching and photoconductivity", *Phys. Rev. B* 54, 17628-



- 17637 (1996).
33. A.J. Breeze, Z. Schlesinger, S.A. Carter, and P. J. Brock, "Charge transport in TiO₂/MEH-PPV polymer photovoltaics", *Phys. Rev. B* 64, 125205 (2001).
 34. W. U. Huynh, X. Peng, and A. P. Alivisatos, "CdSe nanocrystal rods/poly(3-hexylthiophene) composite photovoltaic devices", *Adv. Mater.* 11, 923-927 (1999).
 35. C.-H. Chang, T.-K. Huang, Y.-T. Lin, Y.-Y. Lin, C.-W. Chen, T.-H. Chu, and W.-F. Su, "Improved charge separation and transport efficiency in poly(3-hexylthiophene)-TiO₂ nanorod bulk heterojunction solar cells", *J. Mater. Chem.* 18, 2201-2207 (2008).
 36. L. E. Greene, M. Law, B. D. Yuhas, and P. Yang, "ZnO-TiO₂ core-shell nanorod/P3HT solar cells", *J. Phys. Chem.* 111, 18451-18456 (2007).
 37. K. Shankar, G. K. Mor, H. E. Prakasam, O. K. Varghese, and C. A. Grimes, "Self-assembled hybrid polymer-TiO₂ nanotube array heterojunction solar cells", *Langmuir* 23, 12445-12449 (2007).
 38. U. Bach, D. Lupo, P. Comte, J. E. Moser, F. Weissortel, J. Salbeck, H. Spreitzer, and M. Grätzel, "Solid-state dye-sensitized mesoporous TiO₂ solar cells with high photon-to-electron conversion efficiencies", *Nature* 395, 583-585 (1998).
 39. K. M. Coakley, and M. D. McGehee, "Photovoltaic cells made from conjugated polymers infiltrated into mesoporous titania", *Appl. Phys. Lett.* 83, 3380-3382 (2003).
 40. D. Gebeyehu, C. J. Brabec, F. Padinger, T. Fromherz, S. Spiekermann, N. Vlachopoulos, F. Kienberger, H. Schindler, and N. S. Sariciftci, "Solid state dye-



- sensitized TiO₂ solar cells with poly(3-octylthiophene) as hole transport layer”, *Synth. Met.* 121, 1549-1550 (2001).
41. S.-J. Moon, J.-H. Yum, R. Humphry-Baker, K. M. Karlsson D. P. Hagberg, T. Marinado, A. Hagfeldt, L. Sun, M. Grazel, and Md. K. Nazeeruddin, “Highly efficient organic sensitizers for solid-state dye-sensitized solar cells”, *J. Phys. Chem. C* 113, 16816-16820 (2009).
42. A. Fujishima, X. Zhang, and D. A. Tryk, “TiO₂ photocatalysis and related surface phenomena”, *Sur. Sci. Rep.* 63, 515-582 (2008).
43. Y. Bessekhoud, D. Robert, and J. V. Weber, “Preparation of TiO₂ nanoparticles by sol-gel route”, *Int. J. Photoenergy* 5, 153-158 (2003).
44. R. W. Matthews, “Photooxidation of organic impurities in water using thin films of titanium dioxide”, *J. Phys. Chem.* 91, 3328-3333 (1987).
45. O. Carp, C. L. Huisman, and A. Reller, “Photoinduced reactivity of titanium dioxide”, *Prog. Solid State Chem.* 32, 33-177 (2004).
46. A. Mills, N. Elliott, G. Hill, D. Fallis, J. R. Durrant, and R. L. Willis, “Preparation and characterization of novel thick sol-gel titania film photocatalysts”, *Photochem. Photobiol. Sci.* 2, 591-596 (2003).
47. A. Mills, J. Wang, and M. Crow, “Photocatalytic oxidation of soot by P25 TiO₂ films”, *Chemosphere* 64, 1012-1035 (2006).
48. J. C. Yu, J. Yu, W. Ho, Z. Jiang, and L. Zhang, “Effects of F- doping on the photocatalytic activity and microstructures of nanocrystalline TiO₂ powders”, *Chem. Mater.* 14, 3808-3816 (2002).
49. Article from Wikipedia on anatase. Website: <http://en.wikipedia.org/wiki/Anatase>



50. Article from Wikipedia on Rutile. Website: <http://en.wikipedia.org/wiki/Rutile>
51. J. C. Jamieson, and B. Olinger, "Pressure-temperature studies of anatase, brookite, rutile, and TiO₂(II): A discussion", *Mineral. Notes* 54, 1477-1481 (1969).
52. T. B. Ghosh, S. Dhabal, and A. K. Datta, "On crystallite size dependence of phase stability of nanocrystalline TiO₂", *J. Appl. Lett.* 94, 4577-4582 (2003).
53. J. Muscat, V. Swamy, and N. M. Harrison, "First-principles calculations of the phase stability of TiO₂", *Phys. Rev. B* 65, 224112 (2002).
54. N. A. Dubrovinskaia, L. S. Dubrovinsky, R. Ahuja, V. B. Prokopenko, V. Dmitriev, H.-P. Weber, J. M. Osorio-Guillen, and B. Johansson, "Experimental and theoretical identification of a new high-pressure TiO₂ polymorph", *Phys. Rev. Lett.* 87, 275501 (2001).
55. A. Beltran, L. Gracia, and J. Andres, "Density functional theory study of the brookite surfaces and phase transitions between natural titania polymorphs", *J. Phys. Chem. B* 110, 23417-23423 (2006).
56. H. Zhang, and J. F. Banfield, "Thermodynamic analysis of phase stability of nanocrystalline titania", *J. Mater. Chem.* 8, 2073-2076 (1998).
57. J. K. Burdett, T. Hughbanks, G. J. Miller, J. W. Richardson, Jr., and J. V. Smith, "Structural-electronic relationships in inorganic solids: Powder neutron diffraction studies of the rutile and anatase polymorphs of titanium dioxide at 15 and 295 K", *J. Am. Chem. Soc.* 109, 3639-3646 (1987).
58. H. Tang, K. Prasad, R. Sanjinès, P. E. Schmid, and F. Lévy, "Electrical and optical properties of TiO₂ anatase thin films", *J. Appl. Lett.* 75, 2042-2047 (1994).
59. M. Hirano, C. Nakahara, K. Ota, O. Tanaike, and M. Inagaki, "Photoactivity and



- phase stability of ZrO₂-doped anatase-type TiO₂ directly formed as nanometer-sized particles by hydrolysis under hydrothermal conditions”, *J. Solid State Chem.* 170, 39-47 (2003).
60. J. Zhang, Q. Xu, Z. Feng, M. Li, and C. Li, “Importance of the relationship between surface phases and photocatalytic activity of TiO₂”, *Angew. Chem. Int. Ed.* 47, 1766-1769 (2008).
61. R. A. Spurr, and H. Myers, “Quantitative analysis of anatase-rutile mixtures with an X-Ray diffractometer”, *Anal. Chem.* 29, 760-762 (1957).
62. J. Sun, L. Gao, and Q. Zhang, “Synthesizing and comparing the photocatalytic properties of high surface area rutile and anatase titania nanoparticles”, *J. Am. Ceram. Soc.* 86, 1677-1682 (2003).
63. H. Chang, and P. J. Huang, “Thermo-Raman studies on anatase and rutile”, *J. Raman Spectrosc.* 29, 97-102 (1998).
64. H. Sirringhaus, N. Tessler, and R. H. Friend, “Integrated optoelectronic devices based on conjugated polymers”, *Science* 280, 1741-1744 (1998).
65. H. Sirringhaus, N. Tessler, and R. H. Friend, “Integrated, high-mobility polymer field-effect transistors driving polymer light-emitting diodes”, *Syn. Mater.* 102, 857-860 (1999).
66. Z. L. Li, S. C. Yang, H. F. Meng, Y. S. Chen, Y. Z. Yang, C. H. Liu, S. F. Horng, C. S. Hsu, L. C. Chen, J. P. Hu, and R. H. Lee, “Patterning-free integration of polymer light-emitting diode and polymer transistor”, *Appl. Phys. Lett.* 84, 3558-3560 (2004).
67. Y. Zhao, Z. Xie, Y. Qu, Y. Geng, and L. Wang, “Solvent-vapor treatment induced



- performance enhancement of poly(3-hexylthiophene):methanofullerene bulk-heterojunction photovoltaic cells”, *Appl. Phys. Lett.* 90, 043504 (2007).
68. G. Li, V. Shrotriya, Y. Yao, and Y. Yang, “Investigation of annealing effects and film thickness dependence of polymer solar cells based on poly(3-hexylthiophene)”, *J. Appl. Phys.* 98, 043704 (2005).
69. E. Bundgaard, and F. C. Krebs, “Low band gap polymers for organic photovoltaics”, *Sol. Energy Mater. Sol. Cells* 91, 954–985 (2007).
70. D. L. Pearson, J. S. Schumm, and J. M. Tour, “Iterative divergent/convergent approach to conjugated oligomers by a doubling of molecular length at each iteration. A rapid route to potential molecular wires”, *Macromolecules* 27, 2348-2350 (1994).
71. T. Izumi, S. Kobashi, K. Takimiya, Y. Aso, and T. Otsubo, “Synthesis and spectroscopic properties of a series of β -blocked long oligothiophenes up to the 96-mer: Reevaluation of effective conjugation length”, *J. Am. Chem. Soc.* 125, 5286-5287 (2003).
72. S. Wang, H. Takahashi, K. Yoshino, K. Tanaka, and T. Yamabe, “Dependence of poly(3-alkylthiophene) film properties on electrochemical polymerization conditions and alkyl chain length”, *Jpn. J. Appl. Phys.* 29, 772-775 (1990).
73. R. D. McCullough, R. D. Lowe, M. Jayaraman, and D. L. Anderson, “Design, synthesis, and control of conducting polymer architectures: Structurally homogeneous poly(3-alkylthiophenes)”, *J. Org. Chem.* 58, 904-912 (1993).
74. Y. Kim, S. Cook, S. M. Tuladhar, S. A. Choulis, j. Nelson, J. R. Durrant, D. D. C. Bradley, M. Giles, I. Mcculloch, C.-S. Ha, and M. Ree, “A strong regioregularity



- effect in self-organizing conjugated polymer films and high-efficiency polythiophene:fullerene solar cells”, *Nat. Mater.* 5, 197-203 (2006).
75. J. Obrzut, and K. A. Page, “Electrical conductivity and relaxation in poly(3-hexylthiophene)”, *Phys. Rev. B* 80, 195211 (2009).
 76. D. Li, Y. Wang, and Y. Xia, “Electrospinning nanofibers as uniaxially aligned arrays and layer by layer stacked films”, *Adv. Mater.* 16, 361-366 (2004).
 77. D. Li, and Y. Xia, “Fabrication of titania nanofibers by electrospinning”, *Nano Lett.* 3, 555-560 (2003).
 78. R. Zhu, C.-Y. Jiang, X.-Z. Liu, B. Liu, A. Kumar, and S. Ramakrishna, “Improved adhesion of interconnected TiO₂ nanofiber network on conductive substrate and its application in polymer photovoltaic devices”, *Appl. Phys. Lett.* 93, 013102 (2008).
 79. D. Hussain, F. Loyal, A. Greiner, and J. H. Wendorff, “Structure property correlations for electrospun nanofiber nonwovens”, *Polymer* 51, 3989-3997 (2010).
 80. A. Greiner, and J. H. Wendorff, “Electrospinning: A fascinating method for the preparation of ultrathin fibers”, *Angew. Chem. Int. Ed.* 46, 5670 - 5703 (2007).
 81. D. Li, and Y. Xia, “Electrospinning of nanofibers: Reinventing the wheel?”, *Adv. Mater.* 16, 1151-1170 (2004).
 82. A. Frenot, and I. S. Chronakis, “Polymer nanofibers assembled by electrospinning”, *Curr. Opin. Colloid Interface Sci.* 8, 64-75 (2003).
 83. A. L. Yarin, S. Koombhongse, and D. H. Reneker, “Bending instability in electrospinning of nanofibers”, *J. Appl. Phys.* 89, 3018 - 3026 (2001).



84. Y. M. Shin, M. M. Hohman, M. P. Brenner, and G. C. Rutledge, "Electrospinning: A whipping fluid jet generates submicron polymer fibers", *Appl. Phys. Lett.* 78, 1149 - 1151 (2001).
85. D. Zhang, and J. Chang, "Patterning of electrospun fibers using electroconductive templates", *Adv. Mater.* 19, 1664 - 1667 (2007).
86. R. Dersch, T. Liu, A. K. Schaper, A. Greiner, and J. H. Wendorff, "Electrospun nanofibers: Internal structure and intrinsic orientation", *J. Polym. Sci. A1* 41, 545 - 553 (2003).
87. D. Li, G. Ouyang, J. T. McCann, and Y. Xia, "Collecting electrospun nanofibers with patterned electrodes", *Nano Lett.* 5, 913 - 916 (2005).
88. T. D. Brown, P. D. Dalton, and D. W. Hutmacher, "Direct writing by way of melt electrospinning", *Adv. Mater.* 23, 5651 - 5657 (2011).
89. M. Seol, H. Kim, Y. Tak, and K. Yong, "Novel nanowire array based highly efficient quantum dot sensitized solar cell", *Chem. Commun.* 46, 5521 - 5523 (2010).
90. L. Shen, G. Zhu, W. Guo, C. Tao, X. Zhang, C. Liu, W. Chen, S. Ruan, and Z. Zhong, "Performance improvement of TiO₂/P3HT solar cells using CuPc as a sensitizer", *Appl. Phys. Lett.* 92, 073307 (2008).
91. B. O'Regan, and M. Gratzel, "A low-cost, high-efficiency solar cell based on dye-sensitized colloidal TiO₂ films", *Nature* 353, 737 - 740 (1991).
92. C. Goh, S. R. Scully, and M. D. McGehee, "Effects of molecular interface modification in hybrid organic-inorganic photovoltaic cells", *J. Appl. Phys.* 101, 114503 (2007).



93. R. Cohen, L. Kronik, A. Shanzer, D. Cahen, A. Liu, Y. Rosenwaks, J. K. Lorenz, and A. B. Ellis, "Molecular control over semiconductor surface electronic properties: Dicarboxylic acids on CdTe, CdSe, GaAs, and InP", *J. Am. Chem. Soc.* 121, 10545 - 10553 (1999).
94. C. Levy-Clement, R. Tena-Zaera, M. A. Ryan, A. Katty, and G. Hodes, "CdSe-sensitized p-CuSCN/nanowire n-ZnO heterojunctions", *Adv. Mater.* 17, 1512 - 1515 (2005).
95. I. Oja, A. Belaidi, L. Dloczik, M.-C. Lux-Steiner, and T. Dittrich, "Photoelectrical properties of $\text{In}(\text{OH})_x\text{S}_y/\text{PbS}(\text{O})$ structures deposited by SILAR on TiO_2 " *Semicond. Sci. Technol.* 21, 520 - 526 (2006).
96. K. Tennakone, G. R. R. A. Kumara, I. R. M. Kottegoda, V. P. S. Perera, and G. M. L. P. Aponso, "Nanoporous n- TiO_2 /selenium/p-CuCNS photovoltaic cell", *J. Phys. D: Appl. Phys.* 31, 2326 – 2330 (1998).
97. A. Belaidi, T. Dittrich, D. Kieven, J. Tornow, K. Schwarzburg, and M. Lux-Steiner, "Influence of the local absorber layer thickness on the performance of ZnO nanorod solar cells". *Phys. Stat. Sol. (RRL)* 2, 172 – 174 (2008).
98. M. Page, O. Niitsoo, Y. Itzhaik, D. Cahen, and G. Hodes, "Copper sulfide as a light absorber in wet-chemical synthesized extremely thin absorber (ETA) solar cells", *Energy Environ. Sci.* 2, 220 – 223 (2009).
99. E. D. Spoeke, M. T. Lloyd, E. M. McCready, D. C. Olson, Y.-J. Lee, and J. W. P. Hsu, "Improved performance of poly(3-hexylthiophene)/zinc oxide hybrid photovoltaics modified with interfacial nanocrystalline cadmium sulfide", *Appl. Phys. Lett.* 95, 213506 (2009).



100. G. Larramona, C. Chone, A. Jacob, D. Sakakura, B. Delatouche, D. Pere, X. Cieren, M. Nagino, and R. Bayon, "Nanostructured photovoltaic cell of the type titanium dioxide, cadmium sulfide thin coating, and copper thiocyanate showing high quantum efficiency", *Chem. Mater.* 18, 1688 – 1696 (2006).
101. A.J. Criddle, and C.J. Stanley, Eds., *Quantitative data file for ore minerals 3rd ed.*, Chapman & Hall, 1993.
102. J. W. Anthony, R. A. Bideaux, K. W. Bladh, and M. C. Nichols, Eds., *Handbook of Mineralogy*, Mineralogical Society of America, 2001.
103. C. T. Tsai, D. S. Chuu, G. L. Chen, and S. L. Yang, "Studies of grain size effects in rf sputtered CdS thin films", *J. Appl. Phys.* 79, 9105 - 9109 (1996).
104. G. Perna, V. Capozzi, S. Pagliara, M. Ambrico, and D. Lojacono, "Reflectance and photoluminescence characterization of CdS and CdSe heteroepitaxial films deposited by laser ablation technique", *Thin Solid Films* 387, 208 - 211 (2001).
105. P. P. Hankare, P. A. Chate, and D. J. Sathe, "CdS thin film: Synthesis and characterization", *Solid State Sci.* 11, 1226 – 1228 (2009).
106. K. Yamaguchi, T. Yoshida, T. Sugiura, and H. Minoura, "A novel approach for CdS thin-film deposition: Electrochemically induced atom-by-atom growth of CdS thin films from acidic chemical bath", *J. Phys. Chem. B* 102, 9677 – 9689 (1998).
107. S. Biswas, M. F. Hossain, and T. Takahashi, "Fabrication of Grätzel solar cell with TiO₂/CdS bilayered photoelectrode", *Thin Solid Films* 517, 1284 – 1288 (2008).
108. I. O. Oladeji, and L. Chow, "Optimization of chemical bath deposited cadmium sulfide thin films", *J. Electrochem. Soc.* 144, 2342 - 2346 (1997).



109. P. K. Nair, J. Campos, and M. T. S. Nair, "Opto-electronic characteristics of chemically deposited cadmium sulphide thin films", *Semicond. Sci. Technol.* 3, 134 – 145 (1998).
110. P. O'Brien, and T. Saeed, "Deposition and characterization of cadmium sulfide thin films by chemical bath deposition", *J. Cryst. Growth* 158, 497 - 504 (1996).
111. S. Corer, and G. Hodes, "Quantum size effects in the study of chemical solution deposition mechanisms of semiconductor films", *J. Phys. Chem.* 98, 5338 – 5346 (1994).
112. M. T. S. Nair, P. K. Nair, R. A. Zingaro, and E. A. Meyers, "Conversion of chemically deposited photosensitive CdS thin films to n-type by air annealing and ion exchange reaction", *J. Appl. Phys.* 75, 1557 (1994).
113. P. Roy, and S. K. Srivastava, "A new approach towards the growth of cadmium sulphide thin film by CBD method and its characterization", *Mater. Chem. Phys.* 95, 235 - 241 (2006).
114. Article from Wikipedia on Greenockite.
Website: <http://en.wikipedia.org/wiki/Greenockite>
115. Article from Wikipedia on Hawleyite.
Website: <http://en.wikipedia.org/wiki/Hawleyite>
116. Material safety data sheet acc. to OSHA and ANSI. 2010.
117. J. Elias, R. Tena-Zaera, and C. Lévy-Clément, "Electrodeposition of ZnO nanowires with controlled dimensions for photovoltaic applications: Role of buffer layer", *Thin Solid Films* 515, 8553 – 8557 (2007).
118. B. O'Regan, D. T. Schwartz S. M. Zakeeruddin, and M. Grätzel, "Electrodeposited



- nanocomposite n-p heterojunctions for solid-state dye-sensitized photovoltaics”, *Adv. Mater.* 12, 1263 - 1267 (2000).
119. M. J. Siegfried, and K.-S. Choi, “Electrochemical crystallization of cuprous oxide with systematic shape evolution”, *Adv. Mater.* 16, 1743 – 1746 (2004).
120. Y. Matsumoto, Y. Ishikawa, M. Nishida, and S. Ii, “A new electrochemical method to prepare mesoporous titanium(IV) oxide photocatalyst fixed on alumite substrate”, *J. Phys. Chem. B* 104, 4204 – 4209 (2000).
121. M.-S. Wu, Y.-A. Huang, C.-H. Yang, and J.-J. Jow, “Electrodeposition of nanoporous nickel oxide film for electrochemical capacitors”, *Int. J. Hydrogen Energy* 32, 4153 - 4159 (2007).
122. I. Zhitomirsky, “Cathodic electrodeposition of ceramic and organoceramic materials. Fundamental aspects”, *Adv. Colloid Interface Sci.* 97, 279 - 317 (2002).
123. I. Zhitomirsky, and A. Petric, “Cathodic electrodeposition of polymer films and organoceramic films”, *Mater. Sci. Eng., B* 78, 125 – 130 (2000).
124. J. A. Switzer, M. G. Shumsky, E. W. Bohannon, “Electrodeposited ceramic single crystals”, *Science* 284, 293 - 296 (1999).
125. G. S. Attard, P. N. Bartlett, N. R. B. Coleman, J. M. Elliott, J. R. Owen, J. H. Wang, “Mesoporous platinum films from lyotropic liquid crystalline phases”, *Science* 278, 838 - 840 (1997).
126. R. J. Jackman, S. T. Brittain, A. Adams, M. G. Prentiss, and G. M. Whitesides, “Design and fabrication of topologically complex, three-dimensional microstructures”, *Science* 280, 2089 - 2091 (1998).
127. D. Rosenthal, and T. I. Taylor, “A study of the mechanism and intermediates in the



- precipitation of cations with thioacetamide”, *J. Am. Chem. Soc.* 82, 4169 – 4174 (1960).
128. S. Chun, K. S. Han, J. S. Lee, H. J. Lim, H. Lee, and D. Kim, “Fabrication CdS thin film and nanostructure grown on transparent ITO electrode for solar cells”, *Curr. Appl. Phys.* 10, 5196 – 5200 (2010).
129. P. J. Brown, D. S. Thomas, A. Kohler, J. S. Wilson, J.-S. Kim, C. M. Ramsdale, H. Sirringhaus, and R. H. Friend, “Effect of interchain interactions on the absorption and emission of poly(3-hexylthiophene)”, *Phys. Rev. B* 67, 064203 (2003).
130. K. S. Novoselov, A. K. Geim, S. V. Morozov, D. Jiang Y. Zhang, S. V. Dubonos, I. V. Grigorieva, and A. A. Firsov, “Electric field effect in atomically thin carbon films”, *Science* 306, 666 - 669 (2004).
131. K. S. Novoselov, A. K. Geim, S. V. Morozov, D. Jiang, M. I. Katsnelson, I. V. Grigorieva, S. V. Dubonos and A. A. Firsov, “Two-dimensional gas of massless Dirac fermions in graphene”, *Nature* 438, 197 - 200 (2005).
132. Y. Zhang, Y.-W. Tan, H. L. Stormer, and P. Kim, “Experimental observation of the quantum Hall effect and Berry’s phase in graphene”, *Nature* 438, 201 - 204 (2005).
133. Z. Liu, Q. Liu, Y. Huang, Y. Ma, S. Yin, X. Zhang, W. Sun, and Y. Chen, “Organic photovoltaic devices based on a novel acceptor material: Graphene”, *Adv. Mater.* 20, 3924 – 3930 (2008).
134. S. Sun, L. Gao, Y. Liu, and J. Sun, “Assembly of CdSe nanoparticles on graphene for low-temperature fabrication of quantum dot sensitized solar cell”, *Appl. Phys. Lett.* 98, 093112 (2011).



135. X. Li, Y. Zhu, W. Cai, M. Borysiak, B. Han, D. Chen, R. D. Piner, L. Colombo, and R. S. Ruoff, "Transfer of large-area graphene films for high-performance transparent conductive electrodes", *Nano Lett.* 9, 4359 - 4363 (2009).
136. X. Wang, L. Zhi, and K. Mullen, "Transparent, conductive graphene electrodes for dye-sensitized solar cells", *Nano Lett.* 8, 323 - 327 (2008).
137. Y. Wang, S. W. Tong, X. F. Xu, B. Özyilmaz, and K. P. Loh, "Interface engineering of layer-by-layer stacked graphene anodes for high-performance organic solar cells", *Adv. Mater.* 23, 1514 – 1518 (2011).
138. R. Murali, Y. Yang, K. Brenner, T. Beck, and J. D. Meindl, "Breakdown current density of graphene nanoribbons", *Appl. Phys. Lett.* 94, 243114 (2004).
139. K. I. Bolotin, K. J. Sikes, Z. Jiang, M. Klima, G. Fudenberg, J. Hone, P. Kim, and H. L. Stormer, "Ultrahigh electron mobility in suspended graphene", *Solid State Commun.* 146, 351 – 355 (2008).
140. C. Lee, X. Wei, J. W. Kysar, and J. Hone, "Measurement of the elastic properties and intrinsic strength of monolayer graphene", *Science* 321, 385 - 388 (2008).
141. L. A. L. Tang, J. Wang, and K. P. Loh, "Graphene-based SELDI probe with ultrahigh extraction and sensitivity for DNA oligomer", *J. Am. Chem. Soc.* 132, 10976 – 10977 (2010).
142. F. Bonaccorso, Z. Sun, T. Hasan, and A. C. Ferrari, "Graphene photonics and optoelectronics", *Nat. Photonics* 4, 611 - 622 (2010).
143. L. Liao, Y.-C. Lin, M. Bao, R. Cheng, J. Bai, Y. Liu, Y. Qu, K. L. Wang, Y. Huang, and X. Duan, "High-speed graphene transistors with a self-aligned nanowire gate", *Nature* 467, 305 - 308 (2010).



144. Nano enhanced wholesale technologies, Newtechs, LLC.
Website: <http://www.nano-enhanced-wholesale-technologies.com/>
145. D. Li, M. B. Müller, S. Gilje, R. B. Kaner, and G. G. Wallace, “Processable aqueous dispersions of graphene nanosheets”, *Nat. Nanotechnol.* 3, 101 - 105 (2008).
146. Z. H. Ni, W. Chen, X. F. Fan, J. L. Kuo, T. Yu, A. T. S. Wee, and Z. X. Shen, “Raman spectroscopy of epitaxial graphene on a SiC substrate”, *Phys. Rev. B* 77, 115416 (2008).
147. K. S. Kim, Y. Zhao, H. Jang, S. Y. Lee, J. M. Kim, K. S. Kim, J.-H. Ahn, P. Kim, J.-Y. Choi, and B. H. Hong, “Large-scale pattern growth of graphene films for stretchable transparent electrodes”, *Nature* 457, 706 - 710 (2009).
148. M. M. de Kok, M. Buechel, S. I. E. Vulto, P. van de Weijer, E. A. Meulenkaamp, S. H. P. M. de Winter, A. J. G. Mank, H. J. M. Vorstenbosch, C. H. L. Weijtens, and V. van Elsbergen, “Modification of PEDOT:PSS as hole injection layer in polymer LED”, *Phys. Stat. Sol. (a)* 201, 1342 - 1359 (2004).
149. D. J. Lipomi, J. A. Lee, M. Vosgueritchian, B. C.-K. Tee, J. A. Bolander, and Z. Bao, “Electronic properties of transparent conductive films of PEDOT:PSS on stretchable substrates”, *Chem. Mater.* 24, 373 – 382 (2012).
150. B. Winther-Jensen, and F. C. Krebs, “High-conductivity large-area semi-transparent electrodes for polymer photovoltaics by silk screen printing and vapour-phase deposition”, *Sol. Energy Mater. Sol. Cells* 90, 123 - 132 (2006).
151. T. Granlund, T. Nyberg, L. S. Roman, M. Svensson, and O. Inganäs, “Patterning of polymer light-emitting diodes with soft lithography”, *Adv. Mater.* 12, 269 -273



- (2000).
152. J. Y. Kim, K. Lee, N. E. Coates, D. Moses, T.-Q. Nguyen, M. Dante, A. J. Heeger, “Efficient tandem polymer solar cells fabricated by all-solution processing”, *Science* 317, 222 - 225 (2011).
153. H.-Y. Chen, J. Hou, S. Zhang, Y. Liang, G. Yang, Y. Yang, L. Yu, Y. Wu, and G. Li, “Polymer solar cells with enhanced open-circuit voltage and efficiency”, *Nat. Photonics* 3, 649 – 653 (2009).